



**Aalto University**  
**School of Engineering**

Santeri Henrik Koivisto

## **Spray characteristics of a pressure-swirl atomizer while injecting high-viscosity liquid**

Diplomityö, joka on jätetty opinnäytteenä tarkastettavaksi  
diplomi-insinöörin tutkintoa varten.

Espoo 22.03.2019

Supervisor: Mika Järvinen

Instructor: Ari Kankkunen

---

**Tekijä** Santeri Henrik Koivisto

---

**Työn nimi** Pyörresuuttimen suihkun ominaisuudet korkean viskositeetin nesteellä

---

**Maisteriohjelma** Energy Technology**Koodi** K3007

---

**Työn valvoja** Mika Järvinen

---

**Työn ohjaaja** Ari Kankkunen

---

**Päivämäärä** 22.03.2019**Sivumäärä** 65 + 5**Kieli** Englanti

---

### Tiivistelmä

Biomassoihin ja jätteisiin perustuvia korkean viskositeetin nestemäisiä polttoaineita kohtaan on ollut kiinnostusta höyrykattila ja poltinsovelluksissa. Kyky ruiskuttaa tällaisia polttoaineita sallisi jalostusvaiheiden vähentämisen raskaille polttoaineille ja laajamittaisemman kuivauksen hyödyntämisen vesipitoisille polttoaineille. Kyseisten polttoaineiden ruiskutus on haastavaa ja energiantensiivistä. Tästä johtuen ruiskutukseen tarvitaan ominaisuuksiltaan suotuisa suutintyyppi kuten esimerkiksi pyörresuutin. Tämän tutkimuksen tavoitteena on tutkia tarkoitukseen suunnitellun isokokoisen pyörresuuttimen suihkun muotoa ja nestejakaumaa. Tutkimuksessa ruiskutettiin vesi-glyseroliseosta 2 – 3 l/s viskositeetin ollessa alueella 150 – 225 mPas. Valittu viskositeettialue vastaa joidenkin raskaiden polttoöljyjen, paperiteollisuuden biomassaliuoksien ja nopealla pyrolyysillä tuotettujen bioöljyjen viskositeetteja. Ulostulokulmat, nestekalvon nopeus ja nestejakauma määritettiin suurnopeuskameralla ja mekaanisella keräimellä. Suurnopeuskameran tuottamista videoista kerättiin dataa tarkoitukseen kehitetyllä Matlab-koodilla ja ImageJ-ohjelmalla. Suihkun ulostulokulma oli keskimäärin 50° ja 55° edestä ja sivulta katsottuna. Keskimääräinen kalvon nopeus oli tilavuusvirrasta riippuen 7 – 12 m/s, minkä perusteella voitiin arvioida, että ilmaytimen koko oli 24 – 35 % ulostuloaukon koosta. Vastaavat kalvon paksuudet vaihtelivat välillä 4 – 6 mm. Tutkittu suutin tuotti epäsymmetrisen suihkun, jonka epäsymmetria vahvistui syötetyn nesteen viskositeetin kasvaessa. Syöttöpaineen lisäyksellä oli päinvastainen vaikutus.

---

**Avainsanat** vesi-glyseroliseos, pyörresuutin, ulostulokulma, nestekalvon nopeus, nestejakauma, mekaaninen keräin

---



---

**Author** Santeri Henrik Koivisto

---

**Title of thesis** Spray characteristics of a pressure-swirl atomizer while injecting high-viscosity liquid

---

**Master programme** Energy Technology

**Code** K3007

---

**Thesis supervisor** Mika Järvinen

---

**Thesis advisor** Ari Kankkunen

---

**Date** 22.03.2019

**Number of pages** 65 + 5

**Language** English

---

## **Abstract**

There has been interest towards combustion of high-viscosity biomass and waste based liquid fuels in boiler-type applications. The ability to directly inject these types of fuels at high viscosity would allow a reduced number of refinement-steps for heavier fuels, while allowing more extensive drying to be employed for fuels with high water content. However, the injection of such fuels is challenging and energy intensive, thus requiring a nozzle-type such as the pressure-swirl nozzle, which is advantageous for handling liquids with high viscosity. The goal of this research was to study the spray shape and liquid distribution of a specifically designed large pressure-swirl nozzle. This involved injecting high-viscosity water-glycerol mixture at 2 – 3 l/s with a viscosity range of 150 – 225 mPas. The chosen viscosity range reflects the properties of some high-viscosity liquid fuels such as heavy fuel oils, liquors from the pulping industry and bio-oils from fast pyrolysis. The spray angles, film velocity and liquid distribution were evaluated using high-speed imaging and mechanical patternation. The videos were analyzed using a specifically designed Matlab-code and ImageJ software. The total spray angle was 50° and 55° on average from the front and side view, respectively. The average film velocity was found to be 7 – 12 m/s depending on flow rate. Based on this, the average air-core size was estimated to be 24 – 35 % of the exit orifice area, and the corresponding film thicknesses were 4 – 6 mm. The studied nozzle produced apparent asymmetries into the emerging spray. The asymmetries were exacerbated, when injecting liquid with higher viscosity. Increasing the injection pressure had the opposite effect.

---

**Keywords** water-glycerol mixture, swirl nozzle, spray angle, film velocity, liquid distribution, mechanical patternator

---

## Forewords

*The goal of this thesis was to study the spraying of high viscosity liquid with a specifically designed large pressure-swirl nozzle. It was the first experimental study with this nozzle design. Thank you to my supervisor Mika Järvinen and instructor Ari Kankkunen. You were always really helpful and provided insightful guidance. Also, thank you to Vadim Desyatnyk and Petteri Kivivuori for making the experiments possible.*

Espoo 22.03.2019

Santeri Henrik Koivisto

# Table of contents

Tiivistelmä	
Abstract	
Forewords	
Table of contents .....	1
Symbols .....	2
Abbreviations .....	3
1 Introduction .....	4
1.1 Background .....	4
1.2 Objective and outline of the work .....	5
2 Literature review .....	6
2.1 General flow characteristics .....	6
2.2 Atomization in swirl nozzles .....	8
2.3 Air-core and liquid film thickness .....	10
2.4 Spray cone angle .....	12
2.5 Liquid distribution and spray symmetry .....	21
3 Experimental .....	30
3.1 Pressure-drop measurement .....	30
3.2 Viscosity of the water-glycerol mixture .....	33
3.3 Spray angle measurement .....	35
3.4 Liquid film velocity from bubble tracking .....	38
3.5 Spray pattern measurement .....	40
4 Results and discussion .....	44
4.1 General flow characteristics .....	44
4.2 Spray cone angle and spray bend angle .....	47
4.3 Velocity of the liquid film .....	51
4.4 Estimated air-core area and liquid film thickness .....	53
4.5 Liquid distributions .....	54
5 Error analysis .....	57
5.1 Error in viscosity measurement .....	57
5.2 Error in high-speed camera measurements .....	58
5.3 Error in patternation measurement .....	59
6 Conclusions .....	60
7 Sources .....	62
Appendix 1	
Appendix 2	

## Symbols

$A_o$	[m <sup>2</sup> ]	exit orifice area
$A_a$	[m <sup>2</sup> ]	air-core area
$\bar{A}_a$	[m <sup>2</sup> ]	average air-core area
$A_{in}$	[m <sup>2</sup> ]	inlet port area
$A_s$	[m <sup>2</sup> ]	swirl-chamber area
$A_{eff}$	[m <sup>2</sup> ]	effective exit area
$C_d$	-	discharge coefficient
$C_i$	-	area correction factor
$FN$	[m <sup>2</sup> ]	flow number
$K$	-	atomizer constant
$K_\theta$	-	correction factor for the tangent of the semi cone angle
$N$	-	number of sectors in the patternator
$N_s$	-	number of required samples
$\dot{V}$	[m <sup>3</sup> /s]	volume flow rate
$Z$	[kg/m <sup>2</sup> s]	mass flux
$d_o$	[m]	exit orifice diameter
$d_s$	[m]	swirl chamber diameter
$d_p$	[m]	inlet port diameter
$d_a$	[m]	air-core diameter
$d_i$	[m]	inner pipe diameter
$g$	[m/s <sup>2</sup> ]	gravitational acceleration
$h$	[m]	patternator distance from nozzle
$l_s$	[m]	swirl chamber length
$l_o$	[m]	exit orifice length
$l$	[m]	pipe length
$\dot{m}$	[kg/s]	mass flow rate
$n$	-	index of frictional decay in the vortex motion
$p_A$	[Pa]	ambient pressure
$r_a$	[m]	air-core radius
$\bar{r}_a$	[m]	average air-core radius
$r_s$	[m]	swirl chamber radius
$r_o$	[m]	exit orifice radius
$\bar{t}$	[m]	average film thickness
$\bar{v}$	[m/s]	average velocity
$\bar{v}_f$	[m/s]	average film velocity
$y_i$	[m]	height of liquid level in probe i
$y_j^*$	-	normalized height of liquid level in sector j
$\bar{y}$	[m]	average value of $y_j$
$x_i$	[m]	distance from centerline for probe i
$\theta_b$	[°]	spray bend angle
$\theta$	[°]	total spray angle
$\theta_m$	[°]	mean spray angle
$\theta_R$	[°]	right half-angle
$\theta_L$	[°]	left half-angle

$\emptyset_e$	[°]	effective spray angle
$\emptyset_{eR}$	[°]	right effective half-angle
$\emptyset_{eL}$	[°]	left effective half-angle
$\phi$	[°]	patternator angle
$\Delta p$	[Pa]	injection pressure
$\Delta p_{pipe}$	[Pa]	pipe pressure-drop
$\sigma$	-	normalized standard deviation
$\delta$	[m]	boundary layer thickness
$\varepsilon$	[m]	swirl chamber-to-exit orifice eccentricity
$\xi$	-	friction coefficient
$\xi_{in}$	-	friction coefficient for abrupt decrease in pipe diameter
$\rho_l$	[kg/m <sup>3</sup> ]	liquid density
$\mu_L$	[mPas]	liquid dynamic viscosity
$\Gamma$	-	patternation index

## Abbreviations

HFO	Heavy fuel oil
-----	----------------

# 1 Introduction

## 1.1 Background

Different types of nozzles are employed in various applications such as combustion of liquid fuels in power plants, gas turbines and engines, spreading of pesticides in agriculture, spray drying, spray coating, and fire extinguishing. The nozzle performance often plays a key role in the quality of end product or the efficient use of resources. Therefore, a lot of research has been dedicated towards understanding the inner-workings of nozzles and how changes in the design and operating parameters can facilitate improvements in terms of economic feasibility, environmental impact and overall efficiency.

Nozzles are especially important in the combustion of liquid fuels, since these fuels constitute a large share of the used energy sources in the transportation and energy sector. For liquid fuels, the atomization performance of the nozzle determines not only the combustion efficiency, but also the extent to which emissions are produced. Furthermore, the importance of the fuel injection and nozzle design will be emphasized in the future due to stricter emission standards and usage of waste- and biomass-based liquid fuels. These unconventional fuels are often characterized by relatively high moisture content, low volatility, and the necessity for pre-processing before combustion. The pre-processing can improve the quality of the fuel for example by reducing the moisture content with some form of drying or by upgrading the biomass feedstock into bio-oil through a fast pyrolysis process. Both methods result in a higher dry-solids content, thus increasing the viscosity and the heating value of the fuel. For example, the viscosity of the bio-oils can vary in the range 35 – 1000 mPas at 40 °C depending on the used biomass- or waste-feedstock. This is because the used feedstock affects the composition of the produced bio-oil: for example, the oxygen and water content of the fuel. (Czernik & Bridgwater 2004).

Similar viscosity ranges are encountered in the case of heavy fuel oils (HFOs), which are often used to fuel ships and oil-boilers. In Finland, for example, the annual consumption of HFO was reported to be around 650 000 tonnes (Lehto et al. 2013). In recent years, bio-oils have been suggested as a potential alternative to reduce the use of HFOs. The HFOs are classified into different categories depending on the viscosity, which can vary in the range of 10 – 700 mPas at 50 °C (International Organization of Standardization 2017).

Furthermore, in the pulping industry, drying is employed to enhance the combustion characteristics of the black liquor side-product. As a side effect of drying, the liquid viscosity is also increased. For example, Miikkulainen (2006) studied spraying of black liquor with 75 – 79 % dry-solids content at 129 – 135 °C. With these parameters, the viscosities were measured to be in the range of 90 – 260 mPas. However, the benefits of having such a high dry-solids content outweigh the detrimental effects of the increased viscosity. This is because the higher dry-solids content not only improves the fuel heating value, but also the in-flight properties of the droplets. The higher energy content in the fuel increases the combustion temperature in the char bed, thus leading to a better combustion efficiency. The in-flight properties are improved due to the increased mean size and density of the droplets, which reduces the propensity for carry-over in the upwards gas flow. This affects the boiler operation, since excessive carry-over results in fouling and corrosion of the heat exchanger surfaces. (Adams et al. 1997.)



Generally, fuels are upgraded to improve the combustion characteristics, thus benefiting the operation of a power plant. Furthermore, in the case of liquefaction via fast pyrolysis, also the storage and transportation of the fuels become easier. However, these types of upgrades also have the negative side-effect of increasing the fuel viscosity. This makes pumping and injection of the fuels more challenging and energy intensive. Therefore, it is necessary to employ a nozzle type, which is well suited for injecting high-viscosity fuels and liquids: for example a pressure-swirl nozzle. In this nozzle type, the flow enters a swirl chamber through tangential inlet ports. This creates a swirling flow, which is characterized by the formation of an air-core. The pressure-swirl nozzle has two main advantages. Firstly, the atomization performance is very good due to the hollow cone flow regime, which increases the spray angle, the discharge velocity, and the amount of air-to-spray interaction, thus reducing the size of the droplets. Secondly, the energy consumption is low in comparison to other nozzle types, thus yielding good liquid throughputs with less energy (Khavkin 2004).

The pressure-swirl nozzle seems promising for injection of high-viscosity liquid, since research suggests that increasing the flow viscosity with constant injection pressure may actually increase the liquid through-put for this nozzle type. Wimmer and Brenn (2013) observed that increasing the viscosity of the flow, while keeping the injection pressure constant, reduced the diameter of the air core. This corresponded to an increase in the liquid film thickness at the exit orifice, thus increasing the effective exit area. The increased effective exit area allowed a higher flow rate through the nozzle. The utility of this is clear for large-scale industrial processes, where moderate-to-high viscosity liquids or slurries are being used. Having a higher mass flow rate with similar or reduced power input to the pump increases the process efficiency. Alternatively, since the nozzle can handle liquids with higher-viscosities, more extensive drying can be employed to increase the dry-solids content of the injected liquids.

Furthermore, the size of the nozzle seems to affect the flow friction such that larger nozzles can be used to inject liquids with higher viscosity. Ballester and Dopazo (1994) demonstrated that the effect of viscosity to be more prominent for smaller atomizers. This suggests that the effect of viscosity may be reduced by increasing the nozzle size. However, increasing the nozzle size can have a detrimental effect on the atomization quality due to the increased thickness of the emerging liquid film, which is an important predictor of droplet size. This has been confirmed by experiments showing that the mean drop size is roughly proportional to the square root of the thickness of the liquid film. (Lefebvre & Vincent 2017.) Thus, with scaling the nozzle size, there is a trade-off between obtaining reduction in flow friction and maintaining the appropriate droplet size.

## **1.2 Objective and outline of the work**

The pressure-swirl nozzles have utility for large-scale applications, which demand the injection of high-viscosity liquids at high flow rate. The aim of this thesis was to study the nozzle pressure drop, spray angle, film velocity and liquid distribution of a specifically designed large pressure-swirl nozzle, while injecting a high-viscosity liquid at standard ambient conditions. These characteristics were studied using high-speed photography and mechanical patterning. This also demanded the development of measurement and analysis techniques, which were compatible with the limited budget, novel nozzle design, and injection of highly viscous liquid. The injected liquid was a mixture of water and glycerol, which is discussed in more detail in the experimental section. The tests were conducted with a flow rate varying between 2 – 3 l/s at a viscosity range of 150 – 225 mPas, which reflects the viscosity of some HFOs, bio-oils and other high dry-solids content biomass based liquid fuels.

The studied pressure-swirl nozzle is a novel design with a single tangential expanding inlet port on one side of the swirl chamber. The expanding entrance reduces flow resistance and probability of clogging issues. The design also compensates for the one-sided inlet port by having the exit orifice placed non-concentrically with respect to the nozzle axis. Therefore, it is of interest to study the effects of the design on the spray pattern and shape of the spray for high-viscosity liquids.

The structure of the thesis is as follows. Chapters 2 gives a short introduction to flow in pressure-swirl nozzles, the spray angle, and the spray patternation. Chapter 3 describes the measurement setups used for both the patternation and the high-speed photography. Chapter 4 presents the results and Chapter 5 evaluates the relevant error sources. Chapter 6 draws conclusions about the findings.

## 2 Literature review

### 2.1 General flow characteristics

There are various quantities that can be used to describe the nozzle flow characteristics. Here, we decided to include flow number (FN), discharge coefficient ( $C_d$ ), and Reynolds number ( $Re$ ). To evaluate the first two, it was necessary to determine the pressure drop in the nozzle, since both FN and  $C_d$  are functions of the injection pressure ( $\Delta p$ ). Reynolds number was used in correcting the pressure data to calculate the pressure-drop across the nozzle. This calculation is shown in Chapter 3.

The Reynolds number describes the ratio between the inertial forces and viscous forces, where the former acts to increase the momentum of the flow and the latter acts to decelerate it. This dimensionless number is useful for assessing whether the flow is laminar or turbulent in nature. The limits are typically set such that the pipe flow is laminar at  $Re < 2300$ , turbulent at  $Re > 2900$ , and in a transitional state, if the flow is in between these two values. The Reynolds number for pipe flow is calculated as

$$Re = \frac{\rho_l v d_h}{\mu_l}, \quad (1)$$

where  $\rho_l$  = liquid density,  $v$  = mean velocity of the flow,  $d_h$  = hydraulic diameter, and  $\mu_l$  = liquid viscosity.

Even if the flow is laminar at the nozzle inlet or the pipe leading to it, it is not self-evident that the flow will remain laminar after it enters the nozzle. For example, the flow might become turbulent at the exit orifice due to the high velocities. According to Khavkin (2004, p. 180 - 181) low Reynolds numbers for flows with a large tangential velocity component can correspond to very high Reynolds numbers in straight flows. This seems to suggest that turbulence could occur even with low inlet Reynolds numbers in pressure-swirl atomizers, where the tangential velocity component can be quite high. On the contrary, Chinn et al. (2008) suggested that if turbulence occurs at the inlet channel, it is not necessarily maintained in the body of the atomizer due to the radial acceleration in the swirling flow. This tends to laminarize the flow by restricting fluctuations in the radial direction. However, if the ratio of the boundary layer thickness to swirl chamber radius is very small ( $\frac{\delta}{|r_s|} \ll 1$ ), the stabilizing influence of the wall curvature is less important (Schlichting & Gersten 2000, p.480). Thus, both the geometry of the nozzle and the viscosity of the injected liquid can affect whether the laminar-to-turbulent transition occurs inside the nozzle or not.

The flow number ( $FN$ ) is another important parameter for describing the flow through an atomizer. According to Lefebvre and Vincent (2017), the standard flow number is typically defined as the effective flow area of the nozzle and expressed as the ratio of the nozzle flow rate to the square root of the injection pressure. They also mention that the calculated flow number is traditionally engraved on the side of the nozzle. The standard flow numbers used in US and UK can be expressed as:

$$FN_{US} = \frac{\text{Flow rate [lb/h]}}{\sqrt{\text{Injection pressure [psid]}}}, \quad (2)$$

$$FN_{UK} = \frac{\text{Flow rate [UK gal/h]}}{\sqrt{\text{Injection pressure [psid]}}}. \quad (3)$$

Note that the used units differ for the US and UK flow numbers, and thus different values of flow number are obtained depending on which definition is used. These flow numbers can have significant errors, when used in calculations unless injecting standard calibrating fluid with density of  $\rho_l = 765 \text{ kg/m}^3$ . To obtain a more appropriate description for the flow number, Lefebvre and Vincent (2017) suggested the following equation:

$$FN = \frac{\dot{m}}{\sqrt{\Delta p \rho_l}}, \quad (4)$$

where  $\dot{m}$  = flow rate (kg/s),  $\Delta p$  = injection pressure (Pa), and  $\rho_l$  = liquid density (kg/m<sup>3</sup>).

This produces a dimensionally correct flow number, which is constant regardless of the liquid density. Although this definition is better, the usage of the traditional definition remains a standard practice. Therefore, to compare different nozzles, it may sometimes be necessary to express the flow number in the old format. The following equations can be used to get standard flow numbers ( $FN_{US}$  and  $FN_{UK}$ ) from  $FN$  (Lefebvre & Vincent 2017):

$$FN_{US} = 0.66 \cdot 10^6 \cdot \rho_l^{0.5} \cdot FN, \quad (5)$$

$$FN_{UK} = 0.66 \cdot 10^8 \cdot \rho_l^{-0.5} \cdot FN. \quad (6)$$

Similarly, the flow can be described using the discharge coefficient ( $C_d$ ). One of the main benefits of using the discharge coefficient is its dimensionless form, which allows the comparison of nozzle flow characteristics for different size nozzles. According Zhike et al. (2014) the discharge coefficient is defined as the ratio of the actual mass flow rate to the ideal:

$$C_d = \frac{\dot{m}}{\dot{m}_{ideal}}, \quad (7)$$

where the ideal mass flow rate can be calculated from:

$$\dot{m}_{ideal} = A_o (2\rho_l \Delta p)^{0.5}. \quad (8)$$

Thus, by combining (7) and (8), we get:

$$C_d = \frac{\dot{m}}{A_o(2\rho_l\Delta p)^{0.5}}, \quad (9)$$

where  $\Delta p$  = pressure drop across the nozzle,  $\dot{m}$  = measured mass flow rate, and  $A_o$  = exit orifice area.

## 2.2 Atomization in swirl nozzles

There are two variables that are typically used, when describing the nozzle atomization performance. These are the mean droplet size and the droplet size distribution. In some applications, it is necessary to have a narrow range of droplet sizes. For example, when spreading pesticides, the typical demand is to obtain a droplet size range of 200 – 400  $\mu\text{m}$ , since depending on the wind conditions, droplets with a diameter of less than 200  $\mu\text{m}$  can drift away from the application region (Swithenbank et al. 1985).

The swirl nozzle is unique in the sense that it produces conical liquid film, which has special properties in terms of atomization. This liquid film first breaks into ligaments and then disintegrates further into droplets of varying size. Kooij et al. (2018) studied how ligaments affected atomization for a flat fan nozzle and a swirl nozzle with viscosity and surface tension varying in the range 1 – 32 mPas and 23 – 72 mNm<sup>-1</sup>, respectively. The study was conducted using high-speed photography to determine the mean diameter and corrugation of the ligaments (see Fig. 1). These parameters were then used to assess the droplet size distribution. They found that the droplet size distribution depended on liquid surface tension, nozzle type and injection pressure, whereas liquid viscosity seemed to have a negligible effect. According to Kooij et al. (2018), the droplet size distribution results from the dispersion of droplets formed from the disintegration of a single ligament, and also from the distribution of the ligament sizes in the spray. They observed a measurable difference in the droplet size distributions for the flat fan nozzle and the swirl nozzle. This was attributed to the swirl nozzles ability to produce extremely uniform ligament sizes in comparison to the flat fan nozzle.

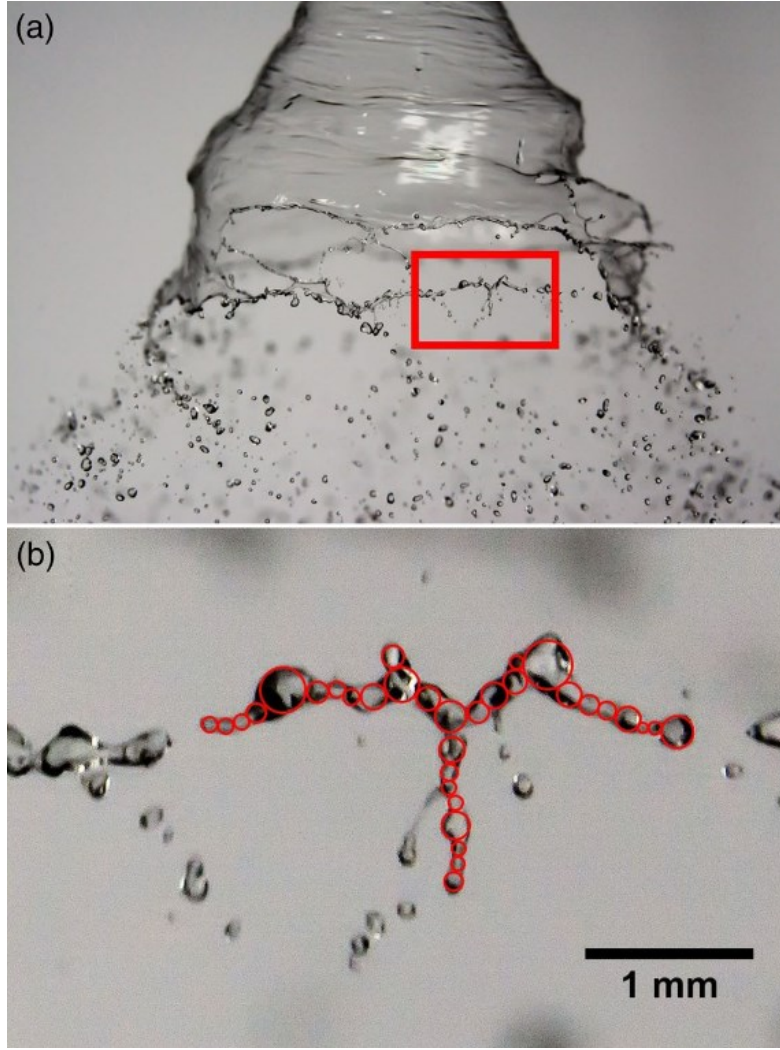


*Figure 1. a) Hollow cone spray produced by Albuz ATR 80 nozzle at injection pressure of 1.0 bar, and b) zoomed ligament framed in inscribed circles, which allow the determination of ligament corrugation and mean diameter of the ligament (Kooij et al. 2018).*

Another distinction to consider is that the properties of the spray change depending on whether the atomization occurs inside the nozzle exit orifice or after some distance from the nozzle. These flow types are described as film forming and non-film forming flows. The atomization quality was found to be worse for the film forming spray disintegration. Whether the spray is film forming or not is determined by the discharge velocity, which is a function of liquid viscosity. As the flow velocity is increased the break-up length of the liquid film is shortened until it disappears completely (Khavkin 2004, p. 165). In this case, the atomization occurs at the exit orifice.

Furthermore, the geometry of the nozzle has an important role in the atomization performance of a swirl nozzle. For example, Jones (1982) optimized a large pressure-swirl nozzle design, which was commonly used in 500 MW oil-fired boilers. They formulated an empirical formula based on experiments, which suggested that atomization performance would improve by reducing swirl chamber length ( $l_s$ ), swirl chamber diameter ( $d_s$ ) and exit orifice length ( $l_o$ ), and by increasing exit orifice diameter ( $d_o$ ). In essence, this would decrease the internal wetted surface area, thus decreasing the losses due to flow friction.

Jones (1982) also mentioned that  $l_o$  could be reduced only to a certain extent, since the atomizer had to maintain its structural integrity. Therefore, the optimization should aim at reducing the swirl chamber dimensions as much as possible. For example, it was suggested that  $l_s$  could be minimized to the point, where it was equal to the height of the inlet channels. Furthermore, reduction in the inlet channel area was also found to be beneficial, although there was a limit due to the potential blockage of the channels. The optimization was required to maintain a constant through-put, and thus  $d_o$  was increased to counter-balance the effects of the changes in the other parameters. These changes yielded a 12 % decrease in mean droplet size. (Jones 1982.)

All of these effects on the droplet size of the nozzle can be tied to the thickness of the liquid film and the state of the air-core, since they are interrelated phenomena. For example, the thickness of the formed ligaments is a function of the liquid film thickness, which changes based on the stability and shape of the air-core.

### **2.3 Air-core and liquid film thickness**

In the pressure-swirl nozzle, the tangential inlets form a swirling flow with a large tangential velocity component. The centrifugal forces produced by the swirling motion push the liquid against the walls of the swirl chamber, thus creating a low-pressure zone near the axis of the nozzle. At sufficiently high inlet Reynolds numbers, the inception of an air core occurs at the exit of the nozzle, followed by an expansion across the entire length of the nozzle (Amini 2016). The air-core forces the liquid to exit the nozzle as a thin liquid film, thus increasing the spray angle and the discharge velocity. The velocity of the liquid film is inversely proportional to the film thickness, since the effective exit area is reduced. This reduces the droplet size not only due to the increase in aerodynamic drag, but also due to the thinner film breaking up into ligaments of smaller diameter, which then disintegrate into droplets.

The air-core has been studied extensively due to its profound effect on the atomization performance. For example, Kim et al. (2009) studied the effect of swirl injector geometry on the air-core and the thickness of the liquid film using high-speed photography and electrical conductance measurement, respectively. The adjustable parameters were length of the swirl chamber and its extension, length of the exit orifice, and diameter of the swirl chamber. They found that certain changes in these parameters, such as having a swirl chamber length-to-diameter ratio ( $\frac{l_s}{d_s}$ ) of 1.27 or higher, produced instability in the air-core. The unstable air-core formed a complex helical shape. Fig. 2 shows how the effects of the instability were also detected as fluctuations in the thickness of the liquid film. This illustrates that there is a link between the behaviors of the air-core and the liquid film.

Kim et al. (2009) concluded that the instability of the air-core was a function of viscous effects, swirl chamber geometry and the inlet Reynolds number. However, if a geometry was prone to instability, increasing the injection pressure did not seem to stabilize the air-core. This was due to the increase in momentum being less than the increase in flow friction as the injection pressure was increased, which suggests that the velocity inside the swirl chamber was not sufficiently high to support a stable air-core.

According to Som (2012), the shape of the air-core is not only dependent on whether the swirl chamber is conical or cylindrical, but also whether the exit orifice is abrupt or has a finite length. Firstly, the conical swirl chamber seems to produce a more cylindrical air-core, whereas the cylindrical swirl chamber results in a helical air-core. This seems to suggest that the conical chamber increases the air-core stability. Secondly, adding length to the exit orifice creates an increase in the diameter of the air-core at the exit.

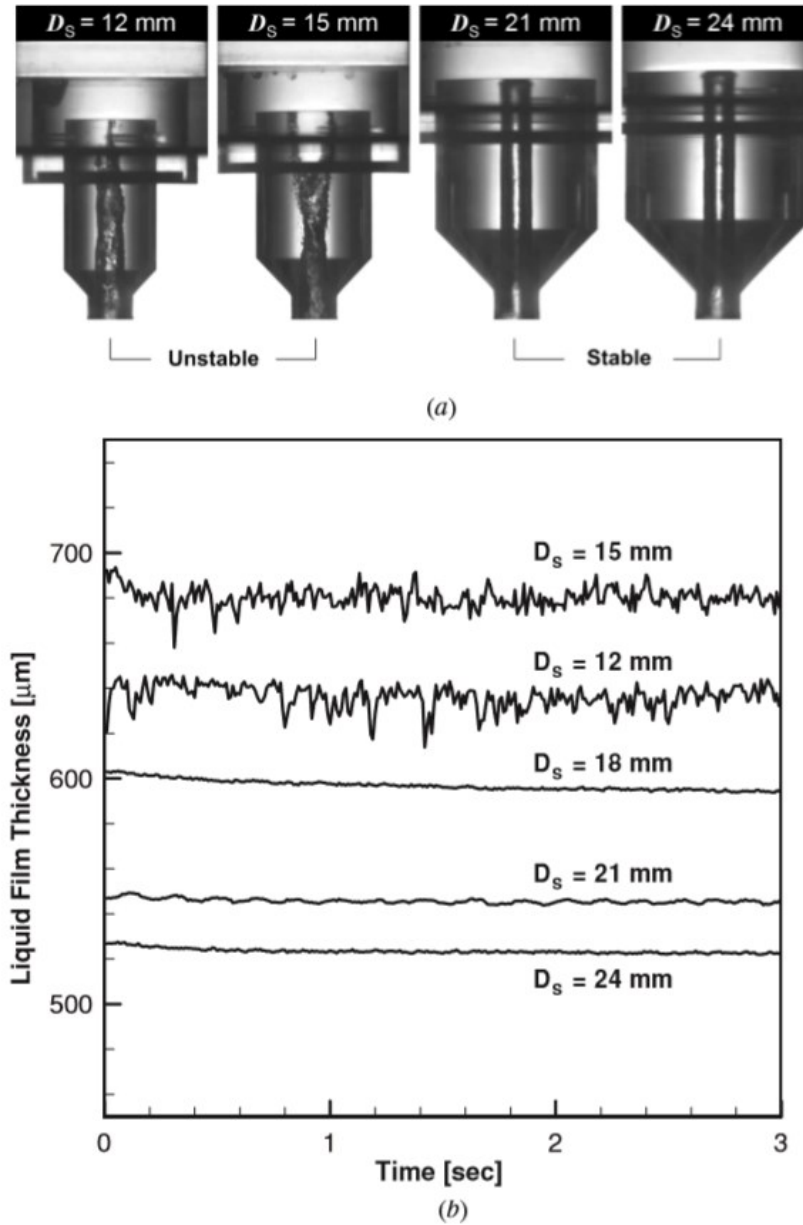


Figure 2. Effects of swirl chamber diameter: a) on the stability and shape of the air-core and b) on the film thickness ( $\Delta p = 10$  bar) (Kim et al. 2009).

Halder et al. (2002) studied the relationship between the formation of the air-core and the Reynolds number at the inlet. They found two limit values for the Reynolds number: one below which the inception of the air-core would not occur, and another one above which a fully-developed air-core was always observed. These limit values decreased with increasing orifice-to-swirl chamber diameter ratio ( $\frac{d_o}{d_s}$ ) and decreasing inlet port-to-swirl chamber diameter ratio ( $\frac{d_p}{d_s}$ ). According to Som (2012), the formation of the air-core occurs due to the low-pressure region, which forms at the nozzle axis with sufficiently high swirl strengths. Thus, the above findings can be explained in terms of flow resistance and tangential velocity of the flow. For example, having a larger exit orifice reduces the flow resistance of the nozzle, and thus more energy is available to drive the swirling motion. On the other hand, decreasing the inlet port diameter increases the tangential velocity

component of the flow, thus being favorable for the formation of the air-core. However, smaller inlet ports also tend to increase the flow resistance, which could potentially restrict the formation of the air-core. (Som 2012.)

Som and Mukherjee (1980) studied the formation of an air-core in a conical swirl nozzle with varying orifice diameters and swirl chamber angles. Their results showed that increasing the inlet Reynolds number produced an initial increase in the air-core diameter. However, with further increase, the diameter reached a limit value beyond which it stayed a constant. This constant diameter was not only higher for nozzles with larger  $\frac{d_o}{d_s}$ , but it was also reached at a lower inlet Reynolds number. The effect of the swirl chamber angle was similar: a larger swirl chamber angle produced an air-core with a larger diameter.

Datta and Som (2000) studied the air-core diameter ( $d_a$ ), coefficient of discharge ( $C_d$ ), and spray cone angle ( $\theta$ ) numerically. Their results showed a sharp increase in  $d_a$  and  $\theta$  together with a decrease in  $C_d$  in the lower end of the flow rate range. In the higher flow rate range,  $d_a$ ,  $C_d$  and  $\theta$  become close to independent of flow rate. Clearly, the swirling strength of the flow reaches an equilibrium, where the frictional decay of the swirling motion increases at the same rate as the addition of swirling strength by the flow entering the swirl chamber. In the lower end of the flow rate range, the increase in swirling motion is the dominant effect. (Datta & Som 2000.) Firstly, these numerical results demonstrated that there exists a maximum diameter for the air-core for a given nozzle geometry, thus being in agreement with previous findings by Som and Mukherjee (1980). Secondly, this showed the close dependence between  $C_d$ ,  $\theta$ , and the state of the air-core.

Therefore, it was also of interest to study the lower flow rate ranges, where the air-core was still in its developing stages. This type of study was conducted by Reddy and Mishra (2008), who encountered a few different types of flow regimes, which were dependent on the state of the air-core. These were denoted as collapsed cone, unstable hollow cone, and fully-developed hollow cone flow. They studied how the spray angle, discharge coefficient, liquid distribution and drop size changed, when going from a collapsed air-core to a transitional flow regime. Their results showed that the spray angle did not change much at low injection pressures. They attributed this to the injection pressure being insufficient to overcome the surface tension forces in the flow. However, with further increase in injection pressure, the centrifugal forces became dominant, and thus the spray angle began to increase monotonically. In terms of spray patternation, the collapsed hollow cone produced a higher mass flux at the center, whereas with the developing hollow cone flow regime, the mass fraction at the center of the spray was reduced. (Reddy & Mishra 2008.)

## 2.4 Spray cone angle

The spray structure can be defined in terms of either the visual or the effective spray angle. The visual spray angle is obtained from spray images by detecting the boundary of the spray. The boundary is straight in the immediate vicinity of the nozzle exit, but slightly curved inwards some distance from the nozzle. This curving inwards occurs due to aerodynamic effects that are imparted on the liquid film as it moves through the ambient gas at high velocity. Due to the curved boundaries, the spray angle can have different values depending on the chosen measurement cross-section. Thus, there are two distinct ways to define the spray angle. One of them is described as the maximum cone angle, which is obtained by measuring the tangent in the region near to the nozzle. More commonly, however, a straight line is drawn from the exit orifice to a point on the spray contour, which forms an angle with respect to the axis of the nozzle. (Rizk & Lefebvre 1987.) This yields two half-angles ( $\theta_L$  and  $\theta_R$ ), which can be summed up to obtain the total spray angle ( $\theta$ ). Furthermore, as the half-angles are often dissimilar, the spray appears to be skewed



to one side, thus forming an angle between the nozzle axis and the visual midline of the spray. This angle is defined as the spray bend angle ( $\theta_B$ ). Note that the bend angle is defined such that if  $\theta_L > \theta_R$ , then  $\theta_B < 0$  and vice versa. Thus, the sign of the bend angle describes, which way the spray is bent. These angles are illustrated in Fig. 3.

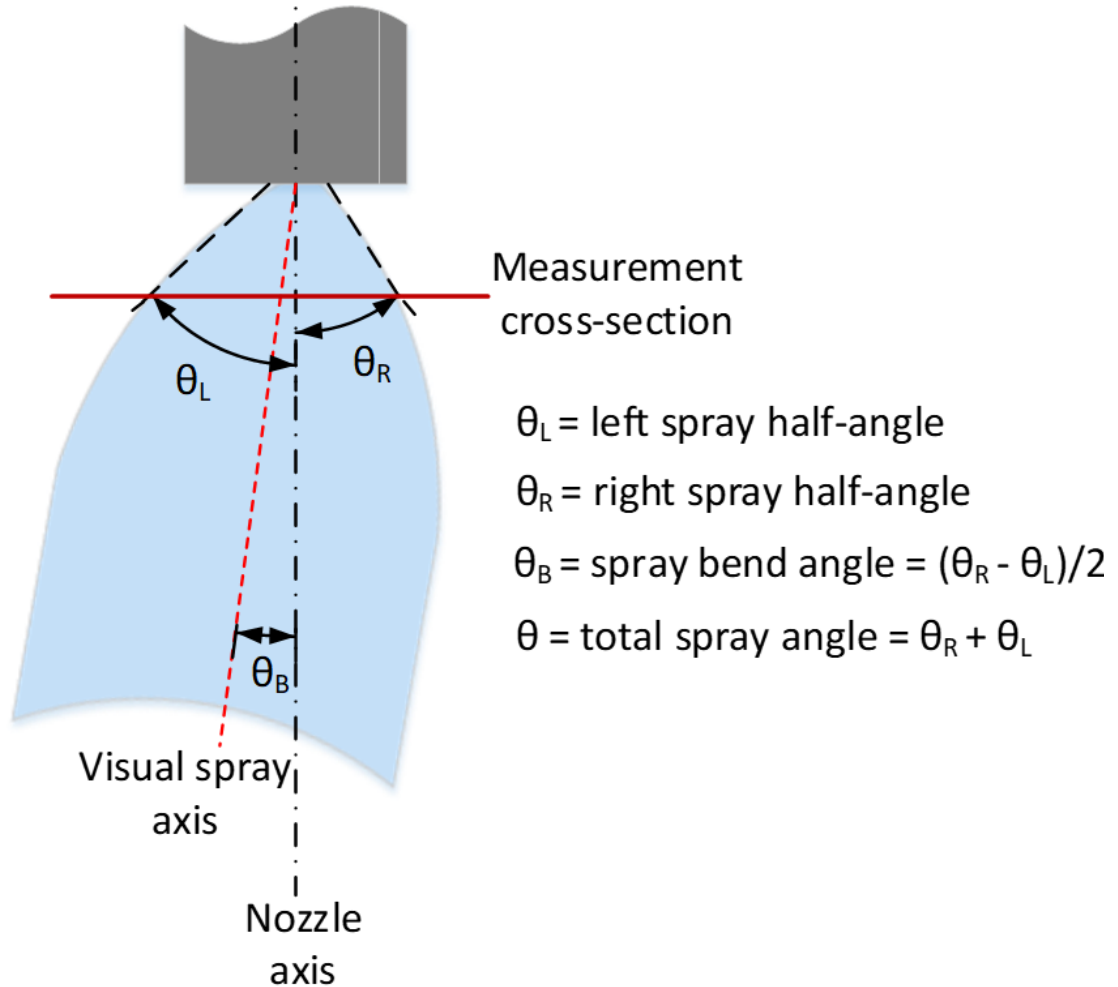


Figure 3. Representation of visual spray half-angles, total spray angle, and spray bend angle based on image analysis.

The fluctuating surface waves make the spray contour change constantly, and thus a single image is insufficient to give an accurate description of the spray angle. This issue can be dealt with by calculating the spray angle for a set of images, which yields a mean, a maximum, and a minimum value for the spray angle. However, while the visible spray angle is a good source of qualitative information, it is less useful for determining quantitative relationships between variables (Chen et al. 1992). This is because it omits information on the liquid distribution, thus leaving internal changes of the spray unexpressed. For example, the spray mass flux could change with respect to some variable even for a constant visible spray angle.

Therefore, it is useful to define the spray in terms of the effective spray angle, which is based on the radial liquid distribution within the spray. The effective spray angle can be measured with reasonable accuracy and expressed in quantitative terms, since it accounts for changes in the internal structure of the spray (Chen et al. 1992). The liquid distribution can be obtained for example with a mechanical patternator. This type of patternation measurement is shown in Fig. 4.

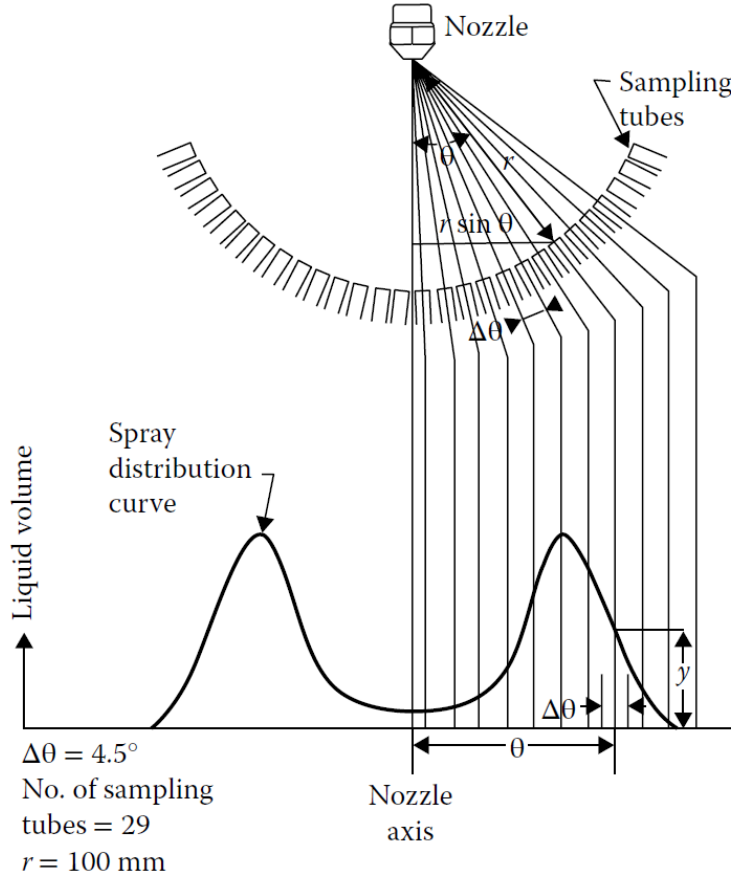


Figure 4. Measurement of radial liquid distribution with a mechanical patternator (Lefebvre & Vincent 2017).

The effective spray angle can be obtained based on the mass distribution data from the patternation measurement. Ortman and Lefebvre (1985) define the effective spray angle as the sum of the angular locations that corresponds to the centers of mass of the material system on the left and the right side of the fuel distribution. This angle can be determined using the following equations:

$$\phi_{e,tot} = \phi_{e,L} + \phi_{e,R}, \quad (10)$$

where  $\phi_{e,L}$  and  $\phi_{e,R}$  are the angular locations for the centers of mass on the left and the right sides, respectively. These angles can be calculated from:

$$\phi_{e,L/R} = \tan^{-1}\left(\frac{\left|\frac{\sum y_i x_i}{\sum y_i}\right|}{h}\right), \quad (11)$$

where  $y_i$  = height of liquid in probe  $i$ ,  $x_i$  = distance from centerline for probe  $i$ , and  $h$  = patternator distance from nozzle. The first term defines the location of the center of mass for a set of probes. This forms a triangle, when the patternator-to-nozzle distance is known. The inverse tangent function can then be used to obtain the effective spray angle for each wing of the patternator.

The spray angle can change based on multiple factors such as the properties of the injected liquid, injection pressure, ambient pressure, and nozzle geometry. The basic liquid

properties that affect liquid flow include viscosity, density and surface tension. Liquid viscosity can be considered most important, since it not only produces friction within the body of the liquid, but also at the wall-to-liquid interface, thus reducing the tangential velocity component in the flow. This can alter the spray angle, which is dependent on the relative magnitudes of the velocity components. As for the two other properties, research seems to indicate that surface tension has negligible effect on the spray angle, whereas increasing the liquid density slightly widens the spray angle. (Lefebvre & Vincent 2017.) The effects of liquid density is shown in Fig. 5.

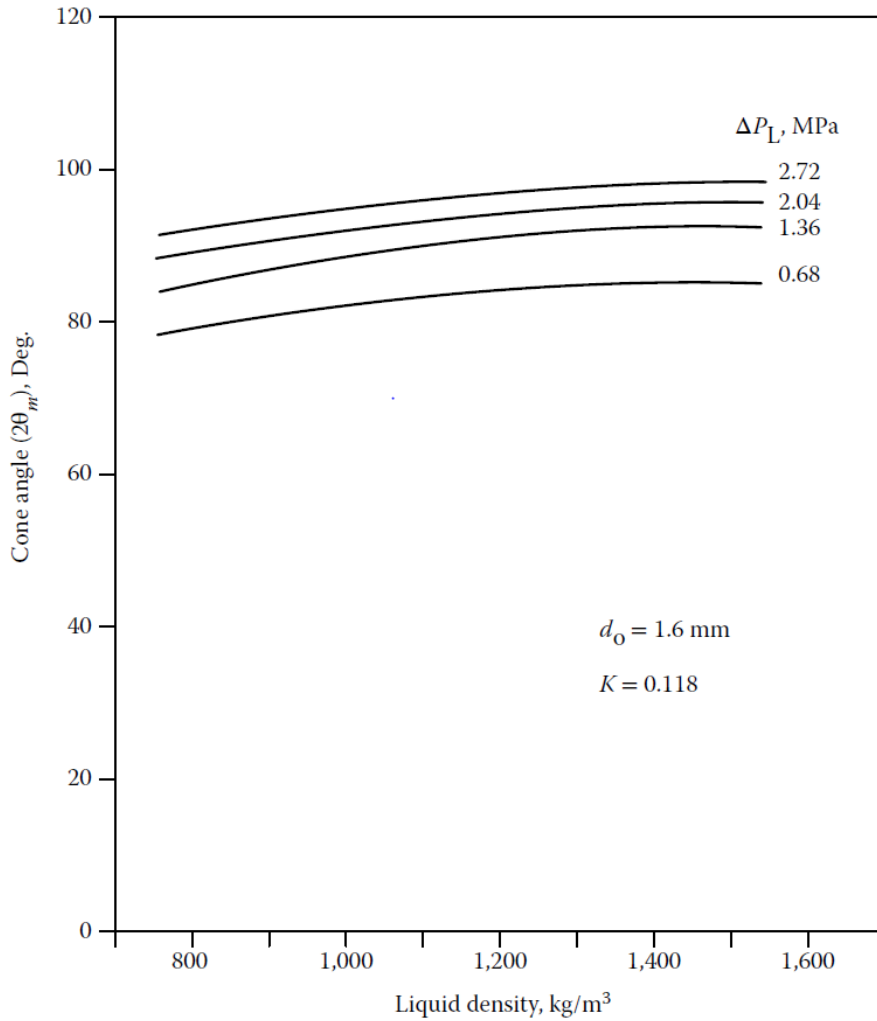


Figure 5. The mean spray angle as a function of liquid density (Lefebvre & Vincent 2017).

Therefore, many studies have focused on viscosity due to its dominant effect on the nozzle internal flow. For example, Chen et al. (1992) studied the change in spray cone angle with respect to changes in injection pressure, discharge orifice length-to-diameter ratio, and liquid viscosity. The spray angle was measured for several different simplex nozzles with three different liquid viscosities in the range 1 – 12 mPas. They found that increasing the liquid viscosity reduced the effective spray angle. This effect was more pronounced at higher viscosities. The effects of liquid viscosity is shown in Fig. 6.

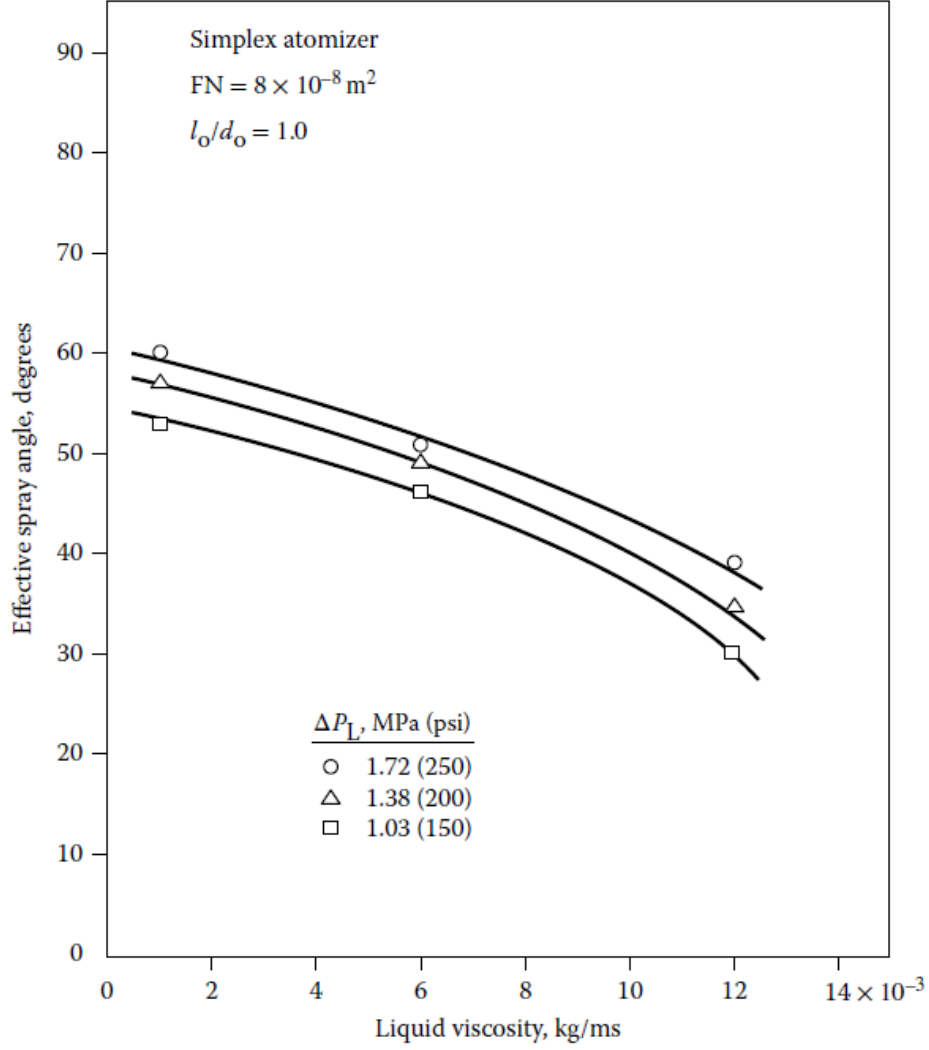


Figure 6. The effective spray angle as a function of viscosity (Lefebvre & Vincent 2017).

Similar results were also obtained by Ballester and Dopazo (1994). They examined how atomizer dimensions and injection conditions affected discharge coefficient and spray angle for small pressure-swirl atomizers. Their measurements were conducted by injecting heavy fuel oil at different fuel temperatures ranging from 20 to 120 °C with twenty small nozzles of varying geometry. As the temperature increased, they observed a 250% reduction in oil viscosity and less than 6% reduction in oil density and oil surface tension. These property changes were accompanied with a significant increase in the spray angle. This result indicated that the increase in the spray angle occurred due to the reduction in oil viscosity rather than the changes in the other liquid properties. Furthermore, this shows that the relationship between viscosity and temperature is much stronger in comparison to the other liquid properties, which were reduced only slightly over the whole temperature interval.

The geometrical features, such as orifice diameter ( $d_o$ ), inlet port diameter ( $d_p$ ), swirl chamber diameter ( $d_s$ ), orifice length ( $l_o$ ), and swirl chamber length ( $l_s$ ), can have a pronounced effect on the spray angle. For example, the spray angle expands with increasing orifice diameter, and to some extent with increasing swirl chamber diameter. Conversely, the spray angle is decreased slightly as a function of the inlet port diameter. Furthermore,

minor variation is produced by changing the lengths of the outlet orifice and swirl chamber. (Rizk & Lefebvre 1987.) Many of these parameters change the spray angle only slightly, while the orifice diameter seems to have a more significant effect in comparison as shown in Fig. 7. The studied nozzle had three inlet ports.

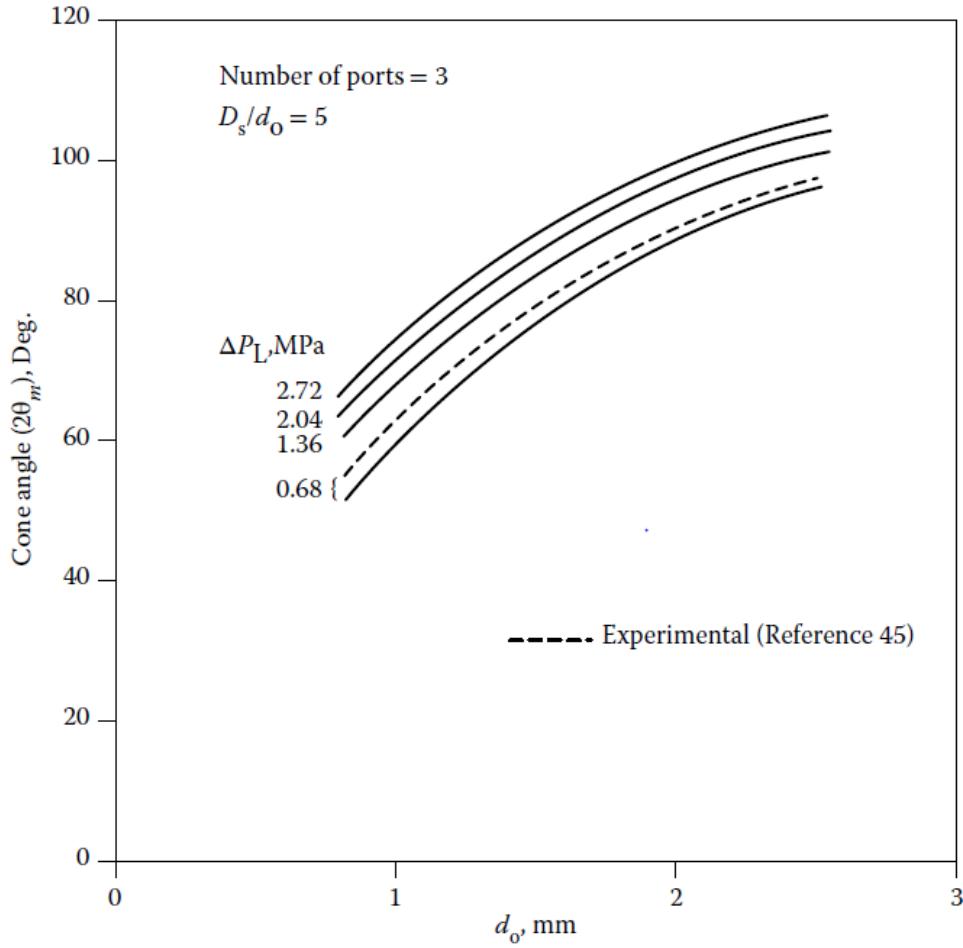


Figure 7. The visible spray angle as a function of orifice diameter (Lefebvre & Vincent 2017).

It is common practice to combine some of these geometrical parameters into dimensionless ratios, which allows their usage in empirical correlation formulas. One such useful ratio is the outlet orifice length-to-diameter ratio ( $l_o/d_o$ ). In a study by Chen et al. (1992), they observed a reduction in the effective spray angle with respect to increasing outlet orifice length-to-diameter ratio. They suggested that the narrower spray angle occurred due to the reduced swirl velocity, which could be attributed to the increase in frictional losses at the walls of the discharge orifice. Furthermore, the influence of  $l_o/d_o$  reduced with increasing viscosity and was unchanged with respect to changes in injection pressure. In their study, they also investigated the effect of the number of feed slots used. Chen et al. (1992) compared atomizers with 1 to 3 feed slots and concluded that it had a negligible effect on the spray cone angle.

De Corso et al. (1956) studied the effects of ambient and fuel injection pressure for ten swirl-nozzles. The measurements were conducted inside a pressure vessel in the pressure range of 0.01 – 0.8 MPa. They observed a significant contraction of the spray cone angle with the initial increase in the ambient pressure. However, the effect of the ambient pressure diminished with further increase. They suggested that the contraction of the spray angle was caused by aerodynamic effects, which occurred due to the motion of the spray

through the ambient gas. The high velocity liquid film encloses a portion of the ambient gas and entrains it at the inner and outer surfaces, thus creating a measurable low-pressure region within the spray boundaries. They noted that this mechanism seems to be instrumental in causing the spray angle to decrease as a function of ambient pressure.

Ortman & Lefebvre (1985) obtained similar results in their spray patternation study, thus confirming the findings of De Corso et al. (1956). Their pressure vessel was designed to withstand pressures of up to 2.0 MPa, thus allowing a much larger range of ambient pressure to be investigated. The results indicated a similar pattern of diminishing rate of contraction of the effective spray angle with respect to increasing ambient pressure. Furthermore, both authors found that increasing the injection pressure produced a consistent reduction in the effective spray cone angle. Both of these findings can be seen in Fig. 8.

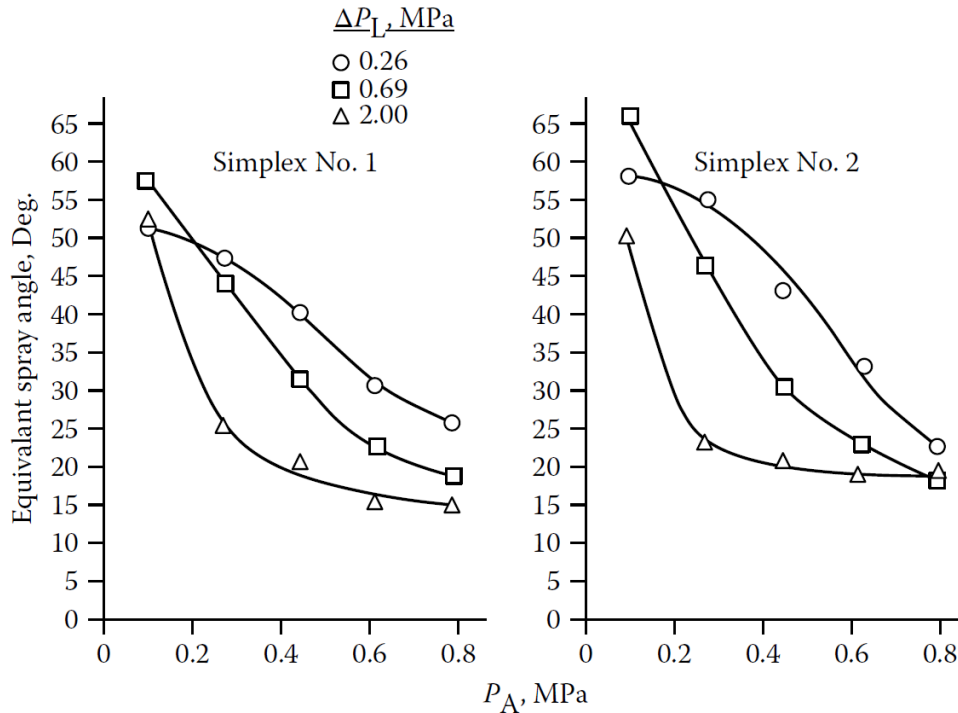


Figure 8. The effective spray angle as a function of ambient pressure for different injection pressures (Ortman & Lefebvre 1985).

At high enough ambient pressures, the spray angle was stabilized, and thus no further contraction occurred regardless of any further increases in the ambient pressure. This seemed to indicate that some type of equilibrium was reached between the ambient pressure and the low-pressure region within the spray sheath. It is worth noting that the final value of the stabilized spray angle was clearly dependent on the atomizer design. These findings are shown in Fig. 9.

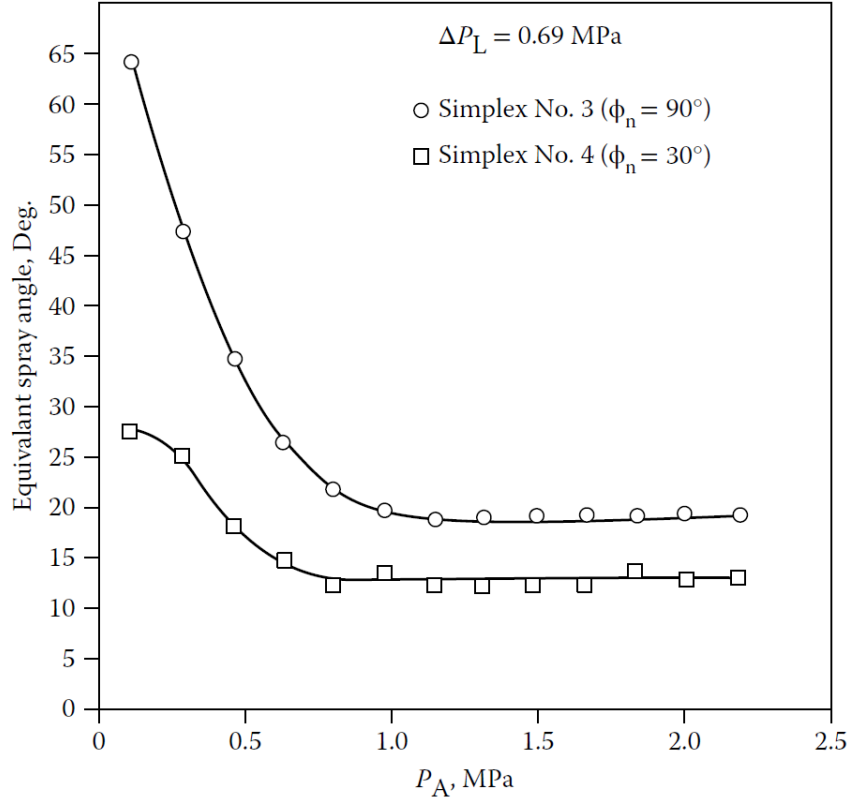


Figure 9. The stabilization of the spray angle with increasing ambient pressure (Ortman & Lefebvre 1985).

Various correlations have been proposed in the attempt to predict the spray cone angle with reasonable accuracy. One such correlation was suggested in a study by Babu et al. (1982), where they derived formulas to predict spray characteristics such as spray angle, discharge rate and air core diameter. They used the assumption of inviscid flow in their formulation. As a result, they obtained the following set of equations to describe the spray angle:

$$\tan\left(\frac{\theta}{2}\right) = \frac{(\pi/4)(1-X)K_\theta}{B}, \quad (12)$$

where

$$X = \frac{A_a}{A_o},$$

$$B = \frac{A_p}{d_m d_o} \left(\frac{d_m}{d_o}\right)^{1-n},$$

with the variables denoted as  $A_a$  = air core area,  $A_p$  = total inlet area,  $A_o$  = exit orifice area, and  $A_s$  = swirl chamber area,  $K_\theta$  = correction factor for the tangent of the semi cone angle,  $n$  = index of frictional decay in the vortex motion, and  $d_m$  = diameter based on the midpoint of the inlet channel.

They observed that the performance characteristics for each of the nozzles varied linearly with pressure in the pressure range below 2.76 MPa. Consequently, it was sufficient to obtain a correlation for 0.69 MPa, and then use that to infer the intermediate values with linear interpolation. This lead to the derivation of the following coefficient values for the two pressure ranges:

$$n = 1.1764A_o^{0.1396} \frac{A_p^{0.2336}}{A_s^{0.1775}},$$

$$K_\theta = 1.70987 \frac{A_p^{0.034048}}{A_o^{0.17548} A_s^{0.24579}},$$

for  $\Delta P \geq 2.76$  MPa, and

$$n = 1.0776A_o^{0.14176} \frac{A_p^{0.27033}}{A_s^{0.17634}},$$

$$K_\theta = 2.35109 \frac{A_p^{0.34873}}{A_o^{0.26326} A_s^{0.32742}},$$

for  $\Delta p = 0.69$  MPa.

These equations were validated by using experimental data from previous works with swirl nozzles. The equations yielded a reasonably accurate prediction for the spray angle with maximum deviation of less than 10% between predicted and experimental results. (Babu et al. 1982.) However, this equation is based purely on geometrical parameters, and thus omits the direct effects of liquid properties and injection pressure, although these effects may be taken into account to some extent by the exponents and the index of frictional decay. Apparently, the main disadvantage of this correlation formula is that it requires information on the air core size, which is not always available. Furthermore, as the formula is based on the inviscid analysis, it may be incorrect to use it for our case due to the high-viscosity liquid used in the experiments.

Rizk and Lefebvre (1987) recognized the necessity of a correlation formula, which also considers the effects of injection pressure and liquid properties. Thus, they examined how atomizer dimensions and operating conditions affected spray cone angle and velocity coefficient. They formulated an equation in terms of nozzle geometry, injection pressure, and the liquid properties. This equation describes the maximum spray angle, which is obtained in the immediate vicinity of the nozzle exit. The resulting equation is expressed as:

$$2\theta_m = 6K^{-0.15} (\Delta p d_0^2 \frac{\rho_l}{\mu_l^2})^{0.11}, \quad (13)$$

where  $K$  = atomizer constant,  $\Delta p$  = injection pressure,  $\mu_l$  = dynamic viscosity,  $d_0$  = exit orifice diameter, and  $\rho_l$  = density.

However, Ballester and Dopazo (1994) analyzed the validity of equation (13) with respect to their experimental results for small atomizers, and found significant discrepancies between the results and the correlation. They suggested that the viscosity effects had a much larger influence for smaller atomizers. Thus, based on their analysis, the following improved spray angle correlation was proposed:

$$2\theta_m = 16.156K^{-0.39} d_0^{1.13} \mu_l^{-0.9} \Delta p^{0.39}. \quad (14)$$

Both equations include not only the effects of geometry, but also the direct effects of injection pressure and liquid properties, thus yielding a more comprehensive prediction for the cone angle than the correlation suggested by Babu et al. (1982).



## 2.5 Liquid distribution and spray symmetry

Studying the spray patternation and symmetry can have utility not only for designing and improving nozzles for specific applications, but also for ensuring the quality and specificity of manufactured nozzles (Bayvel & Orzechowski 1993). The quality control aspect is especially important in applications, where nozzles are mass produced with strict quality standards such as diesel and aircraft engine nozzles. In this type of application, any maldistributions in the emerging spray can decrease the combustion efficiency and exacerbate the formation of soot and other emissions. For example, in a patternation study by Cohen and Rosfjord (1991), it was observed that an auxiliary airflow induced the collapse of a hollow cone spray, thus producing several fuel rich zones. This resulted in incomplete combustion in some areas of the gas-turbine, thus explaining the high smoke numbers and soot formation that characterized the studied nozzle type. Based on the observation, the system designer could modify the auxiliary airflow, as it was identified to be the main source for the maldistribution.

The liquid distribution and spray symmetry can be studied with a device called a “patternator”. The patternator types range from simple mechanical devices to advanced laser-sheet systems. Each of these methods have pros and cons. Mechanical devices tend to be simple and low cost method to obtain information on the spray mass distribution, whereas advanced optical measurements can yield very high resolution data. Due to the less complicated methodology, mechanical patternation can be used for verifying the performance of more sophisticated measurement techniques such as the phase-Doppler anemometry or other optical techniques (Dullenkopf et al. 1998).

Simplest mechanical patternator designs involve a disk, which is divided into several sectors that collect the flow across the circumference as in Fig. 10. However, often it is also of interest to measure the radial liquid distribution, which requires a more complicated patternator design. Radial patternators typically consist of a set of equidistant tubes that are placed in a flat or an arched formation to measure the liquid distribution for the whole spray area or a section of the spray (see Fig. 11). During the measurement, the tubes collect a certain amount of liquid, which can then be used as an indication of the spray volume flux for that tube position.

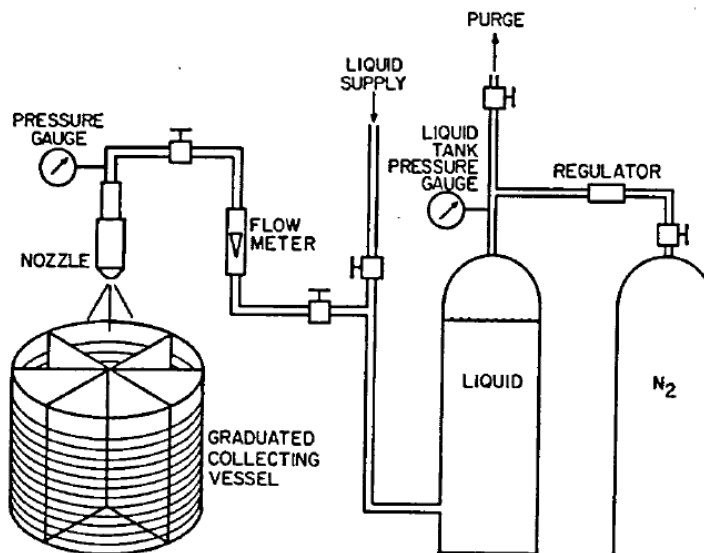
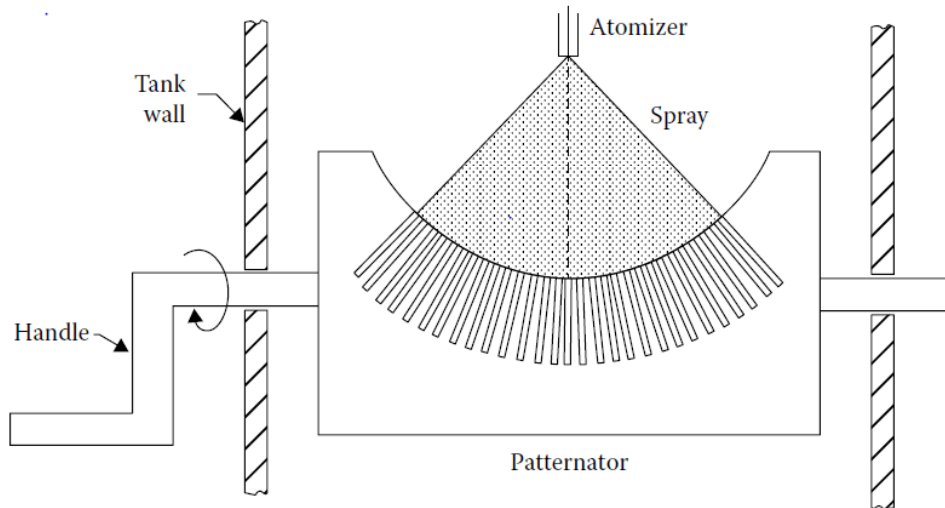


Figure 10. Schematic of a test rig using a mechanical patternator with sector division (Chen et al 1993).



*Figure 11. An arched patternator for measurement of radial liquid distribution (Lefebvre & Vincent 2017).*

Although the patterning measurement is simple, the sampling technique may introduce various errors. To ensure a good measurement, Chen et al. (1993) suggested that the nozzle should not only be well centered and properly aligned in terms of the center axis, but also placed at the appropriate distance from the patternator. This is determined by the defined patterning area, which is a function of injector scale, typical cone angle, and distance from the nozzle to the sampling plane (McVey et al. 1986).

McVey et al. (1986) described the guidelines they used to design a high-resolution patterning system, which was used in the mass flux measurement of gas turbine fuel injectors with flow rates of up to 0.16 l/s. The technique employed in measuring the spray spatial mass distribution can be classified by whether it is based on an optical or an extractive probing method (mechanical patternator). The extractive probing can be further divided into systems that capture the whole stream or only a fraction of it.

Their system was designed based on extractive probing of a fraction of the spray. They used a set of 60 sampling probes with squared and chamfered entrances, which were set in six linear arrays radiating from the center axis. They selected the probe spacing such that it could resolve variations in the spray flux with a resolution of 0.5 cm, and thus the patternator had a diameter of 10.2 cm. The relatively high resolution and small size of the patternator can be attributed to the small size of the measured nozzles. The probe arrays were shielded by closed sampling gates, which retracted for the duration of the measurement. This allowed the precise setting of sampling time, and the adjustment of flow rate prior to beginning the sample collection, thus ensuring that the whole sample was collected with the specified flow rate. Sampling time can either be limited by the volume of the collecting vessels or other practical limitations for the test duration. (McVey et al. 1986.) Their design is shown in Fig. 12.

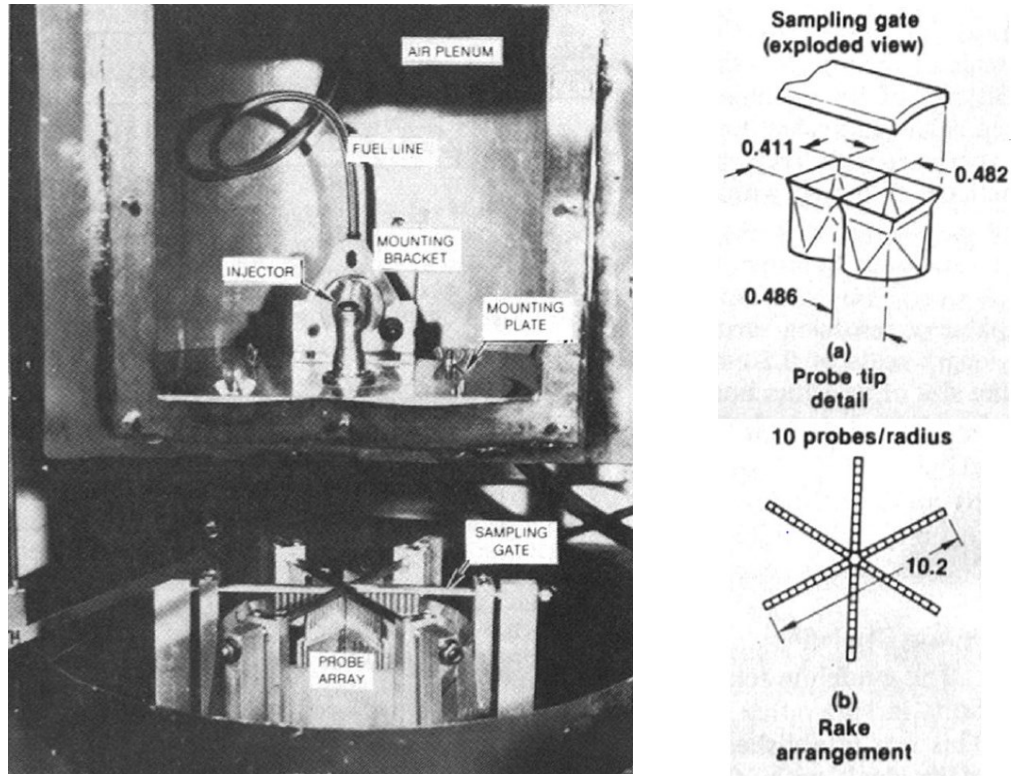


Figure 12. Mechanical patternator system: a) shows details on the probes, and b) shows the probe arrangement (all dimensions in cm) (amended from McVey et al. 1986).

To simplify their system, it was designed to operate in ambient pressure due to the considerable operating costs of a high-pressure systems. It was assumed that the detection of non-ideal performance was independent of ambient pressure. They also built the system to be operated with ambient temperature for the injected fuel and the accompanied nozzle airflow. (McVey et al. 1986.) The goal was probably to reduce the investment and operating cost of the system, although the trade-off was that the system resembles the real one to a lesser extent. The system established the impact of injector aerodynamics and hydraulic design features on spray uniformity.

As mentioned before, there are two types of liquid distributions to consider: radial and circumferential. The radial distribution describes how symmetrical the spray mass flux is with respect to the center axis, whereas the circumferential distribution refers to the way that the liquid is spread out across the sectors. This data can be presented as a fuel distribution curve, which shows the collected liquid volume as a function of the angular or radial location. These curves are useful for determining how changes in the operating parameters affect the fuel distribution. (Ortman & Lefebvre 1985.) The circumferential liquid distribution can be also obtained from the radial patterning data by summing up the liquid volumes. However, for a patternator consisting of a set of collecting vessels with a constant area across the whole radius, the liquid volumes have to be multiplied with a correction factor. This yields volume or flow rate data corresponding to a sector shaped area. The area correction factor for a collecting vessel is defined as:

$$C_i = \frac{A_{s,i}}{A_p}, \quad (15)$$

where  $A_{s,i}$  = area of the corresponding sector element, and  $A_p$  = probe area.

The values of this correction factor depend on the shape of the patternator and the way in which the sectors are defined. This is described in more detail in the experimental chapter. To describe how changes in the operating parameters affect the liquid distribution, the radial liquid distribution data can also be reduced to a single numerical value called the effective/equivalent spray angle, as mentioned in the earlier chapter (Ortman & Lefebvre 1985).

One of the earlier publications on spray symmetry and patterning was by Tate (1960). In the paper, he discussed different ways of representing circumferential patterning data such as the min-max ratio and the patterning index. The min-max ratio is obtained by dividing the smallest and largest percentage of flow collected by the sectors. However, this ratio may give an incomplete picture of the spray symmetry, since it ignores the sectors with intermediate volume percentages. The min-max ratio is defined as:

$$r_{min-max} = \frac{V_{min}}{V_{max}}, \quad (16)$$

where  $V_{min}$  = minimum volume collected, and  $V_{max}$  = maximum volume collected. As for the patterning index ( $\Gamma$ ), it is calculated by summing up the deviations from the ideal liquid distribution for each of the sectors. For example, for an eight-sector patternator, in the ideal case each sector would account for 12.5 % of the flow. Thus, if a sector collected 20 % of the flow, the deviation would be 7.5 %. The formula for  $\Gamma$  can be written as:

$$\Gamma = \sum_{j=1}^n \left| \frac{Q_j}{Q_{tot}} - \frac{100}{n} \right|, \quad (17)$$

where  $Q_j$  = volume collected in sector  $j$ ,  $Q_{tot}$  = total collected volume, and  $n$  = number of sectors in the patternator. Both of these indicators have a value of 0 for perfectly symmetrical sprays. These indicators are typically represented in terms of collected volumes instead of volume flow rates. However, if the patternator collects only a part of the sectors per measurement, flow rates should be used, as it accounts for differences in measurement durations. To obtain the flow rates, the collected liquid volumes are divided with measurement duration. Other option would be to have a constant measurement duration, thus making the measured volumes comparable.

Another alternative indicator is the patterning number ( $P_z$ ), which is defined as (Hicks et al. 2008):

$$P_z = \frac{Z_{max} - Z_{min}}{Z_{ave}}, \quad (18)$$

where  $Z_{max}$ ,  $Z_{min}$  and  $Z_{ave}$  are maximum, minimum and average values of the mass flux, respectively. The benefit of this indicator is its scalability due to being defined based on fluxes. However, the downside is again that it ignores the effects of sectors with intermediate flux. Furthermore, another method was suggested by Chen et al. (1993). In their study, a normalized standard deviation ( $\sigma$ ) was used to describe the symmetry of the spray circumferential liquid distribution. Note that  $\sigma$  varies significantly with respect to the number of sectors employed, thus having less sectors yields a more inaccurate result. It is calculated from:

$$\sigma = \left[ \frac{\sum_{j=1}^N (y_j - \bar{y})^2}{N} \right]^{0.5}, \quad (19)$$

where  $N$  = number of sectors in the patternator,  $y_j$  = normalized height of liquid level in sector  $j$ , and  $\bar{y}$  = average value of  $y_j$ .

Using a set of these as indicators, it is possible to compare the effect that different variables have on the spray symmetry. For example, Tate (1960) identified several potential contributors to spray maldistribution some of which were associated with the used collection device and sampling technique such as splashing of the collected liquid in the vessels, and poor nozzle-to-patternator alignment in terms of the eccentricity or the angle. Other suggested sources of asymmetry were associated with nozzle design and flow conditions such as eccentricity of the swirl chamber and outlet orifice, manufacturing quality, liquid viscosity, and whether the flow was fully developed or not.

Some studies have examined the relationship between nozzle geometry and symmetry of the spray mass flux to determine how certain geometrical parameters affect the nozzle performance. This knowledge is the basis for nozzle design improvements, since the nozzle geometry can be tailored to the needs of the application. For example, Khavkin (2004) found that spray symmetry was dependent on several nozzle design parameters. These included asymmetries in the atomizer construction, number and size of the inlet ports, the swirl chamber length-to-diameter ratio ( $l_s/d_s$ ), the degree of atomizer openings ( $d_p/d_o$ ), and the swirl chamber-to-exit orifice eccentricity ( $\varepsilon$ ), which can be explained as the distance between the centers. For example, according to Borodin et al. (1976 cited in Khavkin 2004, p. 138), the effect of increasing  $\varepsilon$  is to reduce spray symmetry. They suggested that if eccentricity-to-orifice radius ratio ( $\frac{2\varepsilon}{r_o}$ ) was  $\leq 0.05$ , the effect of eccentricity would be negligible. All of these variables contribute to the non-uniformity in the thickness of the liquid film at the exit orifice, thus increasing the asymmetry of the liquid distribution (Khavkin 2004).

Similar research was conducted by Chen et al. (1993), who studied the factors that affected circumferential liquid distribution for a pressure swirl atomizer by using a cylindrical vessel with 16 sectors. The test liquid was water. They conducted the measurements for five different simplex nozzles with different discharge orifice length-to-diameter ratios ( $\frac{l_o}{d_o}$ ) ranging from 0.5 to 4.0, and varying injection pressures ranging from 0.34 to 1.72 MPa. They observed that increasing injection pressure produced a more symmetrical spray for the studied simplex atomizers regardless of  $\frac{l_o}{d_o}$  as shown in Fig. 13.

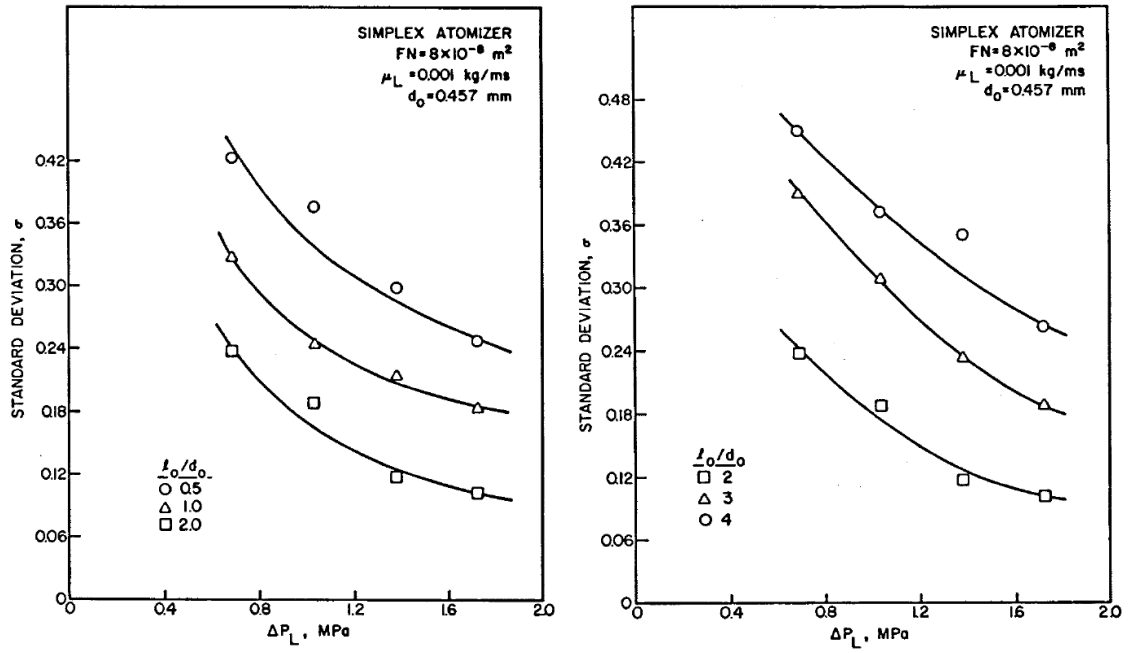


Figure 13. Effect of  $l_o/d_o$  on circumferential symmetry in the range of 0.5 – 4.0 with varying injection pressure (Chen et al. 1993).

In their study (Chen et al. 1993), one of the key geometrical features they studied was the exit orifice length-to-diameter ratio ( $l_o/d_o$ ). It was found that increasing the exit orifice length-to-diameter ratio improved patterning initially until an optimal value was reached. The optimal value for  $l_o/d_o$  was 2.0 at liquid viscosities of 1 – 6 mPas. Beyond the optimum, further increase had an adverse effect on the circumferential symmetry. However, they also observed that increasing the viscosity to 12 mPas produced a reduction of the optimal ratio. This seems to indicate that a wider exit orifice is beneficial for spray symmetry, when the liquid viscosity is increased. These findings are illustrated in Fig. 14.

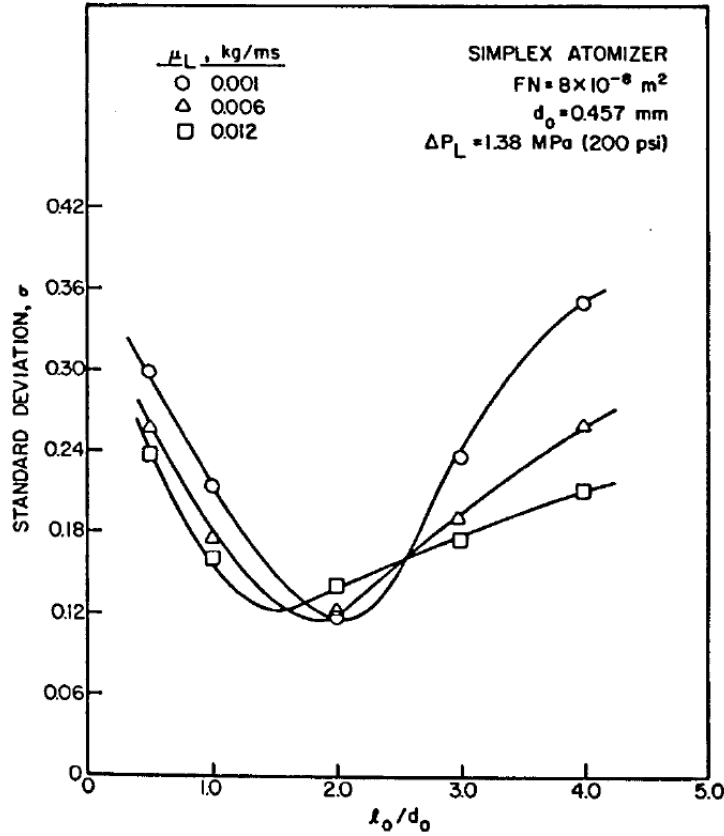


Figure 14. Effect of  $l_o/d_o$  and liquid viscosity on circumferential patterning with injection pressure of 1.38 Mpa (Chen et al 1993).

Furthermore, to study the effect of the number of feed slots, Chen et al. (1993) built two additional simplex atomizers that had similar flow numbers, but only one or two feed slots instead of the typical three-slot configuration. The single feed slot nozzle produced a much poorer uniformity in comparison to the nozzles with two or three feed slots (see Fig. 15). This result was validated by Khavkin (2004), who also observed a sharp reduction in spray uniformity, while using one feed slot instead of two or more. He suggested that, in comparison to the other geometrical parameters, this has by far the largest effect on spray symmetry. However, it is also worth noting that the addition of more than three feed slots yielded diminishing returns (Khavkin 2004).

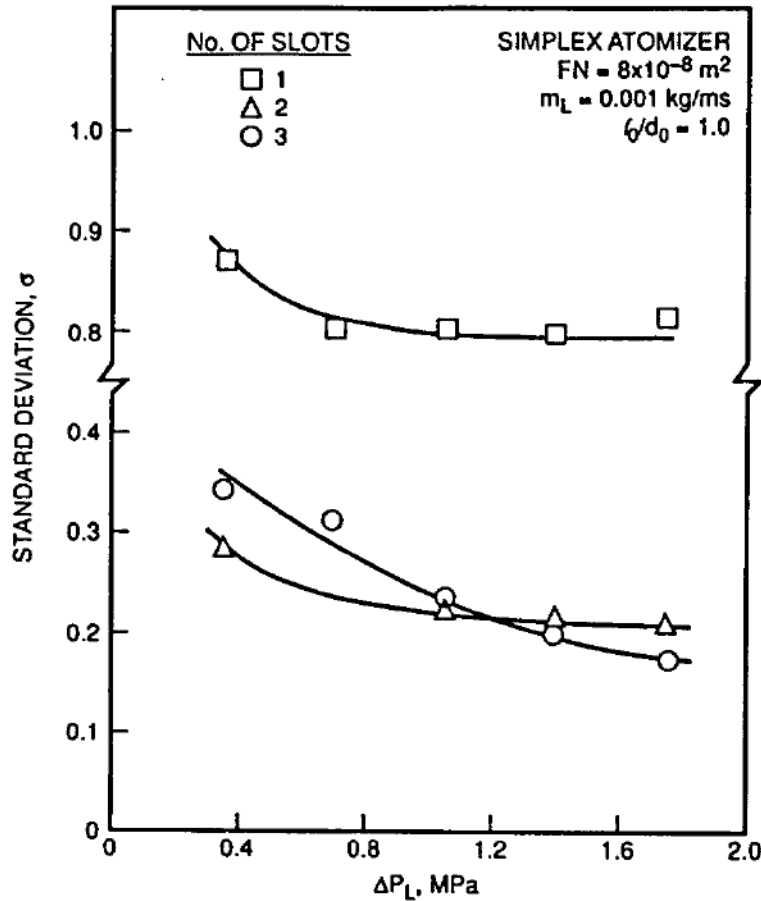


Figure 15. Effect of the feed slot number and injection pressure on circumferential patternation (Chen et al. 1993).

Furthermore, the spray uniformity may be decreased due to the presence of geometrical imperfections, which could be generated during the manufacturing process. Khavkin (2004) noted that the effects of these defects are worse for non-film forming sprays, and thus increasing the injection pressure in the presence of defect can actually decrease the patternation quality significantly. To ensure good patternation, additional grinding and polishing of the nozzle surfaces can be employed to improve the surface finish. It was also noted that the influence of manufacturing quality is especially influential at the exit edge of the nozzle. (Khavkin 2004.) Similarly, Rosfjord and Russel (1987) found that 0.2 mm impressions located at the exit orifice produced noticeable degradation in the fuel pattern, whereas v-shaped notches had less influence. Furthermore, they suggested the use of a square-shaped filming lip, since it enhanced circumferential uniformity in comparison to the sharp-edged filming lip designs.

Ortman and Lefebvre (1985) studied the radial and circumferential distribution of four different Simplex pressure-swirl atomizers inside a pressure vessel. Their study considered the effect of ambient pressure and injection pressure, which were both varied in the range 0.1 – 2.0 MPa. They found that the best nozzles produced excellent radial symmetry and exhibited circumferential maldistribution of less than 10%. As for the other nozzles, the results indicated apparent radial and circumferential maldistributions (see Fig. 16), which were also observed at different injection pressures and ambient pressures. Thus, they suggested that even though a nozzle produces satisfactory symmetry at one pressure level, it might not do so at another.



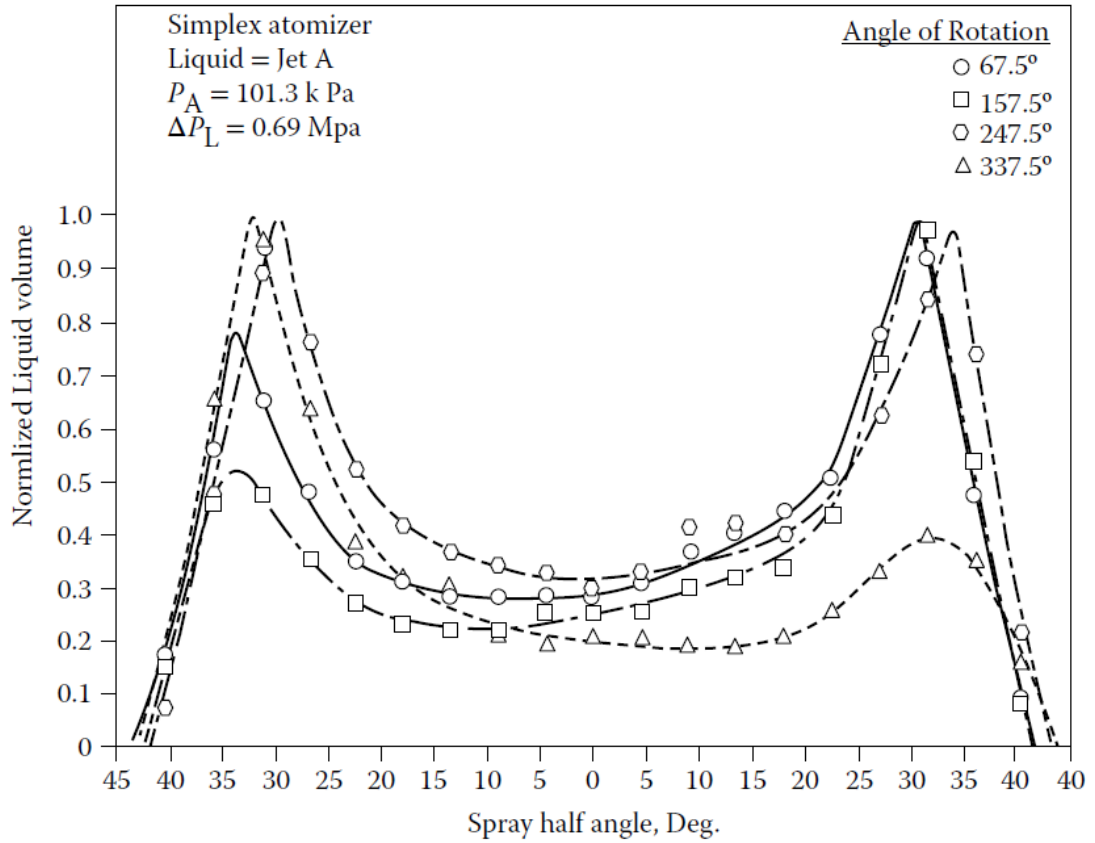


Figure 16. Radial liquid distribution at different angles to show circumferential uniformity (from Ortman & Lefebvre 1985 in Lefebvre & Vincent 2017).

Chen et al. (1993) also looked at the effect of viscosity on the spray symmetry. They found that increasing the liquid viscosity produced improved uniformity, although to a lesser extent than injection pressure. The mechanism for this improvement is unclear. In fact, higher viscosity reduces the Reynolds number. Contrary to observation, this should produce a reduction in the patterning quality. They suggested that the viscosity effect could probably be attributed to the increased thickness of the liquid film. This is because thicker films are typically more symmetrical and less sensitive to the imperfections on the surfaces of the nozzle exit. (Chen et al. 1993.)

The circumferential liquid distribution can also be affected by external effects such as airflows. This is relevant especially for nozzle-designs that utilize airflow in their operation such as aerating nozzles. This was demonstrated by Cohen and Rosfjord (1991), who measured the spatial distribution of several gas turbine fuel injectors using a rake-type patternator at high pressure and temperature. In their study, the nozzle was nested inside an air-swirler to produce a system that resembles a gas turbine. This is because gas turbines are typically operated with an anti-carbon-deposit airflow.

They varied different parameters, such as ambient gas pressure, temperature and density, airflow velocity, and liquid flowrate to investigate the effects on spray symmetry. They found that, in comparison to the other parameters, the airflow was the dominant factor in determining the spray pattern. In fact, the airflow caused the spray cone to collapse into several undesirable fuel rich regions, which explained the very high smoke numbers associated with the injector type. The usage of different liquids had no significant effects in comparison. (Cohen & Rosfjord 1991.)

### 3 Experimental

The experiments were conducted within a 1 m<sup>3</sup> plastic container, where the nozzle was placed in the center of the roof. The water-glycerol mixture was circulated through the nozzle with a pump, which was driven by an electric motor. The system was fitted with sensors to measure the mass flow rate, pressure, temperature and liquid density during the experiments. It was important to track these variables due to their potential effect on the liquid properties. These readings were relayed to the computer and recorded with Labview. The measured mass flow rate was converted to volume flow rate reading, which was used to adjust the pumping power to have a flow rate of 2 – 3 l/s. The closed-loop system is shown in Fig. 17.

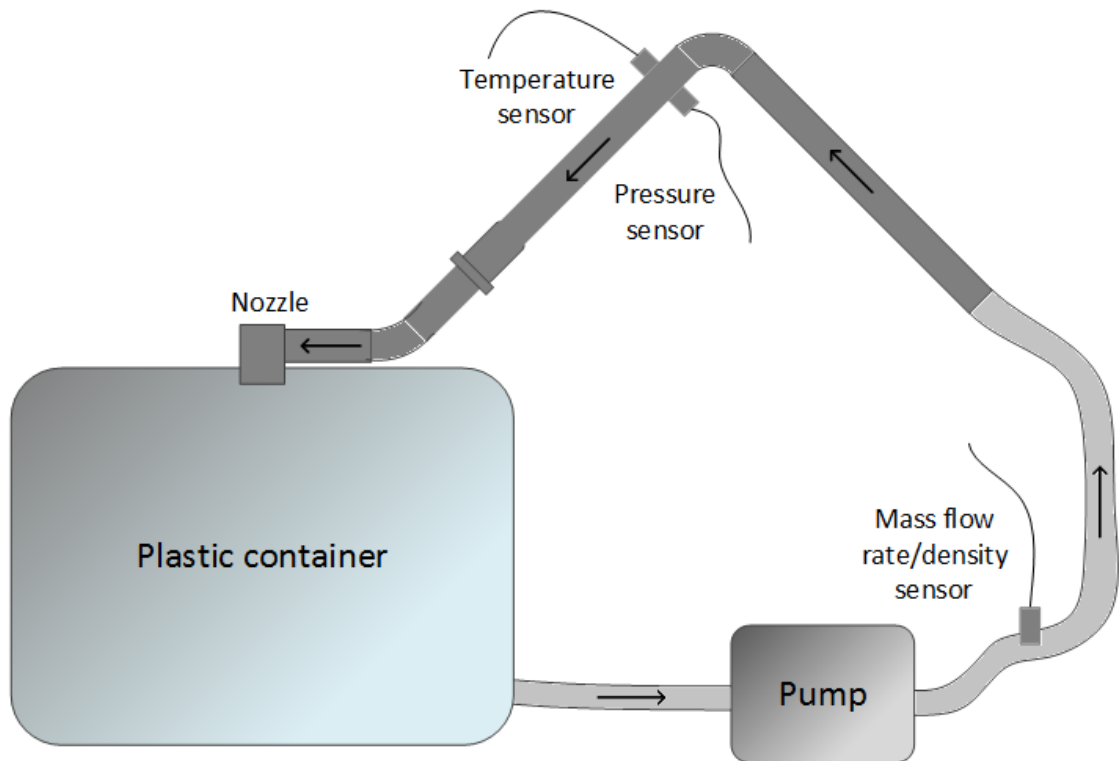


Figure 17. The closed-loop system for the spraying experiments.

#### 3.1 Pressure-drop measurement

The pressure data produced by the sensor had to be corrected due to the sensors location upstream of the nozzle. It was decided that the pressure-drop across the nozzle should be defined in terms of the nozzle attachment point, since this would allow comparison between other nozzles. Furthermore, the calculation of these quantities required information on the liquid properties such as viscosity and density, which were obtained from the viscometer and mass flow sensor, respectively.

The pressure sensor was located 0.675 m upstream from the expanding portion of the nozzle, as is shown in Fig. 18. To obtain the pressure drop across the nozzle, one must account for the pressure losses in the pipe and the difference in height between the two points. The losses in the pipe leading to the nozzle inlet occur due to flow friction in the straight part and the abrupt tapering of the pipe diameter from 38.0 mm to 27.2 mm at

the nozzle attachment point. The tapered pipe is considered a part of the nozzle, since it is manufactured in one piece. Other relevant dimensions are given in Fig. 19.

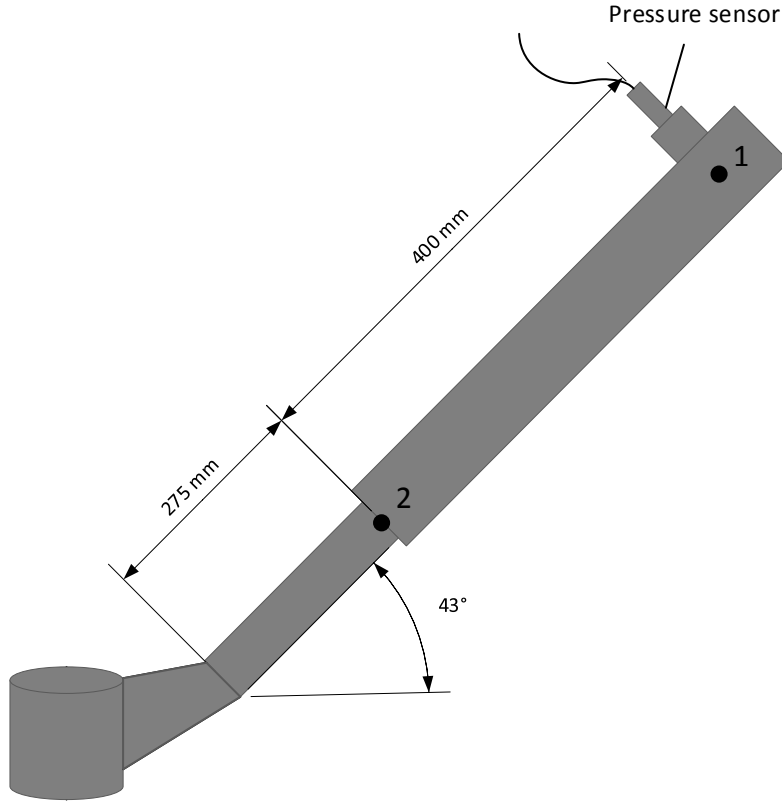


Figure 18. The piping between the pressure sensor and the nozzle.

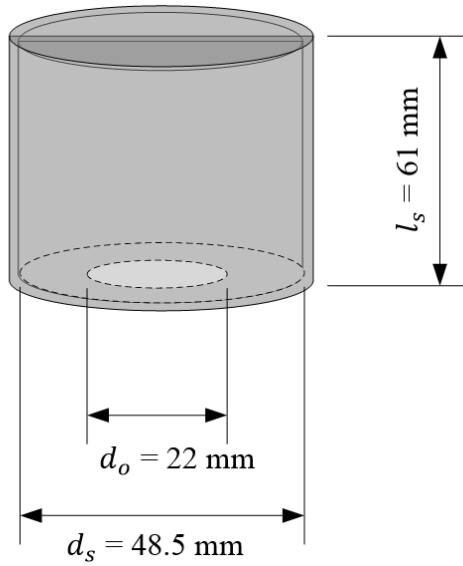


Figure 19. Schematic of the swirl chamber and exit orifice dimensions.

Firstly, for the pipe flow, the pressure loss due to friction can be calculated from (Kast et al. 2016):

$$\Delta p = \xi \frac{l}{d_i} \frac{\rho_l \bar{v}^2}{2}, \quad (20)$$

where  $\Delta p$  = pressure drop,  $\xi$  = friction coefficient,  $d_i$  = inner diameter,  $l$  = pipe length,  $\rho_l$  = liquid density, and  $\bar{v}$  = average velocity.

In our case, the flow was found to be laminar in the inlet pipes, thus simplifying the evaluation of the pipe friction coefficient. For laminar pipe flows, the friction coefficient can be determined based on flow Reynolds number as:

$$\xi = \frac{64}{Re}. \quad (21)$$

Secondly, for the abrupt reduction in the pipe diameter, the pressure drop can be calculated from (Kast et al. 2016):

$$\Delta p = \xi_{in} \frac{\rho_l \bar{v}^2}{2}, \quad (22)$$

where  $\xi_{in}$  = friction coefficient for the abrupt reduction in pipe diameter, which can be read from Fig. 20.

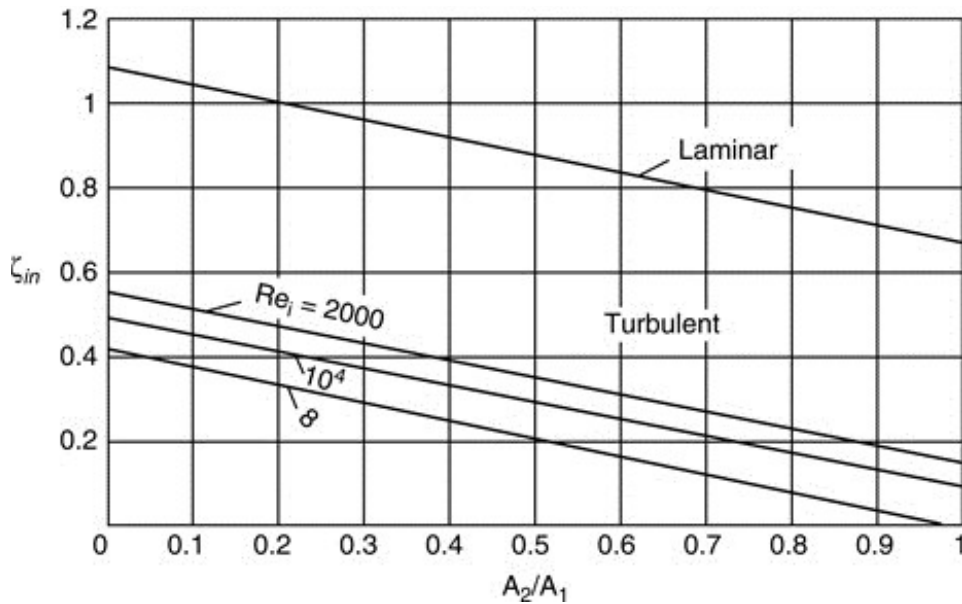


Figure 20. Friction coefficient of abrupt reduction in the pipe diameter ( $\xi_{in}$ ) as a function of the ratio of the pipe cross-section areas (Kast et al. 2016).

The combined pressure losses between the sensor and the nozzle inlet can now be calculated. We can use Bernoulli's equation to calculate the pressure at point 2 to obtain the pressure drop across the nozzle portion. However, Bernoulli's equation is defined for the inviscid flow, and thus it assumes conservation of energy and a flat velocity profile in the flow. These assumptions are untrue in viscous flow, where the velocity profile takes a parabolic shape due to flow friction, which also means that some of the energy is lost in the form of heat. Thus, the equation has to be modified to account for the effects of flow friction by adding in the term  $\Delta p_{pipe}$ , which accounts for the energy losses. This will yield an approximation for the pressure at the nozzle attachment point. Assuming the flow is steady and incompressible, the Bernoulli's equation can be written as (Shaughnessy et al. 2005):

$$\frac{p_1}{\rho} + \frac{1}{2} \bar{v}_1^2 + g z_1 = \frac{p_2}{\rho} + \frac{1}{2} \bar{v}_2^2 + g z_2 \quad (23)$$

After adding the correction term, we have:

$$\frac{p_1}{\rho} + \frac{1}{2} \bar{v}_1^2 + g z_1 - \frac{\Delta p_{pipe}}{\rho} = \frac{p_2}{\rho} + \frac{1}{2} \bar{v}_2^2 + g z_2. \quad (24)$$

Solving for  $p_2$ , we get:

$$p_2 = p_1 + \frac{\rho}{2} (\bar{v}_1^2 - \bar{v}_2^2) + \rho g (z_1 - z_2) - \Delta p_{pipe}, \quad (25)$$

Using equation (25), the pressure data from the sensor ( $p_1$ ) can be corrected such that it corresponds to the pressure drop across the nozzle.

### 3.2 Viscosity of the water-glycerol mixture

The ambient temperature in the measurement location varied in the range of 22 – 27 °C. The ambient temperature was not only affected by the outside temperature, but also to a large extent by the sunlight passing through the large windows. These changes in temperature influenced the liquid viscosity. It was found that the liquid viscosity was slightly different day-to-day and changed during the experiments. Therefore, it was important to evaluate the viscosity accurately.

Initially, the idea was to calculate the viscosity from the logger data (liquid temperature and density) using an empirical formula provided by Nian-Sheng (2008). This formula considered the liquid viscosity as a function of both temperature and glycerol concentration. The liquid temperature was obtained directly from the logger data, while the glycerol concentration was determined based on the total density of the liquid mixture and the calculated densities of the pure components. This formula is applicable to concentrations of 0 – 100% and temperatures of 0 – 100°C, and the error associated with it is less than 5% for 95% of the data found in three databases (Nian-Sheng 2008).

This yielded an evaluation of the liquid viscosity without having to measure the viscosity by sampling. However, it was observed that the measured liquid viscosity was different between the two methods, which meant that one of the methods had to be inaccurate. The discrepancy was attributed to the highly exponential relationship between the liquid viscosity and density at high glycerol-to-water ratios, which lead to disproportionately large deviations in the calculated viscosity even for very small changes or errors in measured density. Thus, to account for this discrepancy, a correction factor was formulated by comparing the calculated viscosity to the one indicated by the viscometer. However, the error in the calculated viscosity was estimated to be around  $\pm 19\%$  even with the density correction factor. Therefore, it became clear that the empirical formula could not be used to reliably estimate the viscosity at high glycerol concentration.

Potential sources of error that could contribute to such a large error include inaccuracies in density measurement, use of average values, and the notable effects of bubble formation. For example, average values were used for both the liquid temperature and density, since the changes in the respective values were roughly in the range of 0.5 – 1%. However, it is possible that even these minor changes could affect the end result due to the exponential nature of the viscosity curve. Furthermore, the empirical formula excluded any form of air-mixing from the analysis. This could affect the accuracy of the calculated viscosity value, since a significant amount air was absorbed into the mixture

in the form of air-bubbles. These bubbles were formed not only due to the impact between the spray and the liquid surface below, but possibly also due to air-to-liquid interactions that occurred within the nozzle or as the liquid sheet disintegrated. The formation of these air-bubbles could change the total density of the liquid mixture even with very low air concentrations due to the much lower density of air in comparison to both water and glycerol. Furthermore, it was also observed that the bubbles affected viscosity by increasing the amount of flow friction. These phenomena had an opposing effect on viscosity, which means that the viscosity change could be in either direction depending on the properties of the bubbles.

The increased viscosity can be explained by the much higher surface tension of the smaller bubbles, which makes them behave like particles in the flow. The presence of particles generally increases the flow friction. This effect may be different depending on the shape of the particles or bubbles. In comparison to particles, however, the effect of bubbles is more difficult to quantify due to the more complicated boundary conditions and the tendency of the bubbles to deform with the flow. If the entrained bubbles have a small diameter and the flow velocity is relatively low, the liquid surface tension is likely to keep the bubbles approximately spherical, which supports the analogy of bubbles as particles (Taylor 1932). In our case, there were two observations, which would support the assumption of spherical bubbles. Firstly, the flow was laminar at least in the pipe portion, and secondly, the shape of the bubbles was observed to be spherical in the emerging spray. However, this does not exclude the possibility of deformation of the bubbles inside the nozzle portion of the flow, especially at the exit orifice, where the flow reaches its maximum velocity.

Since the bubble formation prevented the use of the calculation method, the Brookfield (Model DV-II +) viscometer was chosen as the primary method of viscosity measurement. The device is based on the measurement of torque of a submerged spinning disk. According to the manual, the precision of the device is in the range of  $\pm 1$  % for any spindle/speed combination. The viscosity values given by our device were confirmed by a similar viscometer at the chemistry department. This ensured an accurate evaluation of the viscosity for each of the experiments with some additional work taking samples and measuring the viscosity.

The following procedure was used in measuring the viscosity for each of the samples. Before the experiment, the viscometer was auto-zeroed by removing the spindle and pressing any button. The spindle was then put back in its place and inserted into the sample at the correct height as determined by the small groove in the spindle. The next step was to set the spindle rotational speed according to the manual to ensure accurate viscosity reading. After a few minutes, the viscosity reading was recorded, and the sample was changed.

The change in viscosity during a measurement was studied by taking a set of four liquid samples at a five-minute interval. The samples were taken directly from the dribble at the nozzle exit each time the pump was turned off for a moment, thus ensuring that the sample represented the viscosity inside the nozzle. These samples were then measured with the viscometer. The results showed a clear trend of decreasing viscosity with increasing duration of circulating the liquid (see Table 1). This was attributed to the increasing temperature of the liquid. For 1 °C increase in temperature, the viscosity was reduced by 9.3 %. To avoid the heating effect, the pump was run only for small durations during the measurements. Thus, the bubble formation would have a more pronounced effect on the viscosity of the mixture in comparison to the change in liquid temperature.

*Table 1. Change in liquid viscosity and temperature for different durations of running the pump at 2.00 l/s.*

Sample	t [min]	$\mu_l$ [mPas]	$T_l$ [°C]
1	5	226,5	24,2
2	10	219,5	24,4
3	15	210,5	24,7
4	20	205,5	25,2

By observing the readings given by the viscometer, it became apparent that the bubbles can have a different effect based on their size. The larger bubbles reduced the viscosity, whereas the smaller bubbles increased it. This could be explained by the much stronger surface tension that characterizes the small bubbles, thus making them act as small particles in the flow. Furthermore, the large bubbles were typically only encountered in the beginning of the experiments and they seemed to have a very small lifespan. Thus, as the smaller bubbles were much more prevalent, the dominating effect of the bubbles was to increase the liquid viscosity.

### **3.3 Spray angle measurement**

In our measurements, we used Photron FASTCAM SA3 and FASTCAM SA-Z high-speed cameras, which recorded grayscale and color video, respectively. These cameras were set in a perpendicular arrangement to get a simultaneous front and side view of the spray. The alignment of the camera was set with the aid of a leveling device such that it was tilted less than 1° in any direction. Furthermore, the camera legs were adjusted to the appropriate height to obtain a good view of the emerging spray. The distance between the camera and the nozzle was adjusted to correspond with an image scale of about 40 cm. The cameras were connected to Photron FASTCAM Viewer (PFV), which was the software used to record the measurements.

The lighting of the spray involved two LED-lamps, which were set above the nozzle to illuminate the near-nozzle region. The lamps were oriented downwards in a steep angle on opposite sides of the nozzle. Both the roof and the walls of the container were covered with an opaque material, thus creating good contrast between the emerging spray and the background. This lighting setup was found best after trial and error, as it produced video footage that was easy to process in Matlab. Fig. 21 shows a schematic of the measurement setup.

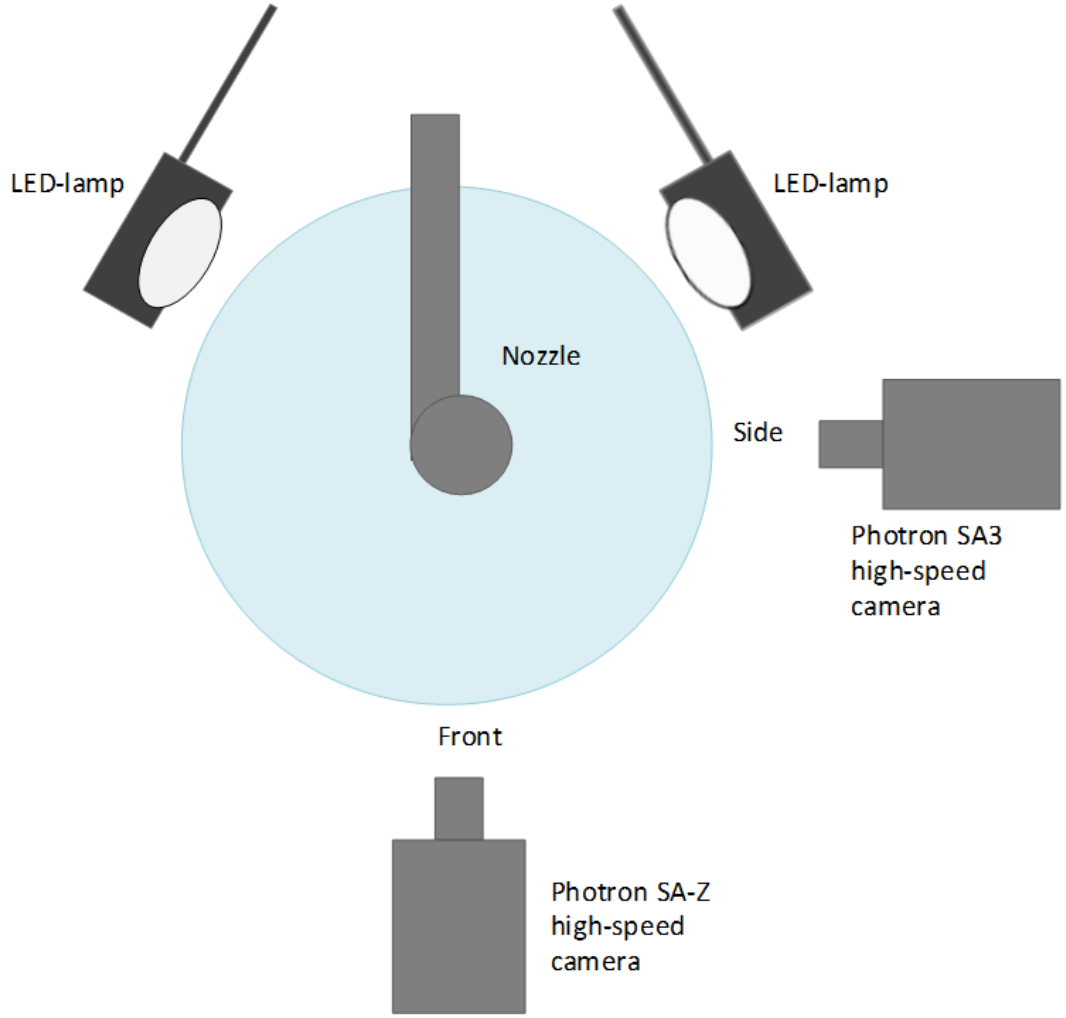


*Figure 21. Setup for the high-speed camera measurements.*

Frame rate and shutter speed are key parameters in high-speed photography. Frame rate refers to the amount of frames per second, thus being a measure of temporal resolution, whereas shutter speed determines the length of time the camera sensor is exposed to the object. This affects the camera's ability to capture the motion of the object: increased shutter speed corresponds to a shorter exposure time, which reduces the motion blur of objects moving at high velocity. (Versluis 2013.)

According to Versluis (2013), two cases must be considered, when choosing the frame rate. Firstly, if the frequency of an event is known, the Nyquist sampling theorem can be used to determine the sampling rate. The theorem states that the sampling rate should be at least twice the event frequency, but preferably higher. Conversely, if the relevant time scale is difficult to estimate, the following formula can be used to estimate the optimum frame rate (Versluis 2013):

$$f = \frac{N_s u}{l}, \quad (26)$$

where  $N_s$  = number of required samples,  $u$  = typical velocity (m/s), and  $l$  = typical length scale (m).



Firstly, based on Nyquist theorem,  $N_s$  of 2 or more is necessary. As for the velocity term, it was obtained from the measured film velocity, which was 14 m/s at maximum. Lastly, the length scale of interest was estimated to be 0.05 m. This is based on wanting to detect the same bubble at least 4 times across 20 cm distance, which is a rough estimate of liquid film break-up length. Using these values in equation (26), the minimum sampling frequency was estimated to be 560 fps. We used the sampling frequency of 2000 fps, which fulfills this criteria. This frame rate also allowed the use of the 1024-to-1024 resolution setting, which was preferable in comparison to the lower resolutions accompanied by further increase in frame rate.

Motion blur can be minimized by choosing short enough exposure time. The exposure time of 0.1 ms was chosen based on visual observation. However, having a very short exposure time reduced the amount of light passing to the camera sensor. Thus, the increased shutter speed had to be compensated by increasing the illumination level. In our case, the use of such a short exposure time was permitted by the two LED-lamps.

Spray angle data was obtained from the recorded videos with a specifically designed Matlab code, which is shown in Appendix 1. A video consists of a set of subsequent images or frames, which are ordered with respect to time. To begin the analysis, Matlab reads the individual frames of the video-file and sets them into a data structure. Each of the frames is then subjected to image analysis, where the contrast is improved and the image is converted into a binary image. The binarized image is improved further by filtering out smaller areas according to the amount of connected pixels. This operation removes pixel chunks that have less pixels than a set limit value, thus eliminating any areas that are disconnected from the main shape.

In Matlab, an image is represented as a matrix, where one cell corresponds to a pixel in the image. These cells are assigned a value, which reflects the intensity of that pixel. Typically, for a grayscale image, the intensity is in the range from 0 to 255, where the limit values correspond to black and white, respectively. RGB-color images, however, are constructed from a set of three matrices, which represents the red, green and blue channels. These channels contain the intensity map for each of the three colors. All the other colors can be created as a combination of the three primary colors.

The grayscale image enhancement involved histogram equalization, which spreads out the most frequent intensity values across a wider intensity range, thus improving the contrast of the image. The improved contrast is useful for the subsequent binarization, since the difference between light and dark areas becomes more distinct. In a binary image, a pixel is represented either as a 0 or a 1, as opposed to a grayscale image, in which a pixel can have a range of different values. The intensity range of a grayscale image can be converted into binary form by setting a threshold value, which determines whether a pixel is assigned the value of 0 or 1. To use this method on a color image, it has to be first converted into a grayscale image prior to binarization. This procedure is shown in Fig. 22. The same process applies to grayscale images without the grayscale conversion step.

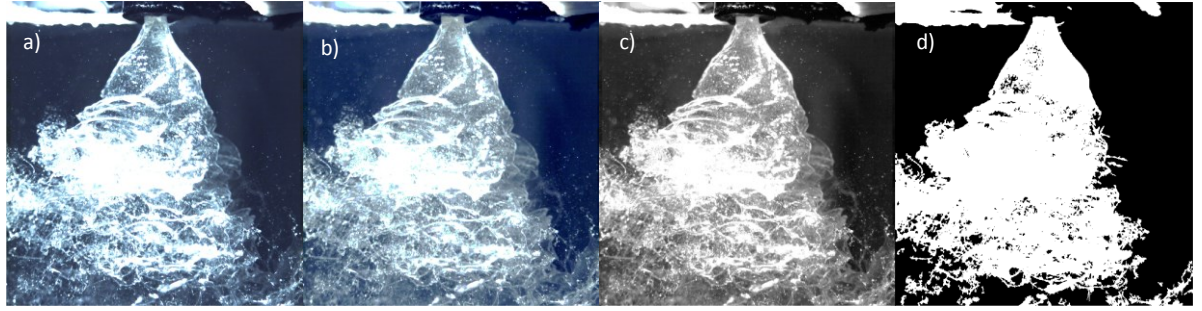


*Figure 22. Steps involved in enhancing a color image. Here a) is the original image, b) shows the effect of contrast improvement, c) is the grayscale conversion, and finally, d) is the filtered binary image.*

The used Matlab code involves three steps. Firstly, the user runs a section of code, which shows a single frame without any enhancement. This frame is used to manually determine the two edge-points of the nozzle exit orifice, which remain constant for the whole length of the video. These points are then inserted into the code, and the rest of the code is run to find the edges of the spray at a specified pixel distance for a large set of frames. If necessary, the binarization threshold is adjusted appropriately to ensure good visibility of the spray edge.

After specifying the measurement cross-section, Matlab examines pixel values starting from the edges, and proceeding towards the center. When Matlab encounters a pixel value of 1, it sets that pixel as the edge point for the respective side. The points at the edges and at the nozzle entrance define two triangles, which are used to determine the visual spray angle both on the left- and the right-hand side. As explained previously, summing the half-angles then yields the total spray angle. Furthermore, by knowing the difference between the two sides, we have a measure of how much the flow seems to lean to one side or the other. This can be represented by calculating the angle between the spray center line and the nozzle axis, as was shown in Fig. 3.

### **3.4 Liquid film velocity from bubble tracking**

The liquid film emerged from the nozzle with a certain velocity, which was evaluated by tracking bubbles entrained in the flow. In our case, the flow had a lot of visible bubbles due to the high viscosity of the mixture. These bubbles were tracked using ImageJ Fiji, which is an open-source image analysis software (Schneider et al. 2012). The automated tracking was based on the Trackmate plug-in (Tinevez et al. 2017).

The bubble tracking became more difficult with increasing flow velocities, as this tended to intensify the effect of lighting, thus causing overexposure. This reduced the bubble visibility in certain parts of the spray. However, the bubble velocities were still obtainable by having a large quantity of frames and proper filtering. The mean velocities of the tracked bubbles varied slightly across the chosen tracking area. The differences in mean velocity can probably be attributed to the velocity distribution within the liquid film, since the velocity of a bubble is dependent on its location in the liquid film. Furthermore, it is possible that the actual velocity of the film may vary depending on the location at the exit, since there can be non-uniformities in the thickness of the liquid film.

First step in the bubble velocity measurement was setting the scale. The scale was determined based on the measured length of a ruler, which corresponded to a certain amount of pixels in the image. This yielded an estimation for the measured lengths as millimeters per pixel. To start the analysis, the Trackmate-plugin was opened, the correct parameters were set, and the automated tracking was then used to detect the velocities of the visible

bubbles in the spray. The resulting tracks had to be filtered to exclude misinterpreted bubble trajectories or floating droplets. These types of tracks were recognized based on having an unexpected direction or velocity in comparison to the liquid film. Fig. 23 shows an example of the bubble detection for a single frame.

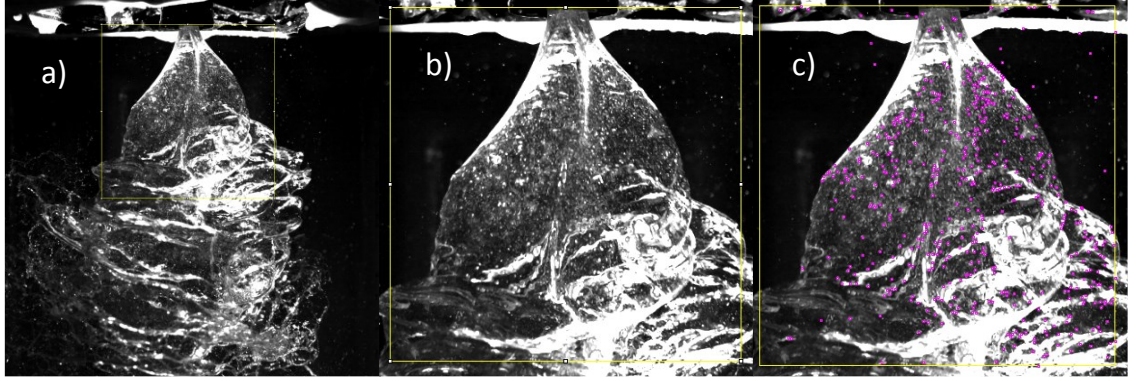


Figure 23. a) Full size image, b) close-up of the detection area, and c) detected shapes in a single frame.

To reduce the false tracking, the search parameters such as particle diameter and quality threshold were set to appropriate values via trial and error. This ensured that the tracking algorithm found enough high-quality shapes to produce multiple tracks, which were linear and in the right direction. It is also possible to have too many particles near one another, which causes the algorithm to detect wrong particles that are in the near vicinity of the correct one. This may introduce some slight error into the measurement. To avoid this the search radius parameter can be set very small, while having an adequate amount of tracked particles. However, some false trajectories are bound to occur even with the proper parameters. These are then subjected to filtering, thus leaving only high-quality tracks to be analyzed. The average velocity of these tracks yielded an estimate for the average velocity of the liquid sheet. This information could then be used to evaluate the average film thickness and the average air-core size. Consider the average effective exit area ( $\bar{A}_{eff}$ ), which can be defined based on the average velocity as:

$$\bar{A}_{eff} = \frac{\dot{V}}{\bar{v}_f}, \quad (27)$$

where  $\bar{v}_f$  = average film velocity, and  $\dot{V}$  = flow rate.

Since we know the exit orifice area ( $A_o$ ), the average air-core area can then be calculated as follows:

$$\bar{A}_a = A_o - \bar{A}_{eff}. \quad (28)$$

Combining equations (27) and (28), we get:

$$\frac{\bar{A}_a}{A_o} = 1 - \frac{\dot{V}}{A_o \bar{v}_f}, \quad (29)$$

which describes the average air-core area in dimensionless form as a fraction of the exit orifice area.

Furthermore, from equation (28), we can get the average air-core radius:

$$\pi \bar{r}_a^2 = \pi r_o^2 - \frac{\dot{V}}{\bar{v}_f},$$

which becomes:

$$\bar{r}_a = \sqrt{r_o^2 - \frac{\dot{V}}{\bar{v}_f \pi}}. \quad (30)$$

Secondly, using equation (28), we can calculate the average film thickness ( $\bar{t}$ ) starting from:

$$\bar{A}_{eff} = A_o - \bar{A}_a.$$

Opening up the terms, we get:

$$\frac{\dot{V}}{\bar{v}_f} = \pi(r_o^2 - \bar{r}_a^2) \quad (31)$$

This can be expanded to:

$$(r_o - \bar{r}_a)(r_o + \bar{r}_a) = \frac{\dot{V}}{\bar{v}_f \pi}, \quad (32)$$

where the term  $r_o - \bar{r}_a$  is equal to  $\bar{t}$ .

Moving the terms around, we get the form:

$$\bar{t} = \frac{\dot{V}}{\bar{v}_f \pi (r_o + \bar{r}_a)}. \quad (33)$$

Now, inserting equation (30) into (33), we have:

$$\bar{t} = \frac{\dot{V}}{\bar{v}_f \pi \left( r_o + \sqrt{r_o^2 - \frac{\dot{V}}{\bar{v}_f \pi}} \right)}. \quad (34)$$

### 3.5 Spray pattern measurement

Our patternator design resembles the radial patternator employed by McVey et al. (1986). We decided to use a similar flat array formation with squared entrances, while having triangular collecting vessels. The triangular vessels have a higher capacity in comparison to similar height rectangular vessels, thus allowing us to keep the height of the patternator under 30 cm. This ensured a sufficient sampling time regardless of the limited space.

The design included a sampling gate, which was operated with a manual lever. The main purpose of the sampling gate was to stop any flow from entering the collecting vessels at the incorrect flow rate such as when the flow was in transient phase or dribbling from the nozzle after the pump was turned off. This ensured that the liquid was collected for the correct sampling duration and only at the correct flow rate. The patternator design is shown in Fig. 24.

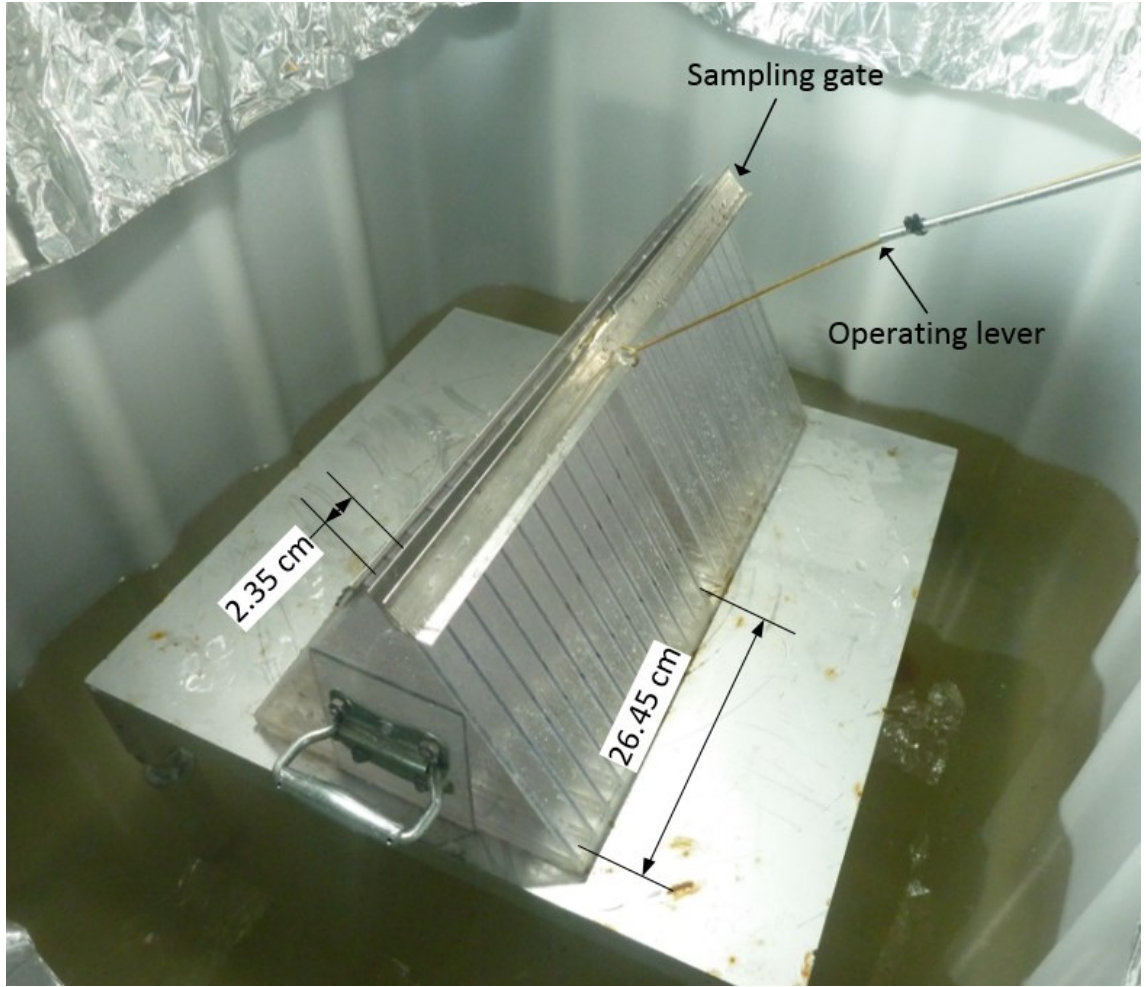


*Figure 24. The radial patternator design employed in the measurement of liquid distribution.*

In our case, the patternator was built from 3 mm thick translucent plastic, thus allowing data to be gathered by observing the heights of the liquid columns in each of the probes. The thicker plastic was used to ensure robustness of the structure. The two-winged patternator was mounted onto a square platform, where it could be turned in  $45^\circ$  increments. This was achieved by having one central hole in the middle and multiple smaller holes in a circular formation, where the patternator was then held in place by two pins. To rotate the patternator, it was lifted up by the handles and the outer pin was placed into a different hole. The patternator position was described by the patternator angle ( $\phi$ ), which is defined in terms of the left-hand side of the patternator. To obtain data on 8 sectors, we used angular positions of  $0^\circ$ ,  $45^\circ$ ,  $90^\circ$  and  $135^\circ$  for the patternator. These angles describe how much the patternator was rotated from the default position (the left-hand side at  $0^\circ$ ). This coordinate system is shown in Fig. 25.



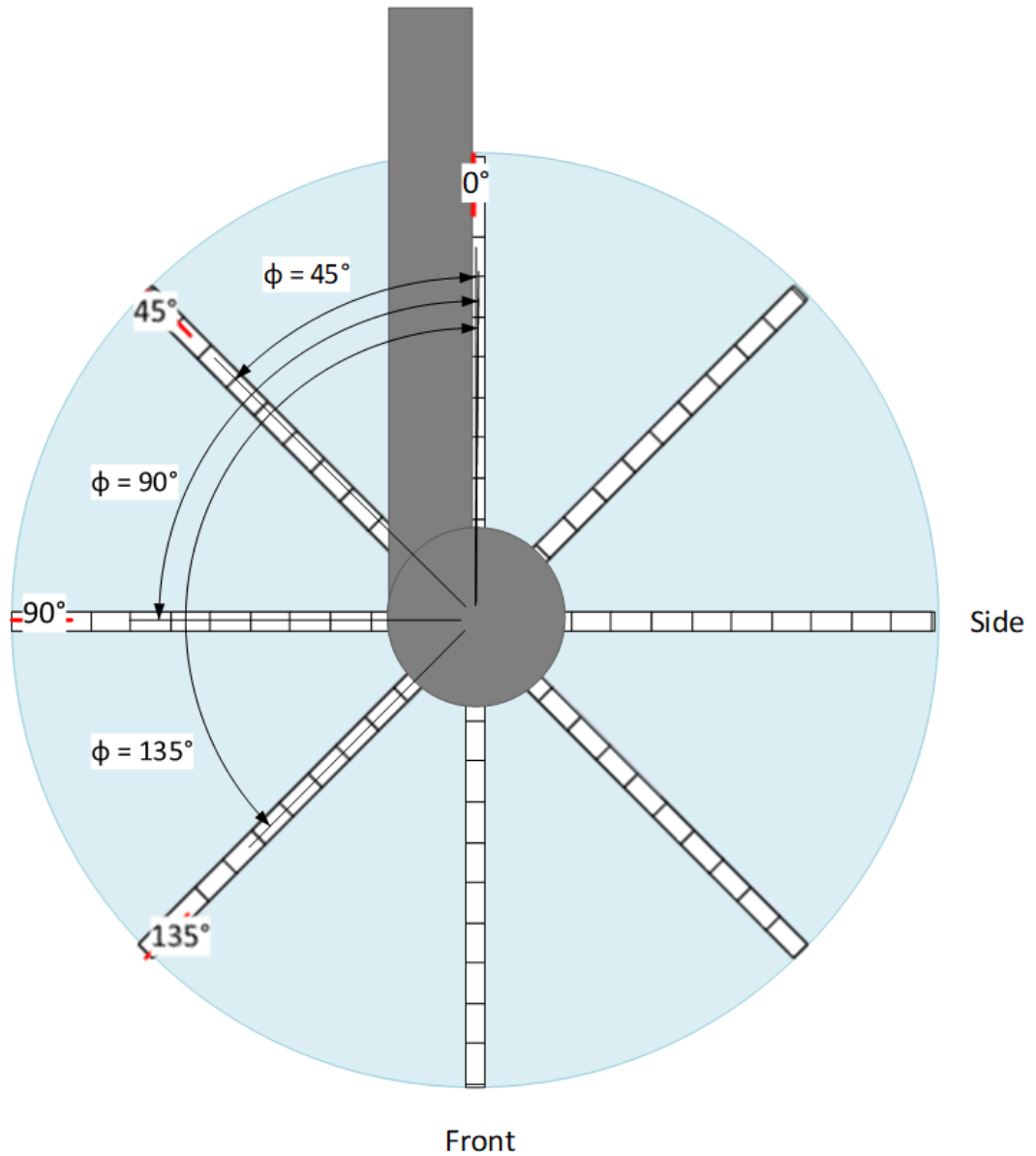


Figure 25. Patternation measurement setup and the definition of the patternator angle ( $\phi$ ).

In our design, the probe entrances were 1 cm wide and 2 cm long, thus yielding a far coarser resolution than the typical 0.5 cm probe spacing. Another important difference in comparison to previous studies was that we decided to place the patternator at a 28 cm distance away from the nozzle instead of the typical 10 cm or less. These decisions were based on the much larger size and flow rate of the measured nozzle. Bringing the patternator very close to the nozzle would have required a smaller probe spacing, thus complicating the patternator design in two major ways. Firstly, the probes would have filled up in a very short duration without an external collection system, and secondly, it is not obvious if the high-viscosity liquid would flow properly through such narrow passages without spilling.

The first step was to ensure everything was set correctly before the start of the measurement. Firstly, this involved checking the angular alignments of the patternator table

and the nozzle. Secondly, the patternator was centered carefully with respect to the exit orifice by using a string with a weight at the other end. When all of these aspects were in good condition, the data logger was started, sampling gate was closed, and the pump was turned on to initiate the liquid flow.

The first measurement was conducted after the flow reached the desired volume flow rate of 2, 2.5 or 3 l/s. The sampling gate was opened with the operating lever, while simultaneously starting the timer. The measurement duration was determined according to how fast the sampling vessels filled up. When any of the sampling vessels got too close to being full, the sampling gate was closed and the timer was stopped. Typically, this produced a sampling time of 33 – 62 s. After collecting the sample, the pump was turned off and the patternator was lifted to a stand, where the liquid levels were recorded with a camera. Fig. 26 shows an example image.



*Figure 26. Photo of the radial liquid distribution collected by the patternator with enhanced contrast and gamma.*

These images were brought into ImageJ, where the scale was set according to the ruler resting on the side of the patternator. This allowed the pixel lengths to be represented in terms of millimeters. These lengths were read from the images with ImageJ “measure” tool, and then collected into an excel-file for further analysis.

The liquid volume takes the form of an isosceles trapezoid due to the triangular shape of the collecting vessel. Thus, the length of the side of the trapezoid could be determined based on the distance from the bottom to the edges formed onto the walls of the vessels. These edges were more or less visible depending on lighting, image formatting, and amount of foam formation. For example, direct sunlight decreased visibility for some of the edges, and thus the experiments were conducted later in the day to avoid this issue. Conversely, formation of foam made it much easier to detect the edge, which meant that images taken later in the measurement set were usually slightly easier to analyze. Furthermore, reading the lengths could be made easier by changing the contrast and gamma setting in ImageJ.

To obtain the flowrate for each of the probes, the calculated liquid volumes are divided by the duration of the measurement. The flowrates of individual probes are modified to

correspond to a sector shape by multiplying them with an area weighing factors shown in Fig. 27. For our case, the area correction factor was defined based on the midpoint of the patternator wing. Thus, for the patternator with 11 probes per wing, the sector and probe widths were equal at the middle of the sixth probe. Thus, the flow rate of a probe can be expressed a

$$\dot{V}_i = C_i \frac{V_i}{t}, \quad (35)$$

where  $C_i$  = area correction factor,  $V_i$  = collected volume in probe i, and  $t$  = duration of the measurement.

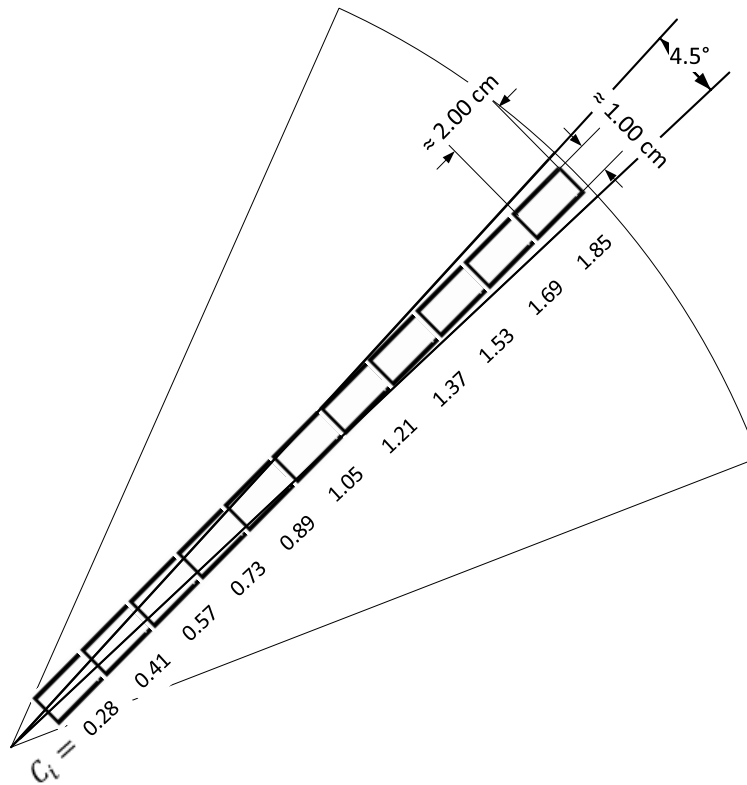


Figure 27. Area correction factors for each probe radiating from the center of the patternator.

## 4 Results and discussion

### 4.1 General flow characteristics

To evaluate whether the flow was laminar or turbulent, the Reynolds number for the pipe flow was calculated at varying flow rates and viscosities for different pipe cross-sections. These cross-sections included the larger pipe upstream, the pipe after the tapering, and the nozzle inlet with diameters of 38.0 mm, 27.2 mm, and hydraulic diameter of 39.1 mm, respectively. The nozzle inlet was calculated based on hydraulic diameter due to its rectangular shape. The calculated Reynolds numbers are shown in Fig. 28, which clearly shows that the flow was in laminar range ( $Re < 2300$ ) both in the pipes and at the nozzle inlet for the whole flow rate range of 2 – 3 l/s. The highest  $Re$  is just over 1000. Furthermore, it can be seen that the slopes are largest for the pipe with the smallest diameter of



27.2 mm. This is expected, since the average velocity is higher within the smaller pipe. The average velocity is calculated by dividing the flow rate with the cross-sectional area.

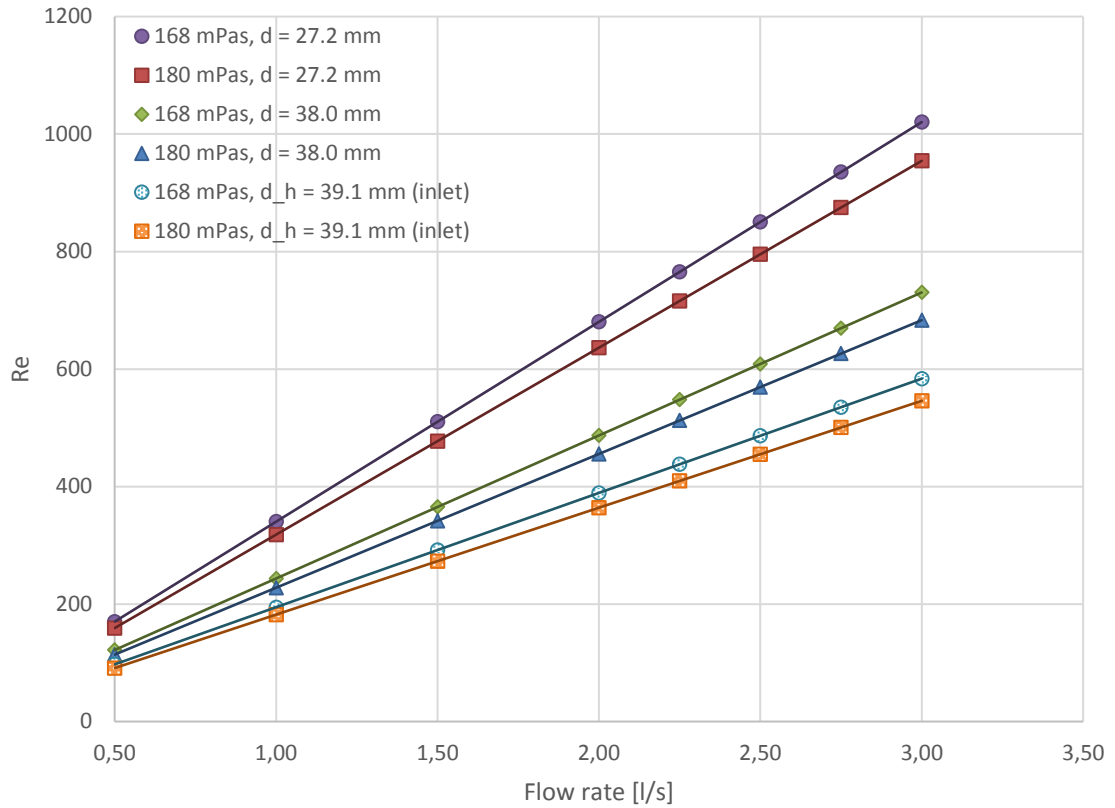


Figure 28. Reynolds number as a function of flow rate and viscosity in the pipes and at the inlet.

The calculated Reynolds numbers were used to evaluate the friction factors for the pipe flow. This allowed the calculation of the pressure losses in the pipe between the pressure sensor and the nozzle attachment, which accounted for 8 – 19 % of the total pressure-drop. The lower percentage corresponds to the higher flow rate, since the magnitude of pressure loss in the nozzle grows disproportionately in comparison to the pressure loss in the pipe leading to the nozzle attachment. Furthermore, it is sometimes interesting to relate spray characteristics to the inlet Reynolds number – for example how does the stability of the air-core change as a function of inlet  $Re$ .

Due to the upstream location of the sensor, it was necessary to use a modified Bernoulli equation to obtain the pressure at the nozzle attachment point. This accounted for the small height difference, the tapering of the pipe, and the pressure drop before the nozzle attachment. After filtering the data to only include data points with steady flow, it was possible to draw the pressure drop curves in Fig. 29. Clearly, the figure shows how increasing the viscosity from 168 to 180 mPas (roughly 7 % increase) produces a negligible difference in pressure drop. The nozzle pressure-drop was between 0.35 – 0.96 bar for flow rates of 2 – 3 l/s at both viscosity levels.

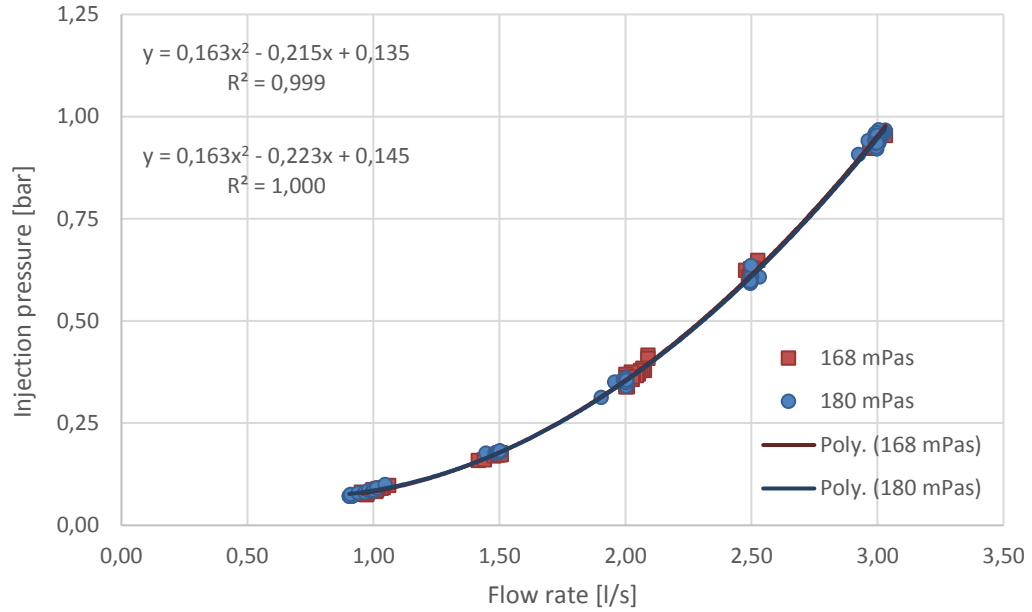


Figure 29. Injection pressure as a function of flow rate at viscosities of 168 and 180 mPas.

The collected pressure-drop data was used to calculate both flow number ( $FN$ ) and discharge coefficient ( $C_d$ ). Looking at Fig. 30 and 31, it can be seen that  $FN$  and  $C_d$  have a reducing trend, which can be attributed to the changing air-core diameter. As the air-core grows with increasing flow rate, the effective exit area is reduced. The value of the discharge coefficient is in the range 0.6 – 0.7, which is much higher than in typical swirl nozzles. This can be explained by considering the high viscosity of the injected liquid. The higher viscosity increases the thickness of the liquid film, thus resulting in a higher effective exit area.

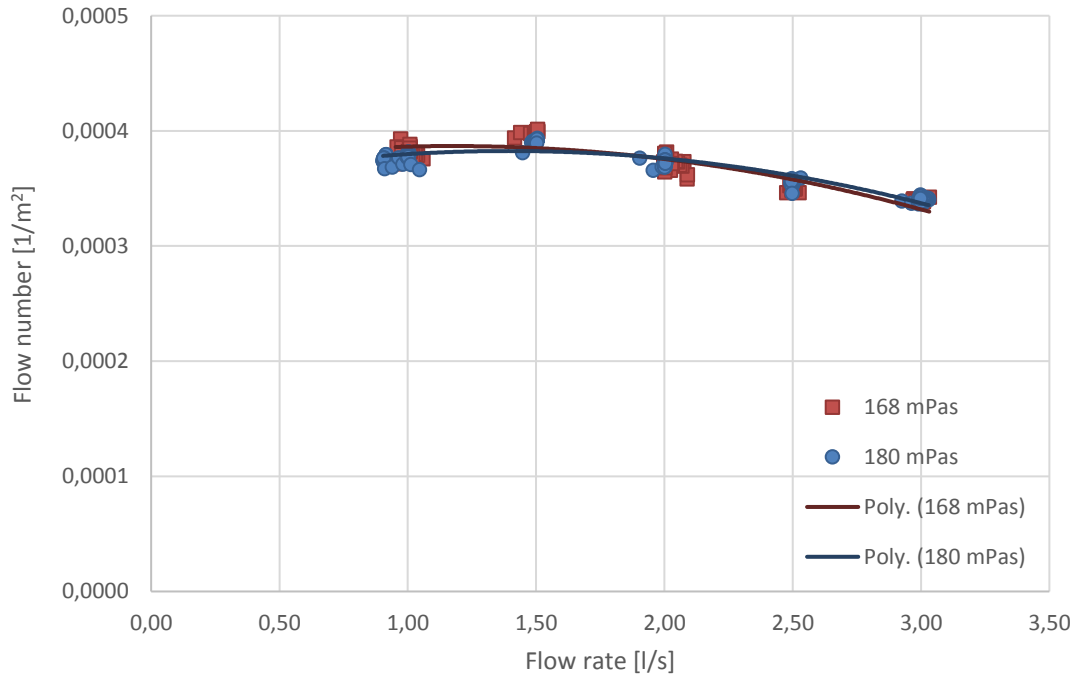


Figure 30. Flow number (FN) as a function of flow rate for viscosities of 168 and 180 mPas.

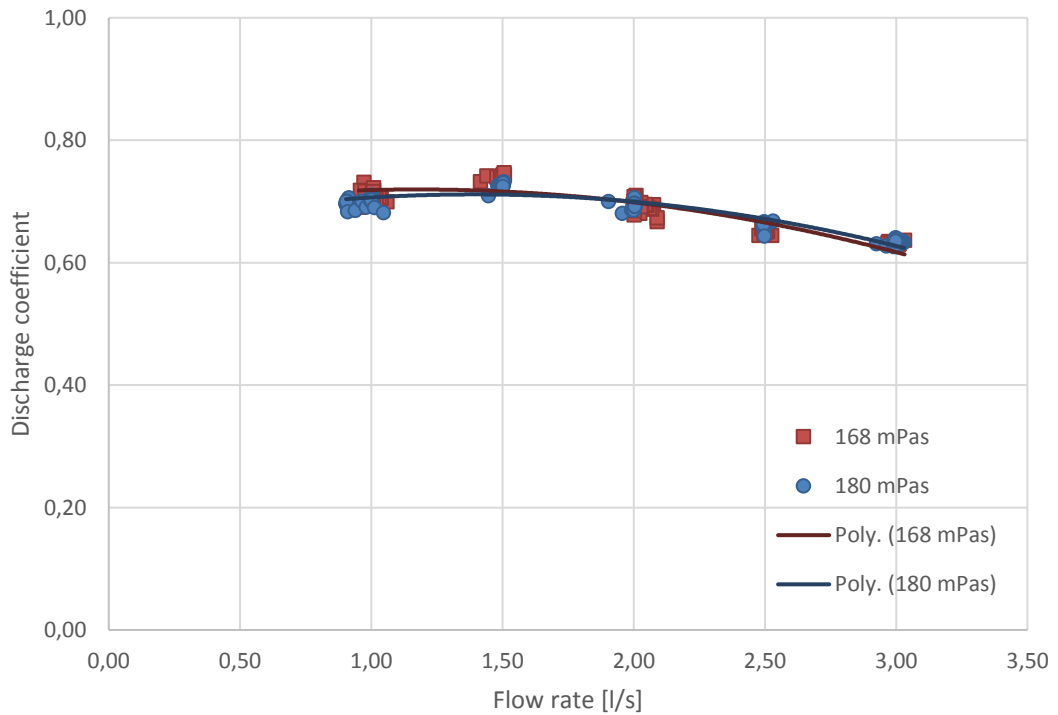


Figure 31. Discharge coefficient ( $C_d$ ) as a function of flow rate at viscosities of 168 and 180 mPas.

## 4.2 Spray cone angle and spray bend angle

The results of the spray angle measurement are shown in Fig. 32. The results showed a lot of fluctuations in the total spray angle, which was calculated based on the spray contour. The data can be seen to deviate as much as 20 – 30° from the average value. These types of fluctuations can be attributed to the spray being in the film forming flow regime,

where the left and the right-hand side fluctuate at different frequencies. Therefore, for example, if two large waves coincide on both sides, the measured spray angle will be large. Conversely, the spray angle will be small for fluctuations that are in opposing phases. The average spray angle was calculated based on 700 data points per flow rate.

The results show that on average,  $\theta$  is around  $50^\circ$  from the front view, and around  $55^\circ$  from the side view with minor changes across the flow rate range. This indicates that the spray cross-section is oval-shaped, which seems to be the case regardless of the viscosity. The shapes of the curves also show that, as the viscosity increased, the effect of the increasing flow rate on the spray angle decreased. This could be explained with the air-core reaching its maximum size faster due to a disproportionately large increase in flow friction with respect to increasing flow rate. The increased flow friction reduces the magnitude of the tangential velocity component, thus decreasing the strength of the swirling motion. When the air-core reaches an equilibrium, the spray angle becomes independent of injection pressure. At the viscosity level of 159 mPas, the spray angle has an increasing trend, which may indicate that the air-core is still in a developing stage.

The suggested empirical formulas for calculating  $\theta$  (see p. 19 – 20) failed to predict the spray angle accurately for the studied nozzle. This could be expected, since the formulas were derived for smaller size simplex nozzles, which have a different geometrical structure. However, it may be possible to formulate new coefficients for the equation, thus yielding a good fit to the current spray angle data.

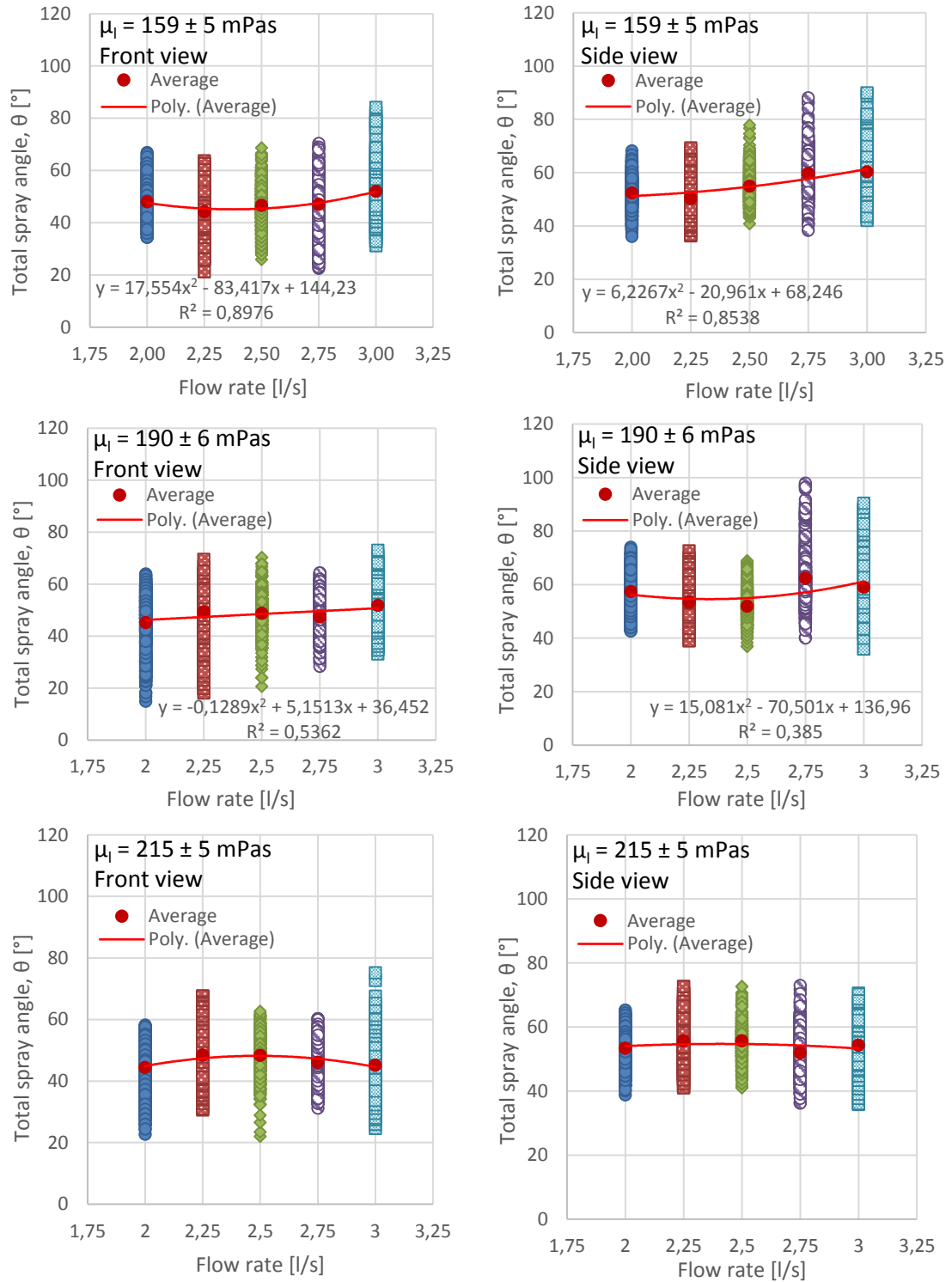


Figure 32. Visual spray angle as a function of flow rate from the front and the side at viscosities of 159, 190 and 215 mPas.

The difference between the left- and right-hand half-angles indicated bending of the spray towards the larger half-angle. These spray bend angles are shown in Table 2 for varying liquid viscosities and flow rates. The  $\theta_B$  values indicate that the spray is bent 2 – 8° towards the left-hand side from the front view and 6 – 12° to the right-hand side from the

side view. These bend angles changed as a function of liquid viscosity and flow rate. For example, increasing the flow rate tended to make the spray straighter, except for the front view at 159 mPas, where the spray bend angle actually increased with respect to flow rate. The effect of viscosity was to reduce bending from the front view and increase it from the side view. Appendix 2 shows sets of spray images at varying flow rate and viscosity, where the spray bending can be observed.

*Table 2. Average spray bend angles as a function of flow rate and viscosity (if  $\theta_B < 0$ , the spray is bent to the left, and otherwise to the right).*

$\dot{V} =$	Front view				
	2,00 l/s	2,25 l/s	2,50 l/s	2,75 l/s	3,00 l/s
$\mu_l = 159 \pm 5$ mPas	-2,4°	-2,0°	-4,8°	-4,7°	-5,4°
$\mu_l = 190 \pm 6$ mPas	-7,7°	-4,3°	-3,1°	-3,7°	-5,1°
$\mu_l = 215 \pm 5$ mPas	-5,6°	-3,9°	-2,4°	-2,2°	-2,7°
$\dot{V} =$	Side view				
	2,00 l/s	2,25 l/s	2,50 l/s	2,75 l/s	3,00 l/s
$\mu_l = 159 \pm 5$ mPas	9,0°	9,4°	8,5°	6,8°	6,0°
$\mu_l = 190 \pm 6$ mPas	10,1°	8,6°	9,0°	9,9°	7,7°
$\mu_l = 215 \pm 5$ mPas	11,6°	10,1°	10,1°	8,9°	7,5°

Based on the liquid distributions, it was also possible to calculate the effective spray angles ( $\phi_{e,tot}$ ), which indicate the angular locations of the centers of mass for the liquid distributions. By definition, the effective angle should be less than the visual spray angle. However, looking at Fig. 33, it can be seen that the effective spray angles were close to same or higher than the visual spray angles for the front and the side view, respectively. This can be explained by the difference in the measured cross-sections, which were 3.9 cm for the high-speed camera measurements and 28 cm for the patterning measurements. Therefore, these angles are not perfectly comparable.

From the front view,  $\phi_{e,tot}$  stays roughly 50° regardless of flow rate, whereas from the side view,  $\phi_{e,tot}$  is initially different and then approaches 60° at both viscosity levels. The initial difference could perhaps be due to a change in flow regime based on increased viscosity. It was observed that at flow rate of 2 l/s, the higher viscosity liquid produced a fan-type flow regime, which could potentially be a very elliptical hollow cone. However, since the state of the air-core is unknown, it is not clear if the air-core is collapsed or not. On the other hand, it is also possible that this discrepancy is a result of the poor resolution of our patterning measurements.

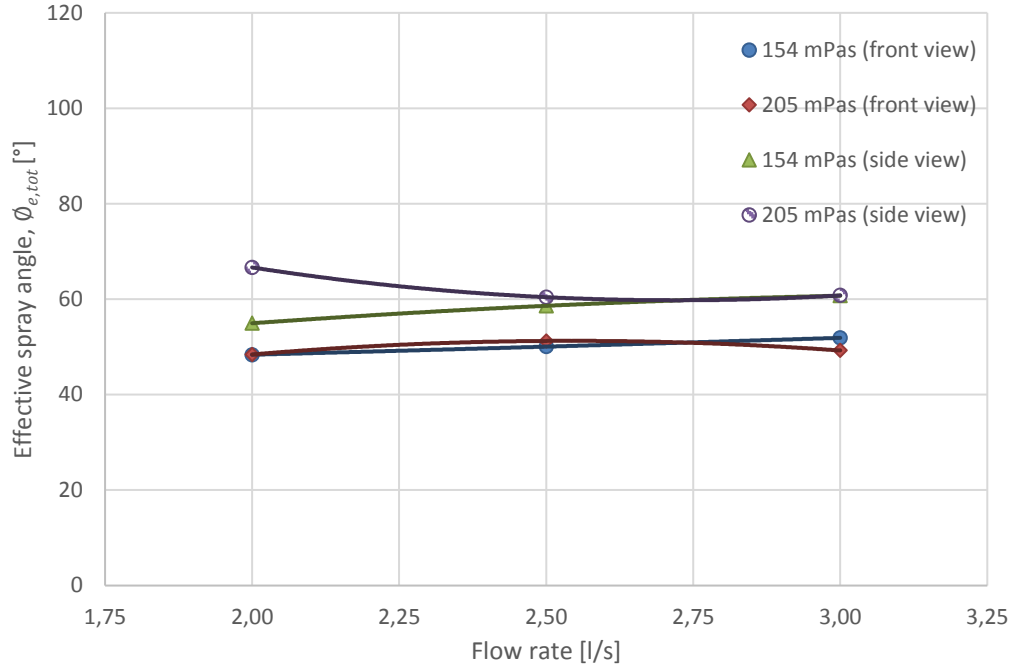


Figure 33. Effective spray angles from the front (patternator position:  $\varphi = 90^\circ$ ) and the side (patternator position:  $\varphi = 0^\circ$ ) at viscosities of 154 and 205 mPas.

### 4.3 Velocity of the liquid film

Tracking the bubbles with ImageJ was useful for determining not only the average velocity of the liquid film, but also the average air core size and film thickness. The bubble velocities were evaluated based on the average velocity of the tracks found by Trackmate. The detected tracks were filtered to reduce the amount of tracks to a manageable set of 150 tracks per flow rate. Having the same number of tracks for each flow rate made the data analysis easier. The collected data is shown in Fig. 34.

At 159 mPas, there were very few detected tracks in the middle portion of the spray at 3.00 l/s, which resulted from overexposure that hid the details in the spray. This occurred due to the spray being more turbulent and mixed at higher flow rates, which increased the amount of light scattering inside the liquid film. The primary way to avoid such overexposure would have been to increase the shutter speed, thus allowing less light to reach the film plane. This issue was limited to a single video file, as can be seen by observing the bubble tracking results for all the other flow rates and viscosities, where it is clear that the detected tracks are more evenly distributed. Furthermore, it is important to consider that the bubble velocities in the middle can have a gamma angle error of 9 %, although taking an average across the whole spray width does mitigate this error.

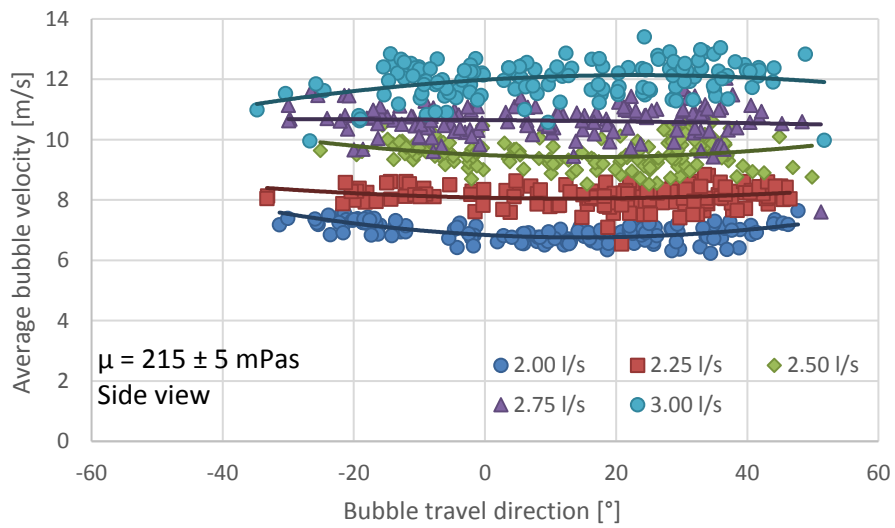
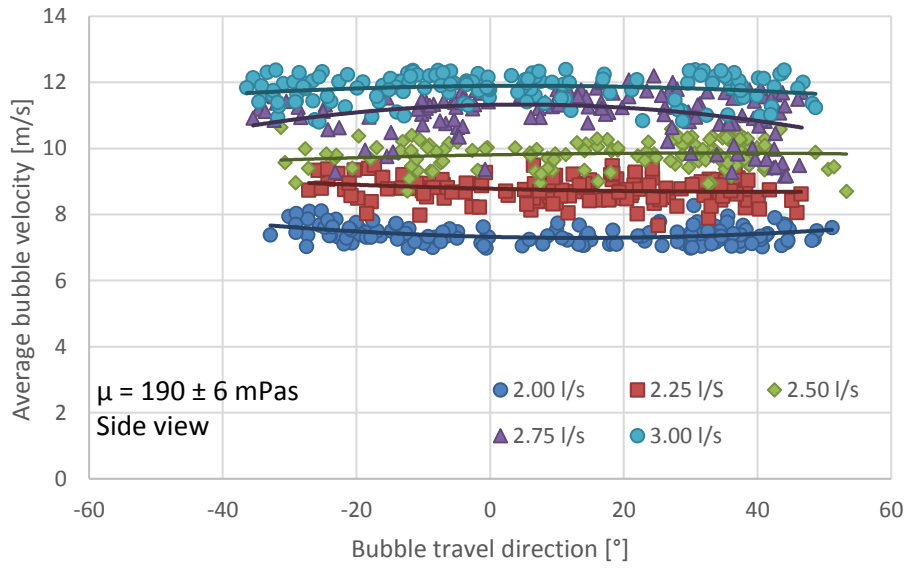
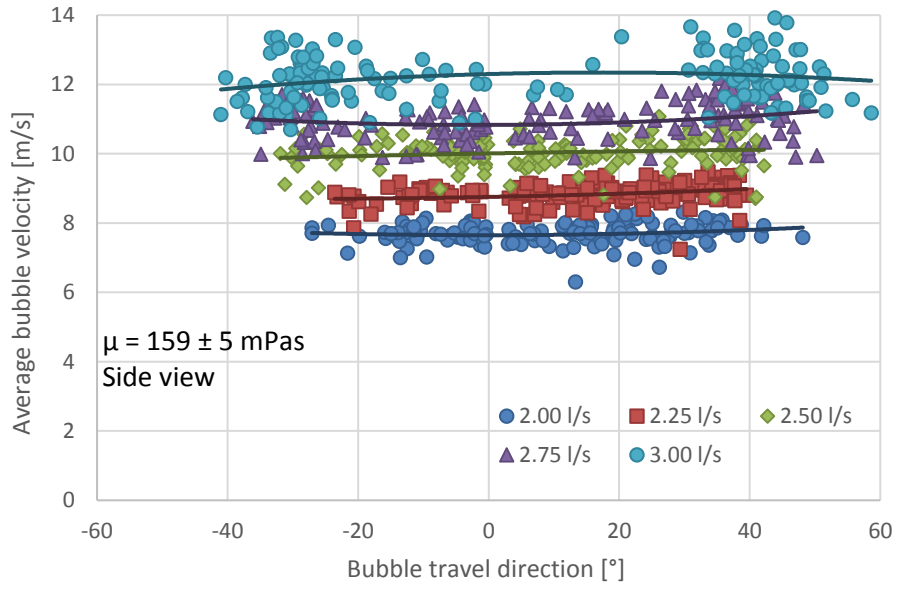


Figure 34. Data from bubble tracking at viscosities of 159, 190 and 215 mPas.



Taking an average of the bubble velocities corresponding to given a flow rate yields an estimation of the average velocity of the liquid film. Fig. 35 shows the average film velocity as a function of flow rate and viscosity. The average film velocity was in the range of 7 – 12 m/s with flow rate of 2 – 3 l/s. It can be seen that the average film velocity and flow rate have a linear relationship. Furthermore, higher viscosity seems to lower the average velocity for the liquid film.

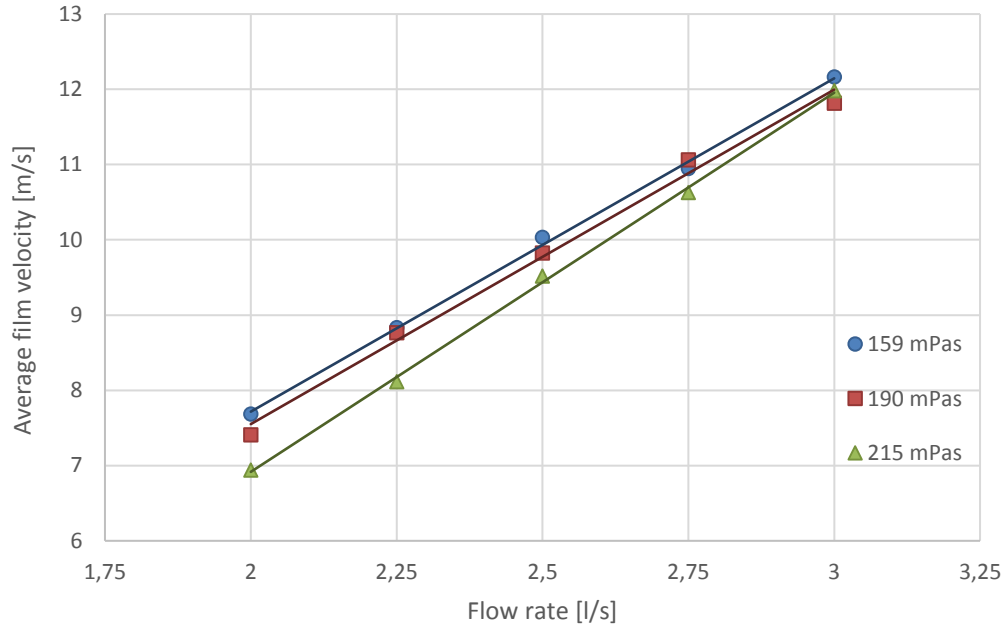


Figure 35. Average film velocity as a function of flow rate and viscosity.

#### 4.4 Estimated air-core area and liquid film thickness

The average air-core area ( $\bar{A}_a$ ) and liquid film thickness ( $\bar{t}$ ) are closely linked. For example, when the air core grows, the film thickness decreases and vice versa. Fig. 36 shows large differences in  $\bar{A}_a/A_o$  and  $\bar{t}$  at the lower end of the flow rate range. It seems that as the viscosity increases, the discrepancy is disproportionately larger. However, as the flow rate approaches 3 l/s, all the curves converge, which suggests that the air-core reaches a maximum size. This finding agrees with research by Datta and Som (2000) and Som and Mukherjee (1980), both of whom found that the air-core size reaches a maximum value beyond which it became independent of injection pressure. Our results indicated that the dimensionless air-core area was 24 – 35 % of the exit orifice area and the liquid film thickness was roughly 4 – 6 mm.

Furthermore, it can be seen that the higher the viscosity, the more the air-core expanded across the flow rate range. The change in air-core area did not seem to reflect a change in the total spray angles, which remained relatively stagnant. This suggests that having a high viscosity uncoupled the air-core area and the spray angle, which are typically connected. Compare, for example, Fig. 32 and 36, where it can be seen that the largest change in spray angle corresponds to the smallest change in air-core area and vice versa. At 215 mPas, the air-core area is increased by 42 %, while the spray angle stays almost constant across the 2 – 3 l/s flow rate range. Conversely, at 159 mPas, the air-core area increases by only 13 %, which coincides with a small increase in the spray angle.

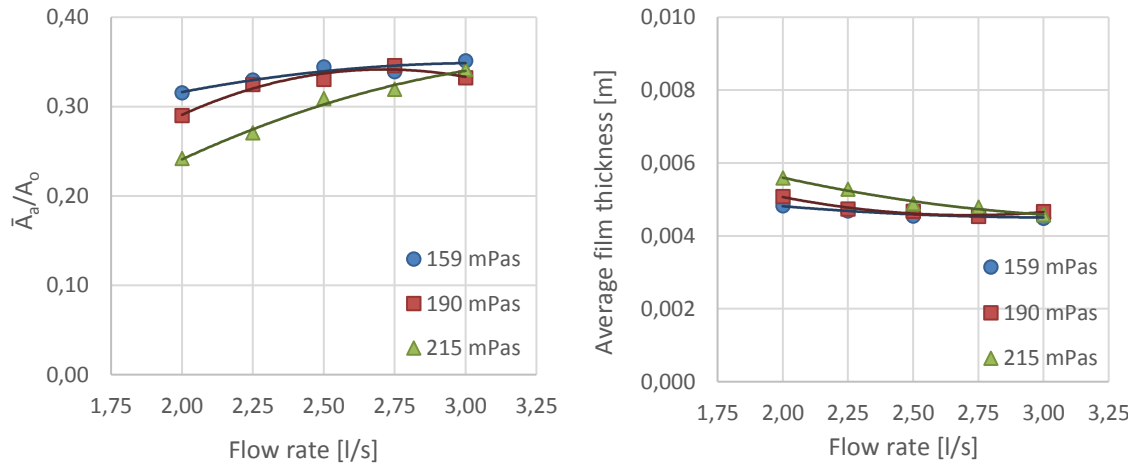


Figure 36. Average air-core area-to-exit orifice area ratio and average film thickness as functions of flow rate and viscosity.

#### 4.5 Liquid distributions

As Khavkin (2004) noted, the symmetry of the liquid distribution is affected by the non-uniformities in the thickness of the liquid film. This ties in with the stability of the air-core, since having an unstable air-core produces fluctuations in the thickness of the liquid film. Kim et al. (2009) showed that the air-core became unstable in their swirl nozzle, when  $\frac{l_s}{d_s}$  was changed from 1.06 to 1.27, which suggests that the transition to an unstable air-core could occur within this range. The currently studied nozzle had  $\frac{l_s}{d_s}$  of 1.26, which is right at the suggested limit. Since it is not exactly known, at which point this transition occurs, there is in fact a possibility that the currently studied nozzle might be characterized by instability. If this is the case, increasing the injection pressure will not increase air-core stability. However, there may be other factors that could affect the air-core stability, such as eccentricity of the exit orifice, large size of the nozzle and shape of the swirl chamber. For example, Som (2012) observed that a conical swirl chamber seemed to improve the air-core stability. This makes sense, since the swirl velocity increases as the liquid flows downwards in the swirl chamber. The studied nozzle design has a cylindrical swirl chamber, which is characterized by a helical air-core. This could definitely produce fluctuations in the thickness of the liquid film, thus decreasing the symmetry of the liquid distribution. Furthermore, the exit orifice-to-swirl chamber eccentricity should also be considered. Borodin et al. (1976, cited in Khavkin 2004) suggested that the eccentricity effect is limited, if  $\frac{2\varepsilon}{r_o} \leq 0.05$ . For our nozzle, this ratio was calculated to be 0.56, which is well over the suggested ratio. Therefore, the eccentricity probably contributed to the asymmetry of the liquid distribution.

Looking at Fig. 37 and 38, it is clear that increasing the flow rate and reducing the viscosity improve spray symmetry. In fact, the 2 l/s case with 205 mPas produced an especially unsymmetrical liquid distribution. With these flow parameters, a fan-type flow regime was observed, which seemed to occur due to the high viscosity level. The probable explanation for this is the absence of the air-core. Or perhaps there is only a partial air-core, which won't expand across the entire nozzle length. This is because having a higher viscosity reduces the swirl strength of the flow, thus hindering the formation of the air-

core. Furthermore, it can be observed that the peak flow rates occur at different radial locations depending on the circumferential location. This can be attributed to the spray bending and the oval shaped cross-section of the spray.

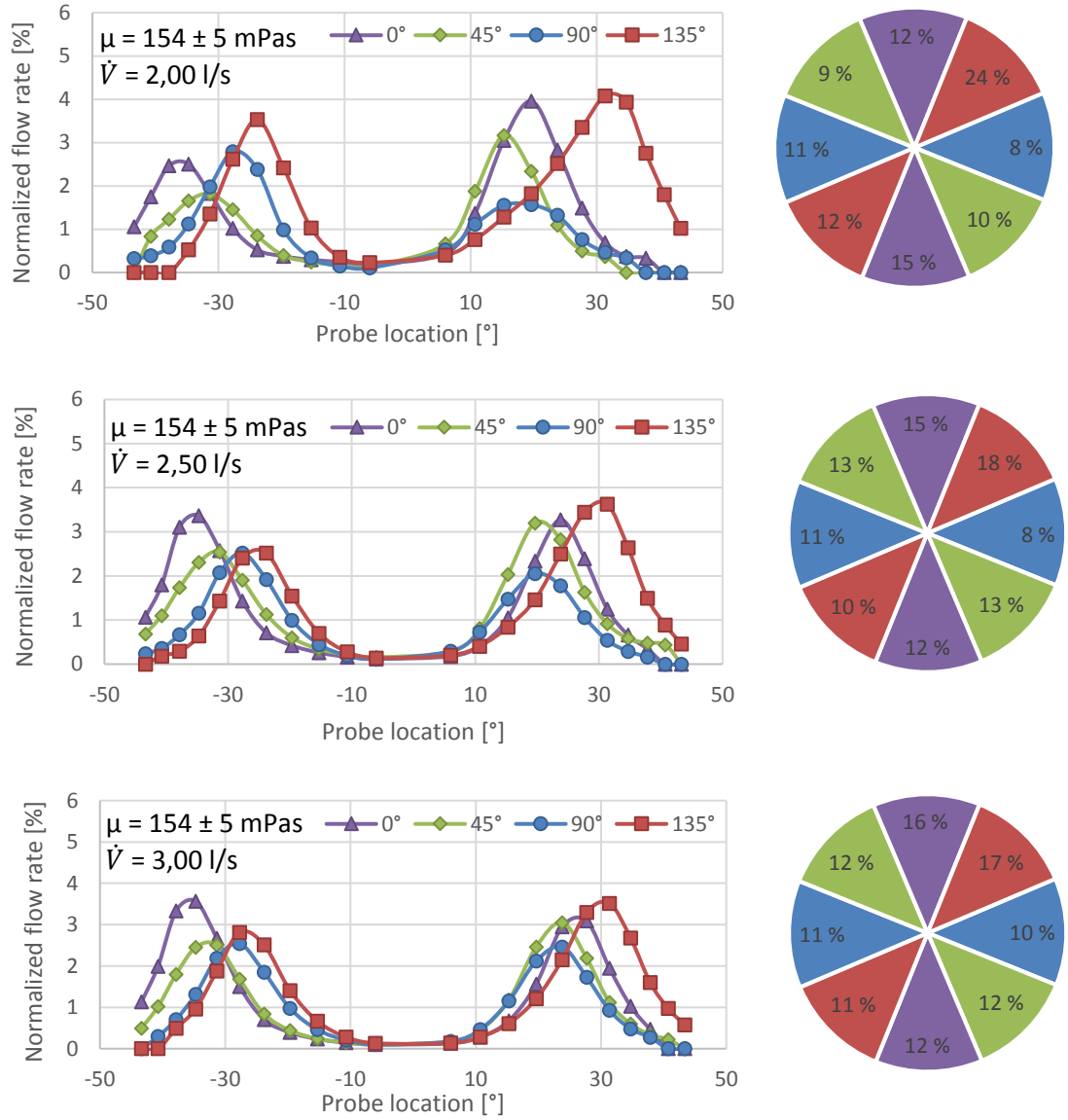


Figure 37. Radial and circumferential liquid distributions for patternator positions of 0°, 45°, 90° and 135° at liquid flow rates of 2.00, 2.50 and 3.00 l/s with viscosity of 154 mPas.

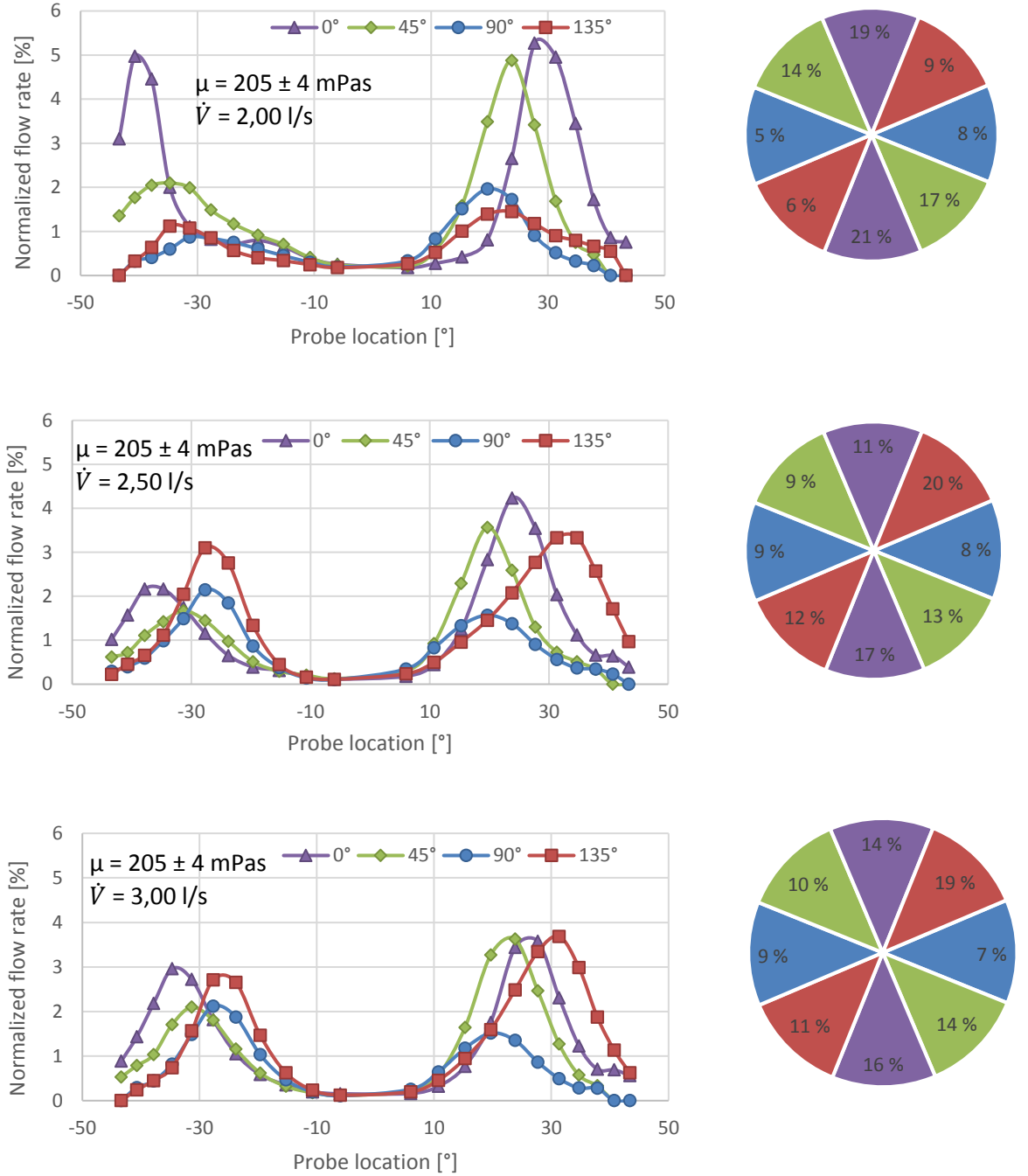


Figure 38. Radial and circumferential liquid distributions for patternator positions of 0°, 45°, 90° and 135° at liquid flow rates of 2.00, 2.50 and 3.00 l/s with viscosity of 205 mPas.

The collected circumferential distributions can be summarized into scalar values, which describe the spray symmetry. In our case, we decided to include  $\Gamma$ ,  $r_{min-max}$  and  $P_z$ . These indicators are 0 for the perfectly symmetrical spray. The calculated values are shown in Table 3. Out of these terms,  $\Gamma$  seemed to be most reliable indicator of spray symmetry, since it accounts for all the sectors and not just the sectors with maximum and minimum flow rates. Furthermore, it is also less sensitive to the amount of sectors in the

patterning measurement, which in our case was only 8. According to Tate (1960), patterning indexes of 7 % or less are typically acceptable for most applications. However, note that this limit is probably most applicable to viscosity levels that are close to 1 mPas.

We found that going from 154 to 205 mPas (33 % increase in viscosity) increased  $\Gamma$  from 34 % to 50 % (47 % increase) at 2 l/s and from 18 % to 31 % (72 % increase) at 3 l/s. This indicated that the spray symmetry not only became poorer with increasing viscosity, but also that the viscosity effect was more pronounced at higher flow rate. Increasing the flow rate had an opposite effect. When going from 2 l/s to 3 l/s at 154 mPas,  $\Gamma$  is reduced from 34 % to 18 % (47 % decrease). The same change in flow rate at 205 mPas reduced  $\Gamma$  from 50 % to 31 % (38 % decrease). This means that the spray symmetry improved with increasing flow rate. The effect was slightly stronger at 154 mPas. Overall, these  $\Gamma$  values were nowhere near the limit of 7 % that Tate (1960) mentioned.

*Table 3. Spray symmetry in terms of  $\Gamma$ ,  $r_{min-max}$  and  $P_z$  for at varying flow rate and viscosity.*

$\mu$ [mPas]	$\dot{V}$ [l/s]	$\Gamma$ [%]	$r_{min-max}$ [%]	$P_z$
154 ± 5	2,00	34	28,1	1,44
154 ± 5	2,50	21	42,5	0,94
154 ± 5	3,00	18	55,1	0,64
205 ± 4	2,00	50	18,5	1,55
205 ± 4	2,50	36	32,2	1,17
205 ± 4	3,00	31	31,8	1,16

## 5 Error analysis

### 5.1 Error in viscosity measurement

Determining the viscosity accurately was difficult due to changing liquid temperature and absorption of air into the mixture. Thus, the viscosity not only changed across samples, but also during the viscometer measurement. Therefore, multiple viscosity readings were obtained for a single liquid sample. To deal with the increasing temperature, 2 – 3 samples were taken during a measurement set. The following formula was used in getting a rough estimate of the error in the measured viscosity, while knowing that the viscometer had an error of 1 %:

$$\delta\mu_l = \frac{1}{2}(1.01\mu_{l,max} - 0.99\mu_{l,min}), \quad (36)$$

where  $\delta\mu_l$  = error in measured liquid viscosity,  $\mu_{l,max}$  = maximum measured viscosity and  $\mu_{l,min}$  = minimum measured viscosity.

Using equation (36), the magnitude of the error was estimated to be 4 – 6 %, which is a conservative estimate. This ensured that the true viscosity value was within the range with good level of confidence. The viscosity could then be expressed in terms of the average viscosity during an experiments as  $\bar{\mu}_l \pm \delta\mu_l$ .

## 5.2 Error in high-speed camera measurements

It was observed that increasing the distance of the measurement cross-section from the nozzle produced a linear increase in the measured spray angle. This observation is in direct contradiction with literature, where it is stated that the largest values of spray angle can be measured in the immediate vicinity of the nozzle exit. Supposedly, the aerodynamic effects bend the spray contour downwards, thus reducing the measured spray angle as the distance from the nozzle is increased. In our case, the linear increase in the width of the spray contour was probably caused by the increasing fluctuations of the spray contour. Furthermore, having such a large nozzle may change the circumstances.

To get an accurate intermediate value, the measurement cross-section was chosen such that it was 100 pixels below the nozzle, which corresponds to roughly 3.9 cm in the 1024x1024 pixel image with a 40 cm scale. This ensured not only that the amount of fluctuations remained moderate, but also that clear edges were visible in the binary image. Having the measurement cross-section too low would reduce the visibility due to the increased amount of aerodynamic distortions such as separated ligaments and droplets obstructing the view.

The error in the spray angle measurement can have variety of different sources including edge-detection error, nozzle and camera misalignments, and other errors associated with the perspective of the camera. The edge-detection errors can be divided into two categories: the error in setting the edge-points at the exit orifice manually and the error in the automated edge-detection with Matlab. For example, we can assume that the user can set the spray edge location within  $\pm 3$  pixels of the correct location on the left and the right-hand side. This produces two independent errors, which can be added in quadrature to evaluate the combined error in terms of the measured spray angles. The resulting error was found to be less than  $1.5^\circ$  for the total spray angle.

Bayvel and Orzechowski (1993, p. 398) suggest that the error associated with finding the spray edge from an image is  $\pm 2\%$  and  $\pm 5\%$  for low and high injection pressures, respectively. In their estimation, this error can be reduced by having an exposure times of  $1\ \mu\text{s}$  or less and good image sharpness. In our case, the injection pressure is relatively low (0.25 – 1 bar), which means that error estimate of  $\pm 2\%$  would be appropriate. Furthermore, Taylor (1982, p.10) noted that discrepancies in the measured value will not necessarily give insight into the reliability of the measurement. Therefore, since the true location of the spray edge changed with each frame, it was impossible to assess the error via statistical analysis.

Another consideration is whether or not the code detecting the spray shape correctly. For example, the image binarization can fail due to insufficient lighting or the use of an inappropriate threshold value. Having too low a threshold produces noise in the binary image, thus causing the measured visual spray angle to appear wider. Conversely, having too high a threshold may leave the edge undetected, which produces an incomplete binary image. This can create holes in the spray contour, thus underestimating the visual spray angle. However, this type of error is easy to detect by observing the produced images, while the Matlab code is being run. Once detected, the threshold can be adjusted appropriately, or the measurement can be redone with improved lighting. Furthermore, since the sample size is 700 frames, the effect of few subpar frames is insignificant in terms of the accuracy of the calculated average.

According to Robbe et al. (2014), the most important error to consider in high-speed camera measurement is the gamma angle uncertainty, which occurs when the object is moving non-orthogonally with respect to the camera. Therefore, the camera measures the apparent traveled distance, which is slightly different from the real one. This is the case,

for example, in the film velocity measurement, since the film is moving towards the camera in an angle corresponding to the spray half-angle. With an estimated average half-angle of  $25^\circ$  and camera distance of 2 m, we get gamma angle error of 9 %. This error applies most to the bubble velocities measured in the middle of the spray and less so to the velocities at the edges.

### 5.3 Error in patternation measurement

Mechanical patternation can have a variety of error sources including number of sectors, collection efficiency, measuring the liquid levels, patternator-to-nozzle misalignment, and timing of the measurement duration. To obtain a valid result, it is important to consider the effects these parameters might have on accuracy of the measurements.

Tate (1960) noted that spray patternation measurements are affected by the number of sectors in the patternator. In fact, fewer sectors appear to produce better results, but this is due to the poor resolution of the measurement. This is because having less sectors produces an averaging effect on the measured patternation. For example, the spray might have small areas of disproportionately high or low flow rate, which either remain uncollected or balance each other out due to the low resolution. Thus, having a higher number of sectors yields a more detailed and accurate representation of the liquid distribution. It is suggested that at least 12 sectors should be employed. However, in our case, the measurement was limited to 8 sectors.

This is tied to the concept of collection efficiency, which is defined as the ratio of collected and total flow. Having a higher collection efficiency ensures that a larger percentage of the flow is accounted for. Therefore, a high collection efficiency is recommended. With the 8 sector measurement, our patternator collected roughly 10 – 12 % of the total flow. This coincided well with the collection area: the angle of a measured sector was roughly  $4.5^\circ$  for a  $45^\circ$  sector, which is exactly 10 % of the total area. Thus, 88 – 90 % of the flow is uncollected, which leaves a lot of room for error. For example, thin strips of higher flow rate would go unnoticed, if it happened to fall in between the collected areas. The assumption here is that the collected flow in the  $4.5^\circ$  sector represents the flow in the whole  $45^\circ$  sector. This assumption is probably reasonable for the more developed hollow-cone flow, but loses validity as the flow becomes extremely asymmetrical.

When taking images of the liquid levels in the patternator (see Fig. 26), we had to consider perspective distortions and the gamma angle error. To minimize the perspective error, the camera was set 3 m away from the patternator. Furthermore, the gamma angle error was eliminated by taking the images perpendicular to the patternator facade. Furthermore, reading the liquid levels from the images may cause slight errors. If we assume that the person analyzing the image can set the end points with  $\pm 5$  pixel accuracy, the error for a single liquid level would be  $\pm 10$  pixels. With the scale of 0.15 mm/pixel, the amount of error becomes  $\pm 1.5$  mm. The relative error is a function of the measured height, which varied in the range 5 – 200 mm. This results in relative error of 1 – 30 %, where the lowest error corresponds to the highest liquid level.

The amount of error and the prevalent error sources are dependent on the used patternation method. For example, Hicks et al. (2008) compared the effects of angular misalignment and nozzle-to-patternator center offset for optical and mechanical patternation. They found that mechanical patternation was less sensitive to angular alignment and more sensitive to offset. In fact, the patternation number ( $P_z$ ) changed approximately 43 %/mm of offset. Although this highlights the importance of minimizing the offset in mechanical patternation, it is important to consider that their result was obtained for a small scale nozzle. In our experiments, the alignment of the nozzle and patternator centers was checked manually using a bullet string, which was hung from the nozzle exit orifice. With

this method the offset could be reduced to 0.5 cm or less. Furthermore, the angular alignment was checked in two directions with an electronic leveling device for the patternator table and the nozzle. The maximum tolerance for these angular misalignments was  $1^\circ$ , although the measured angles were typically between  $0^\circ - 0.5^\circ$ . If the nozzle and the table were tilted in the opposite directions, the maximum angular deviation would be  $2.0^\circ$  at worst.

Some error is also produced due to the manual operation of the sampling gate. The time between opening/closing the sampling gate and starting/stopping the stopwatch could be up to 1 s. With the minimum sampling time of 33 s, the sampling time error can be estimated to be 6 % or less depending on the measurement duration.

## 6 Conclusions

This thesis studied spraying of high-viscosity liquid with a specifically designed large pressure-swirl nozzle. The main focus was on total spray angle, spray bend angle, film velocity, nozzle pressure-drop, and liquid distribution. The measurements involved developing a method for obtaining spray angle data from video files, using ImageJ to extract film velocity data, designing a mechanical patternator to study the liquid distributions, and measuring the liquid viscosity. The aim was to investigate the spray characteristics of the nozzle design with viscosities in the range of 150 – 225 mPas and flow rates of 2 – 3 l/s.

Pressure data from an upstream pressure-sensor was corrected to calculate nozzle pressure-drop. It was found that increasing the viscosity from 168 to 180 mPas had a negligible effect on the nozzle pressure-drop, which varied between 0.35 – 0.96 bar for flow rates of 2 – 3 l/s at both viscosity levels. The nozzle pressure-drop was used to calculate discharge coefficient ( $C_d$ ) and flow number ( $FN$ ), both of which had a reducing trend with respect to increasing flow rate. This was attributed to the increasing air-core diameter. The value of the discharge coefficient was in the range 0.6 – 0.7, thus being higher than in typical swirl nozzles. This can be explained by considering how having a high liquid viscosity produces a smaller air-core, thus increasing the liquid film thickness.

The total spray angle ( $\theta$ ) was found to be, on average, around  $50^\circ$  and  $55^\circ$  from the front and side view, respectively. This indicated that the spray cross-section was oval-shaped. In general,  $\theta$  did not change much across 2 – 3 l/s flow rate range, except for the 159 mPas case, where a slightly increasing trend was observed for both the front and side view. Furthermore, only minor changes in the spray angles occurred with increasing viscosity. The empirical formulas for predicting  $\theta$  did not produce good results for the studied nozzle due to its unconventional geometrical structure and large size.

Our results showed that the spray was characterized by a relatively large amount of bending, since the spray bend angle ( $\theta_B$ ) varied between  $2 - 8^\circ$  towards the left-hand side from the front view and  $6 - 12^\circ$  towards the right-hand side from the side view. The bending was more pronounced, when seeing the spray from the side.

The average film velocity ( $\bar{v}_f$ ) was observed to be in the range 7 – 12 m/s with flow rate range of 2 – 3 l/s. The film velocity was underestimated slightly due to parts of the flow being towards the camera to varying degree. This error was estimated to be roughly in the 9 % range. Based on the average velocity, the average air-core area was calculated to be 24 – 35 % of the exit orifice area for the 2 – 3 l/s flow rate range. The air-core area increased as a function of flow rate. The liquid film thickness, on the other hand, was inversely proportional to the air-core area. Thus, when flow rate was increased from 2 l/s to 3 l/s, the film thickness reduced from 6 mm to 4 mm, respectively. Furthermore, it was



found that  $\bar{v}_f$ ,  $\bar{A}_a$ , and  $\bar{t}$  had a converging trend, which could be an indication of the air-core reaching its maximum size for the studied nozzle design.

Spray symmetry was quantified in terms of the patternation index ( $\Gamma$ ), which is the sum of each sectors deviation (in terms of %) from the ideal distribution. If  $\Gamma = 0\%$ , the spray is perfectly symmetrical. At 154 mPas, the experiments yielded  $\Gamma$  values of 34 %, 21 % and 18 % for flow rates of 2, 2.5 and 3 l/s, respectively. At worst, almost a quarter of the collected flow was found in a 1/8th sector. At 205 mPas, the corresponding  $\Gamma$  values were 50 %, 36 % and 31 %. Thus, the spray could definitely be considered highly unsymmetrical, since all of the indexes were way above the limit of 7 %.

Increasing the viscosity from 154 mPas to 205 mPas, increased  $\Gamma$  by 47 – 72 %, thus indicating much poorer spray symmetry with increasing viscosity. This effect may be due to changes in the flow regime and reduction in air-core stability. Conversely, increasing the flow rate from 2 l/s to 3 l/s reduced  $\Gamma$  by 38 – 47 %. This was a noticeable improvement in spray symmetry. Thus, increasing the flow rate beyond 3 l/s might be beneficial considering that the pressure losses were less than 1 bar with the current maximum flow rate of 3 l/s. The increased injection pressure would produce a more stable air-core, thus improving spray symmetry. However, it is also possible that diminishing returns will be encountered, when the injection pressure is increased to any significant degree.

The liquid distribution measurements had quite a low resolution circumferentially with only eight sectors. Therefore, future research on this nozzle design should definitely consider investigating the spray patternation using a higher resolution method. Furthermore, this thesis did not study the air-core and film thickness directly, but rather based on average velocity of the liquid film. Direct measurements on the air-core would allow a more detailed analysis of the flow behavior, since many of the studied variables are affected by the state of the air-core. This could be, for example, a high-speed camera measurement of the air-core shape and stability through a transparent nozzle of similar geometry. It would also be interesting to study the effect of increasing the injection pressure beyond 1 bar to see how it affects the spray symmetry, air-core and spray angles. This could be combined with measuring the droplet size distributions, which were not studied in this work.

## 7 Sources

Adams T. N., Frederick W. J., Grace T. M., Hupa M., Iisa K., Jones A. K., Tran H. (1997) Kraft Recovery Boilers, *Tappi Press*, ISBN 0-9625985-9-3.

Babu K. R., Narasimhan M. V., Narayanaswamy, K. (1982) Correlations for Prediction of Discharge Rate, Cone Angle and Air Core Diameter of Swirl Spray Atomizers, in: *Proceedings of the 2nd International Conference of Liquid Atomization and Spray Systems*, Madison, WI, pp. 91 – 97.

Ballester J., Dopazo C. (1994) Discharge coefficient and spray angle measurements for small pressure-swirl nozzles, *Atomization and Sprays*, 4, pp. 351 – 367.

Bayvel L., Orzechowski Z. (1993) Liquid atomization, *Taylor & Francis*, ISBN 0-89116-959-8

Borodin W. A., Ditiakin Y. F., et al. (1976) Atomization of liquids, Moscow: Mashinostroenie.

Chinn J. J. (2008) The Numerics of the Swirl Atomizer, *Institute of Liquid Atomization and Spray Systems*, Sep. 8 – 10, Como Lake, Italy, Paper ID: ILASS08-1-16.

Chen S. K., Lefebvre A. H., Rollbuhler J. (1993) Factors influencing the circumferential liquid distribution form pressure-swirl atomizers, *Journal of Engineering for Gas Turbines and Power*, 115(1), pp. 447 – 452.

Chen S. K., Lefebvre A. H., Rollbuhler J. (1992) Factors Influencing the Effective Spray Cone Angle of Pressure-swirl Atomizers, *Journal of engineering for gas turbines and power*, 114, pp. 97 – 103.

Cohen J. M., Rosfjord T. J. (1991) Spray patternation at high pressure, *Journal of propulsion and power*, 7(4), pp. 481 – 487.

Czernik S., Bridgwater A. V. (2004) Overview of Applications of Biomass Fast Pyrolysis Oil, *Energy & Fuels*, vol. 18, pp. 590 – 598, doi: 10.1021/ef034067u.

De Corso S. M., Kemeny G. A., Pittsburgh E. (1956) Effect of Ambient and Fuel Pressure on Nozzle Spray Angle, *Trans. ASME*, 79(3), pp. 607 – 615.

Dullenkopf K., Willman M., Wittig S., Schöne F., Stieglmeier M., Tropea C., Mundo C. (1998) Comparative Mass Flux Measurement in Sprays using a Patternator and the Phase-Doppler Technique, *Particle & Particle Systems Characterization*, 15, pp. 81 – 89.

Datta A., Som S. K. (2000) Numerical prediction of air-core diameter, coefficient of discharge and spray cone angle of a swirl spray pressure nozzle, *International Journal of Heat and Fluid Flow*, 21, pp. 412 – 419, PII: S 0 1 4 2 - 7 2 7 X ( 0 0 ) 0 0 0 0 3 – 5.

Amini G. (2016) Liquid flow in a simplex swirl nozzle, *International Journal of Multi-phase Flow*, vol. 79, pp. 225 – 235, doi: <http://dx.doi.org/10.1016/j.ijmultiphaseflow.2015.09.004>.

Halder M. R., Dash S. K. Som S. K. (2002) Initiation of air core in a simplex nozzle and the effects of operating and geometrical parameters on its shape and size, *Experimental Thermal and Fluid Science*, 26, pp. 871 – 878, PII: S08 9 4-177 7( 0 2 )0 01 5 3-X.

Hicks P. G., Sivathanu Y., Lim J. (2008) Optical and Mechanical Patternation of a High Flow Rate Industrial Gas Turbine Nozzle, *ILASS Americas, 21<sup>st</sup> Annual Conference on Liquid Atomization and Spray Systems*.

International Organization of Standardization (2017) *ISO 8217: Fuel standard for marine distillate fuels*.

Jones A. R. (1982) Design optimization of a large pressure jet atomizer for power plant, *The 2<sup>nd</sup> International Conference of Liquid Atomization and Spray Systems*, Madison, Wisconsin, U.S.A.

Kast W., Gaddis E. S., Wirth K. E., Stichlmair J. (2010) L1 Pressure Drop in Single Phase Flow. In: *VDI Heat Atlas*. Springer, Berlin, Heidelberg, doi: [https://doi.org/10.1007/978-3-540-77877-6\\_70](https://doi.org/10.1007/978-3-540-77877-6_70).

Khavkin Y. I. (2004) *The Theory and Practice of Swirl Atomizers*, Taylor & Francis, ISBN: 1-56032-975-0.

Kooij S., Sijs R., Denn M. M., Villiermaux E., Bonn D. (2018) What determines the drop size in sprays?, *Physical Review X*, 8, doi: 10.1103/PhysRevX.8.031019.

Lefebvre A. H., Vincent G. M. (2017) *Atomization and Sprays*, 2nd ed., CRC Press, ISBN: 9781498736268.

Lehto J., Oasmaa A., Solantausta Y., Kytö M., Chiaramonti D. (2013) Fuel oil quality and combustion of fast pyrolysis bio-oils, *VTT Technology 87*, Espoo, Finland, ISSN: 2242-122X.

McVey J. B., Russel S., Kennedy J. B. (1986) High-resolution patternator for the characterization of fuel sprays, *Journal of propulsion and power*, 3(3), pp. 202 – 209.

Miikkulainen P. (2006) Spray formation of high dry solids black liquor in recovery boiler furnaces, *TKK Dissertations 53*, ISBN-13 978-951-22-8507-5.

Ortman J., Lefebvre A. H. (1985) Fuel distributions from pressure-swirl atomizers, *Journal of propulsion and power*, 1(1), pp. 11 – 15.

Rizk N. K., Lefebvre A. H. (1987) Prediction of Velocity Coefficient and Spray Cone Angle for Simplex Swirl Atomizers, *International Journal of Turbo and Jet engines* 4, pp. 65 – 73.

- Reddy K. U., Mishra D. P. (2008) Studies on Spray Behavior of a Pressure Swirl Atomizer in Transition Regime, *Journal of Propulsion and Power*, 24(1), pp. 74 – 80, doi: 10.2514/1.31156.
- Robbe C., Nsiampa N., Oukara, A. Papy A. (2014) Quantification of uncertainties of high-speed camera measurements, *International Journal of Metrology and Quality Engineering*, 5, doi: 10.1051/ijmqe/2014007.
- Rosfjord T. J., Russel S. (1987) Nozzle Design and Manufacturing Influences on Fuel Spray Circumferential Uniformity, *Journal of Propulsion*, 5(2), pp. 144 – 150.
- Schlichting H., Gersten K. (2000) Boundary-layer theory, 8<sup>th</sup> edition, *Springer*, Berlin, ISBN 3-540-66270-7
- Schneider C. A., Rasband W. S., Eliceiri, K. W. (2012) NIH Image to ImageJ: 25 years of image analysis, *Nature Methods*, 9(7), pp. 671-675
- Shaughnessy, E. J., Jr. Katz, I. M. Schaffer, J. P. (2005). Introduction to Fluid Mechanics (OUP Edition). *Oxford University Press*.
- Som S. K. (2012) Air core in pressure swirl atomizing nozzles, *Atomization and Sprays*, 22(4), pp. 283 – 303, 1044–5110/12/\$35.00
- Som S. K., Mukherjee S. G. (1980) Theoretical and experimental investigation on the formation of air core in a swirl spray atomizing nozzle, *Applied Scientific Research*, 36, pp. 173 – 196, 0003-6994/80/0363-0173\$03.60.
- Kim S., Taeock K., Dongjun K., Youngbin Y. (2009) Effect of geometric parameters on the liquid film thickness and air core formation in a swirl injector, *Measurement Science and Technology*, 20(1), doi:10.1088/0957-0233/20/1/015403.
- Swithebark J., Ewan B. C. R., Swithebark J. R., Taylor D. S. (1985) Aerial agricultural spray drift minimization, 3<sup>rd</sup> *International Conference of Liquid Atomization and Spray Systems*.
- Tate R. W. (1960) Spray Patternation, *Equipment & Design*, 52(10), pp. 49 – 55.
- Taylor G. I. (1932) The viscosity of a fluid containing small drops of another fluid.
- Taylor J. R. (1982) An introduction to error analysis: the study of uncertainties in physical measurements, *University Science Books*, ISBN: 0-935702-42-3
- Tinevez J., Perry N., Schindelin J., Hoopes G. M., Reynolds G. D., Laplantine E., Bednarek S. Y., Shorte S. L., Eliceiri K. W. (2017) TrackMate: An open and extensible platform for single-particle tracking, *Methods*, 115, pp. 80 – 90.
- Versluis M. (2013) High-speed imaging in fluids, *Experiments in Fluids*, 54, doi: 10.1007/s00348-013-1458-x.

Wimmer E., Brenn G. (2013) Viscous flow through the swirl chamber of a pressure-swirl atomizer, *International Journal of Multiphase Flow*, 53(1), pp. 100 – 113 doi: <http://dx.doi.org/10.1016/j.ijmultiphaseflow.2013.02.003>.

Zhike L., Dahuan Z., Wenxi T., Guanghui S., Suizheng Q. (2014) Experimental study on spray characteristics of pressure-swirl nozzles in pressurizer, *Annals of Nuclear Energy* 63, pp. 215 – 227.

# Appendix 1

## Matlab-code, VideoAnalysis.m:

```
warning('off', 'images:initSize:adjustingMag');
close all;
clc;

%Getting framedata from video file:

vidObj = VideoReader('\\h \#"0"ome.org.aalto.fi\koivish3\data\Documents\MATLAB\Example_video_file.avi');

vidHeight = vidObj.Height;
vidWidth = vidObj.Width;

s = struct('cdata',zeros(vidHeight,vidWidth,3,'uint8'),'colormap',[]);

%Time settings in seconds

vidObj.CurrentTime = 0.00; %Starting time

k = 1;

while vidObj.CurrentTime <=1 %Change the run time here
    s(k).cdata = readFrame(vidObj);
    k = k+1;
end
testim = histeq(s(1).cdata);
imshow(testim)

%Run this section only to find the edges of the nozzle exit orifice
%Set the points in FrameAnalysis2

%%

%Initializing

i = 1;
thetaLeft =zeros(length(s)-1,1);
thetaRight = zeros(length(s)-1,1);

%Analysing each of the frames using FrameAnalysis2

while i < length(s)
    [thetaL,thetaR, I] = FrameAnalysis2(s(i).cdata);

    thetaLeft(i) = thetaL;

    thetaRight(i) = thetaR;

    i = i+1;
```

```

end
theta = thetaLeft + thetaRight;

%Saving the results in excel: change the columns as needed

xlswrite('\\h \#"0"ome.org.aalto.fi\koivish3\data\Desktop\Spray angle
data.xlsx', theta, 'U4:U2003');
xlswrite('\\h \#"0"ome.org.aalto.fi\koivish3\data\Desktop\Spray angle
data.xlsx', thetaRight, 'V4:V2003');
xlswrite('\\h \#"0"ome.org.aalto.fi\koivish3\data\Desktop\Spray angle
data.xlsx', thetaLeft, 'W4:W2003');

```

## Matlab-code, FrameAnalysis2.m:

```

function [thetaL,thetaR, I] = FrameAnalysis2(frame)
%Enhancing the image

I = frame;
I = histeq(I);

%Comment or uncomment "rgb2gray" if video is color or grayscale

I = rgb2gray(I);
I = imbinarize(I,0.55); %Change the limit to fit the light level
of the video
I = imfill(I,'holes');
I = bwareaopen(I,2000); %This removes disconnected pixel chunks

%%

%Finding the spray boundaries
%Set the UL and UR according to the nozzle exit orifice edge coordi-
nates

UL = [192 491];
UR = [192 551];

%Change the llim to set the measurement cross-section

llim = 292;

%Lower left boundary
i = 1;
while I(llim,i)==0
    i = i + 1;
end
llb = i;

%Lower right boundary
i = 1;
while I(llim,1025 - i)==0
    i = i + 1;
end

```

```

lrb = 1025 - i;

%%

%Calculating the half-angles

thetaL = atand((UL(2) - llb)/(llim - UL(1)));

thetaR = atand((lrb - UR(2))/(llim - UR(1)));

%%

%Visualization

imshow(I)
s1 = line([llb,UL(2)], [llim,UL(1)], 'Color','m', 'LineWidth',2);
s2 = line([lrb,UR(2)], [llim,UR(1)], 'Color','m', 'LineWidth',2);

end

```



## Appendix 2

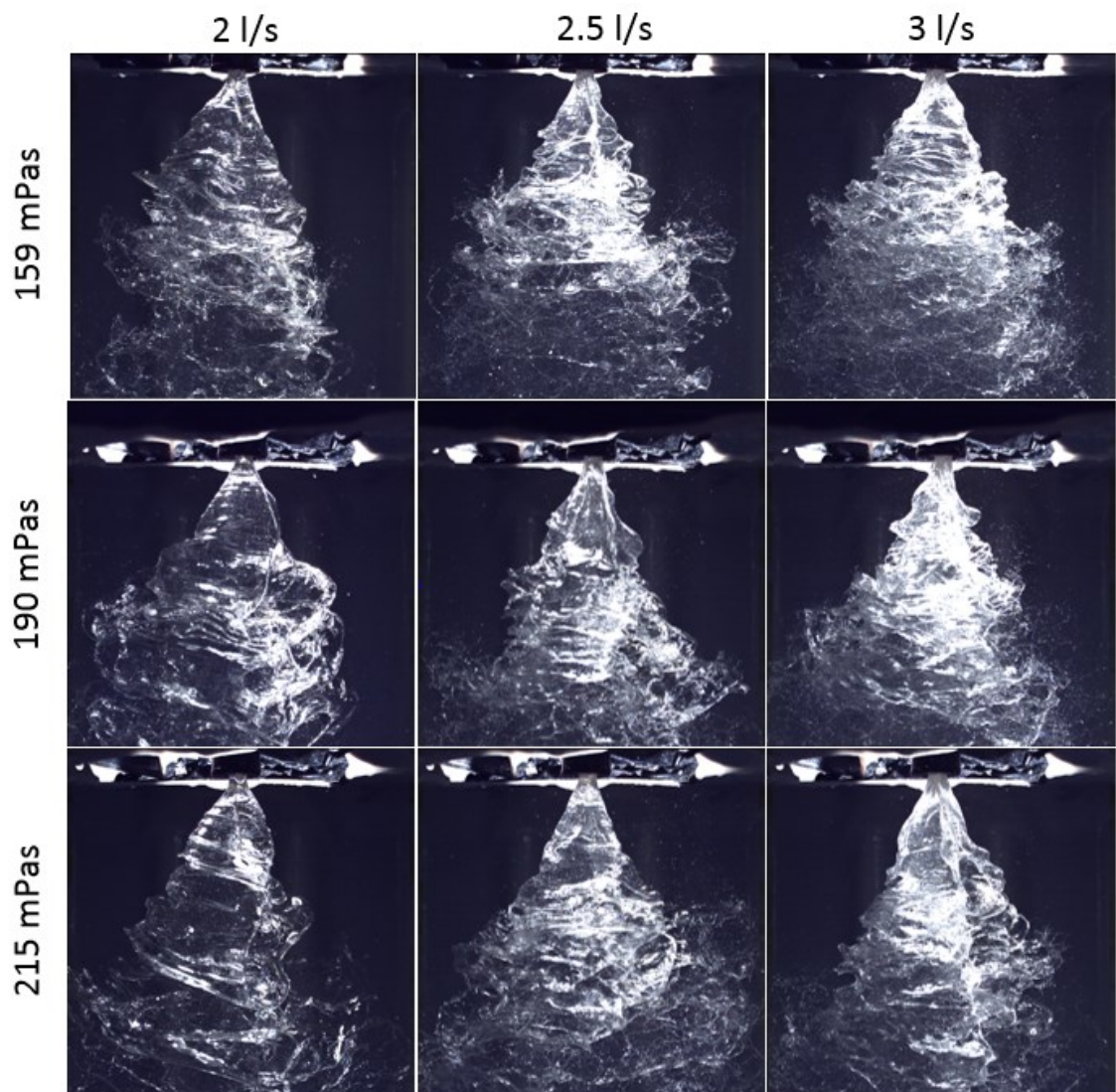


*Figure 39. Spray images at varying flow rate and viscosity (front view).*

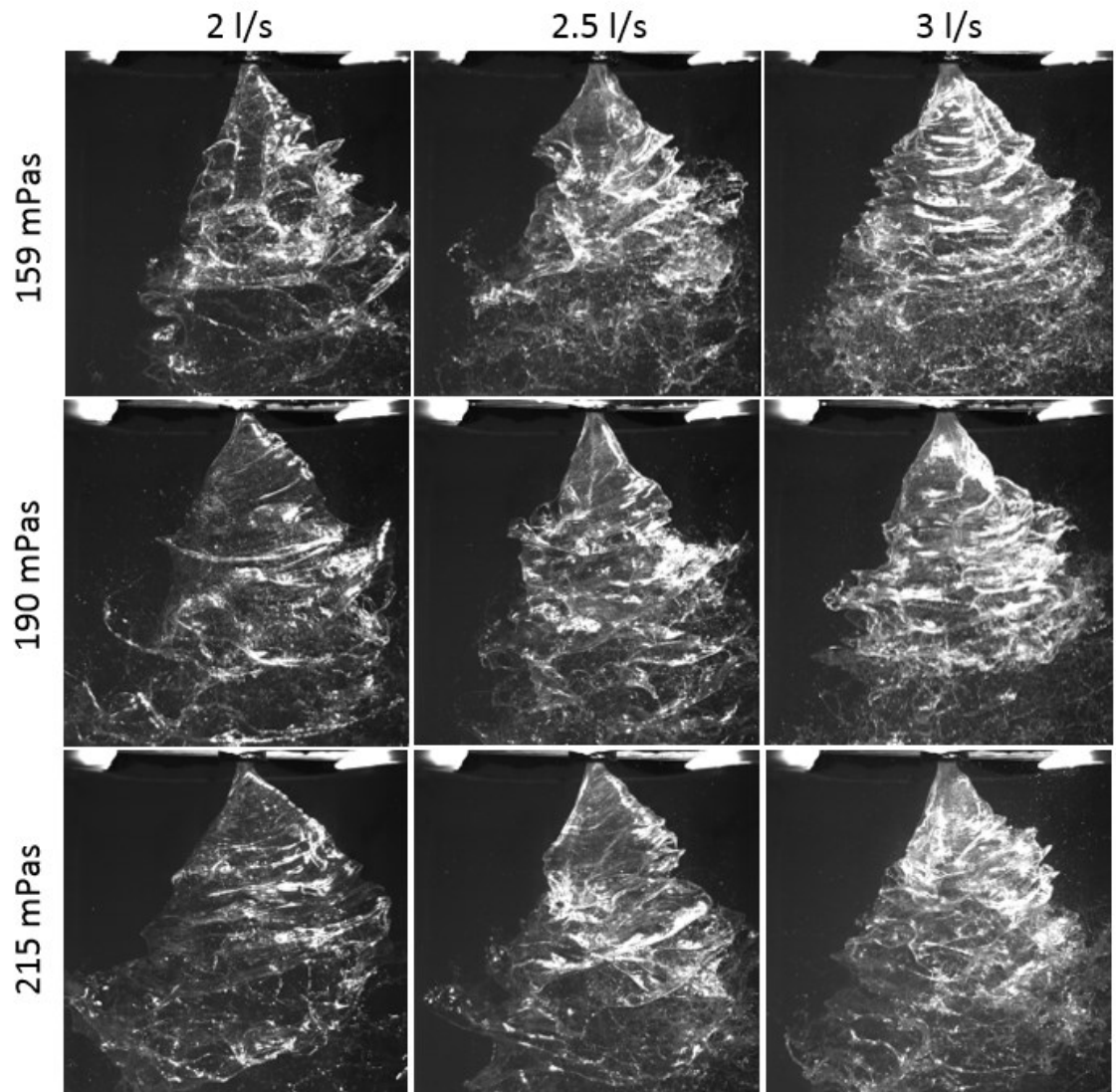


*Figure 40. Spray images at varying flow rate and viscosity (side view).*